True High-Efficiency Commercial Aircraft

The Final Report - Group 1

by

Jeffrey R. Chen
Benyamin De Leeuw
Adnan Feim
Jacob Fransen
Bas Grootnibbelink
Pjotr Lengkeek
Toto Marchand
Antonin Panzo
Kevin Siemonsma
Camille van Weert

as part of the Bachelor course

AE3200 Design Synthesis

in Aerospace Engineering

Student numbers:	4431561, 4471121, 4366336, 4489098, 4357132	
(ordered)	4433866, 4280601, 4436393, 4291719, 4430158	
Project duration:	April 23, 2018 – July 9, 2018	
Thesis committee:	Dr.ir. René Alderliesten,	TU Delft, tutor
	Victor Villalba,	TU Delft, coach
	Haohua Zong,	TU Delft, coach

Date: July 3, 2018
Version: 1.1

This page is intentionally left blank

Contents

Acknowledgements

We would like to express our greatest gratitude to the guidance and support provided throughout the project by tutior Dr.ir René Alderliesten, and coaches Victor Villalba and Haohua Zong. We thank the PMSE team for the information provided regarding the systems engineering and project management aspects of the DSE. We would also like to extend a thanks to professors at the faculty of Aerospace Engineering TU Delft, for providing their knowledge on various aircraft design aspects.

Nomenclature

Abbreviations

A/C	Aircraft
BWB	Blended Wing Body
CFD	Computational Fluid Dynamics
FBS	Functional Breakdown Structure
FF	Fuel Fraction
FFD	Functional Flow Diagram
FW	Fuel Weight
FY	Financial Year
HSNLF	High Speed Natural Laminar Flow Airfoil
MAAMF	Mylar Aluminiumfoil Aluminiumfoil Mylar Fiber
MAC	Mean Aerodynamic Chord
MTOW	Maximal Take-Off Weight
NIST	National Institute of Standards and Technology
OEW	Operational Empty Weight
PW	Payload Weight
RAMS	Reliability, Availability, Maintenance and Safety
TSFC	Thrust Specific Fuel Consumption

Symbols

α	Angle of attack	$[degrees]$
α_{0L}	Zero lift angle of attack	$[degrees]$
β	Thermal expansion coefficient	$[1/K]$
β_{fill}	Fill ratio	$[-]$
$\dot{m}$	Mass flow	$[kg/s]$
ϵ	Emissivity	$[-]$
η	Efficiency	$[-]$
$\frac{c}{V}$	Climb gradient	$[-]$

$\frac{T}{W}$	Thrust loading	$[-]$
$\frac{W}{S}$	Wing loading	$[N/m^2]$
γ	Heat capacity ratio	$[-]$
Λ	Sweep angle	$[degrees]$
λ	Taper ratio	$[-]$
μ	Dynamic viscosity	$[Pas]$
ν	Kinematic viscosity	$[m^2/s]$
ϕ	Angle between perpendicular of the skin and horizontal axis	$[rad]$
ϕ_E	Energy derivative	$[Pa\ m^3/J]$
ρ	Density	$[kg/m^3]$
σ	Stefan-Boltzman constant	$[J/sm^2K^4]$
σ_{hoop}	Hoop stress	$[Pa]$
σ_{long}	Longitudinal stress	$[Pa]$
θ	Ellipse angle	$[rad]$
A	Aspect ratio	$[-]$
$A_{ellipse}$	Ellipse cross sectional area	$[m^2]$
A_{skin}	Skin cross sectional area	$[m^2]$
A_{str}	Stringer cross sectional area	$[m^2]$
A_{tank}	Wetted area of the tank	$[-]$
b	Total wing span	$[m]$
b_w	Span of one wing	$[m]$
c	Climb rate	$[m/s]$
c_r	Root chord	$[m]$
c_t	Tip chord	$[m]$
C_D	Drag coefficient of wing	$[-]$
C_L	Lift coefficient of wing	$[-]$
C_l	Lift coefficient of airfoil	$[-]$
$C_{p,0}$	Minimum pressure coefficient	$[-]$
C_p	Pressure coefficient	$[-]$
cp	Specific heat	$[kJ/kgK]$
D	Diameter	$[m]$

e	Oswald span efficiency factor	$[-]$
E_L	Loiter endurance	$[s]$
E_N	Effort needed for N^{th} aircraft	$[-]$
E_{sp}	Specific energy	$[J/kg]$
f	Weight fraction	$[-]$
F_{long}	Longitudinal force	$[N]$
F_P	Reaction force in skin due to pressure	$[N]$
g	Gravitational acceleration	$[m/s^2]$
Gr	Grashof number	$[-]$
h	Enthalpy	$[kg/kJ]$
h_i	Cruise height	$[m]$
h_c	Convection coefficient	$[W/m^2K]$
h_{ei}	Energy height	$[m]$
h_r	Radiation coefficient	$[W/m^2K]$
$I_{yy,fus}$	Area moment of inertia of the fuselage in the y-direction	$[m^4]$
$I_{yy,str}$	Area moment of inertia of the stringers in the y-direction	$[m^4]$
K	Effort needed for the first aircraft	$[-]$
k	Thermal conductivity	$[W/mK]$
k_A	Airfoil technology factor	$[-]$
k_{fsp}	Fuel constant	$[lbs/gal]$
L	Conductive distance (thickness of the insulator)	$[m]$
l	Length	$[m]$
l_0	Cabin front section length	$[-]$
l_f	Fuselage length	$[m^2]$
M	Mach number	$[-]$
m	Mass	$[kg]$
M_∞	Free stream Mach number	$[-]$
M_{cr}	Mach critical number	$[-]$
M_{dd}	Mach drag divergence number	$[-]$
N	Number of aircraft produced	$[-]$
N_e	Number of engines	$[-]$

N_t	Number of tanks	$[-]$
n_{pax}	Number of passengers	$[-]$
Nu	Nusselt number	$[-]$
P	Pressure	$[Pa]$
Pr	Prandtl number	$[-]$
Q	Heat flow	$[W]$
R	Thermal resitance	$[K/W]$
r	Radius	$[m]$
$R_{ellipse}$	Ellipse radius	$[m]$
R_{max}	Maximal range	$[m]$
R_{mis}	Design range	$[m]$
Ra	Rayleigh number	$[-]$
S	Wing surface area	$[m^2]$
s	Learning rate	$[-]$
S_{blend}	Blend area	$[m^2]$
S_{floor}	Cabin floor area	$[m^2]$
S_f	Fuselage area	$[m^2]$
$s_{landing}$	Landing distance	$[m]$
s_{TO}	Take-off distance	$[m]$
SF	Scaling factor	$[-]$
T	Temperature	$[K]$
t	Thickness	$[m]$
t	Time	$[s]$
t/c	Thickness to chord ratio	$[-]$
T_∞	Temperature of the ambient	$[K]$
T_{cr}	Cruise thrust	$[N]$
t_{floor}	Floor thickness	$[m]$
$T_{frac_{cr}}$	Maximal cruise thrust setting	$[-]$
t_{skin}	Skin thickness	$[m]$
T_{sur}	Temperature of insulation surface	$[K]$
T_{TO}	Take-off thrust	$[N]$

u_1	Center cabin length ratio	$[-]$
u_2	End cabin length ratio	$[-]$
V	Speed	$[m/s]$
v_1	Center cabin width ratio	$[-]$
v_2	End cabin length ratio	$[-]$
V_{tank}	Tank volume	$[m^3]$
W	Weight	$[kg]$
W	Work	$[W]$
x	Quality of vapor	$[-]$

List of Figures

List of Tables

1 Introduction

Efficiency and sustainability are two aspects that are becoming more important in the commercial air travel industry. With regulators moving towards ever stricter noise and emissions regulations, and airlines looking for more efficient aircraft to reduce their cost, there is a need for a new aircraft that can fulfill both the future sustainability requirements whilst also improving the aircraft efficiency.

With the greenhouse effect being a large contributor to global warming, there has been a significant push to reduce the amount of greenhouses gases (CO_2, NO_x, etc.) in an effort to stop global warming. The warming will cause, and is already causing, substantial problems related to health, climate and migration. One of the contributors to the greenhouse effect is the aviation industry. As more people are expected to gain access to air travel, especially in developing countries, air travel is set to increase its contribution to the greenhouse effect. It is for this reason that the aircraft industry is seeking to innovate with respect to sustainability and efficiency.

This is where this design team comes in, presenting the world's first commercial hydrogen powered aircraft: HYDRA. The aim of the design team is to bring to market a new commercial passenger aircraft that increases efficiency, in terms of total lifecycle energy usage, by 20% whilst reducing the lifecycle cost of the aircraft by 10% compared to the current Airbus A320 and Boeing 737. HYDRA will have a range of 6200 km whilst accommodating 170 passengers.

The purpose of this report is to present the preliminary design of the main systems of the HYDRA. In addition to the design of the systems other aspects of the aircraft such as its cost, associated risk, sustainability, etc. are evaluated.

The report begins with an executive overview, Chapter 2 where key design choices and findings from each aspect of the design are presented.

Following this the top level concept is presented in Chapter 3. Following, the technical analysis of the various divisions is presented starting with Chapter 4, then the structural design of the aircraft is shown in Chapter 5. Furthermore, the power and propulsion system design is in Chapter 6 and the stability and control of HYDRA is laid out in Chapter 7.

After presenting the various design aspects, aircraft performance is shown in Chapter 8. This is followed by the results from the Reliability, Availability, Maintenance and Safety (RAMS) analysis in Chapter 9. Then the production plan and operations & logistics are presented in Chapter 10 and Chapter 11 respectively. The sustainability of the project was analyzed and is presented in Chapter 12. The target market for HYDRA as well as an estimate for the cost associated with producing and operating the aircraft are shown in Chapter 13. A functional analysis of some of the primary aircraft systems is shown in Chapter 15.

Finally, an overview of the final design and key performance parameters are presented in Chapter 16. This chapter also examines whether all requirements set prior to the design phase are met by the current design. The report concludes with a discussion on the future of the project in Chapter 17. This chapter discusses further improvements or steps that can be taken by each of the technical departments to improve upon the current design.

2
Executive Overview

2.1. Top Level Concept

It was settled that the top level design would revolve around a blended wing body aircraft with open rotor engines and powered by liquid hydrogen.

Class I weight estimation yielded an operational empty weight (OEW) of 47241kg and a maximum take off weight (MTOW) of 69493kg. The results from a class I weight estimation of such an unconventional aircraft comes with greater uncertainties than of conventional aircraft. The use of class II weight estimation based on initial sizing provided an OEW of 56993kg and a MTOW of 79571kg.

The wing-thrust loading diagram made was used to place several restrictions on the wing plan form. The design point was found to have a wing loading of 2400 $\frac{N}{m^2}$ and a thrust loading of 0.296 $\frac{T}{W}$.

An initial sizing of the aircraft geometry was completed based on several basic parameters including number of passengers, required floor area, and wing-thrust loading diagram. For the wing, the reference area is 284.05 m^2.

2.2. Aerodynamics

The aerodynamic characteristics of the BWB focused strongly on the fuselage and the wing. Through 2D analysis using Xfoil, the airfoil selected for the body and outer wing were respectively, HSNLF-2017 and HSNLF-0217. Using a model created in XFLR5 an estimate of the maximum lift over drag ratio of 21.5 was obtained. The model considered the body of the aircraft, the outer wing as well as the empennage, engines could not be modelled in XFLR5 and thus the drag due to the engine is not considered at this stage in the design.

Through the sizing of the high lift devices, a double slotted Fowler flap was selected, achieving the required maximum lift coefficient at landing condition of 1.3, at an angle of attack of 14°.

2.3. Structures

In the implementation of the structural design, the aspects of the design which were most unconventional and critical were focused on. This included stress analyses throughout the cabin skin, fuselage stringers, and the wing box.

From the cabin skin analysis, the varying skin thickness around the elliptical cross-section of the cabin and also along the length of the cabin were determined, where the maximum was found to be 1.5$[mm]$ in the center section of the cabin. The stringer area of the fuselage stringers was found to be 844$[mm^2]$ for each stringer. The wing box analysis revealed that for the desired wing from the Aerodynamics department, the box would need to have 5 stringers at the root, decreasing to 3 at the tip. The upper skin thickness varies from 9$[mm]$ at the root to 1$[mm]$ at the tip.

Another aspect which is often a challenge for BWB configurations is the weight estimations, thus this was also addressed in detail. The area of the fuselage and wing box stated above were used in part, together with estimations from Howe [29] and Torenbeek [65]. This yielded weights for the outer wing, inner wing, cabin, empennage, and landing gear, the sum of which is the airframe weight. The airframe was found to be 27802[kg].

2.4. Power and Propulsion

There were several changes in Power and Propulsion when comparing HYDRA with conventional aircraft. The first change was the use of hydrogen as fuel. The hydrogen fuel is stored at cryogenic temperatures to increase the volume as much as possible. Due to the large temperature difference between the hydrogen and the ambient temperature, insulation was designed to decrease the heat transfer into the tank. This was done in order to reduce the temperature increase and therefore reduce the pressure increases. The designed insulation consists of different layers, as described in[74]. The thickness of the tank was determined to be 0.14 m thick. The foam dominates the thickness of the insulation, since it was found to be the most effective out of all the layers.

The tank parameters where optimized with the the use of the thermodynamic model developed in subsection 6.2.1 are shown in Table 2.1.

Parameter	Value	Unit
V	75.3	m^3
$m_{hydrogen}$	4731	kg
m_{tank}	4737	kg
t_{foam1}	0.063	m
t_{foam2}	0.063	m
$t_{alu_{liner}}$	0.00335	m
$t_{glass\ fiber}$	0.003	m
t_{total}	0.1405	m

Table 2.1: Tank parameters

The behavior of the pressure in the tank can be seen in Figure 2.1

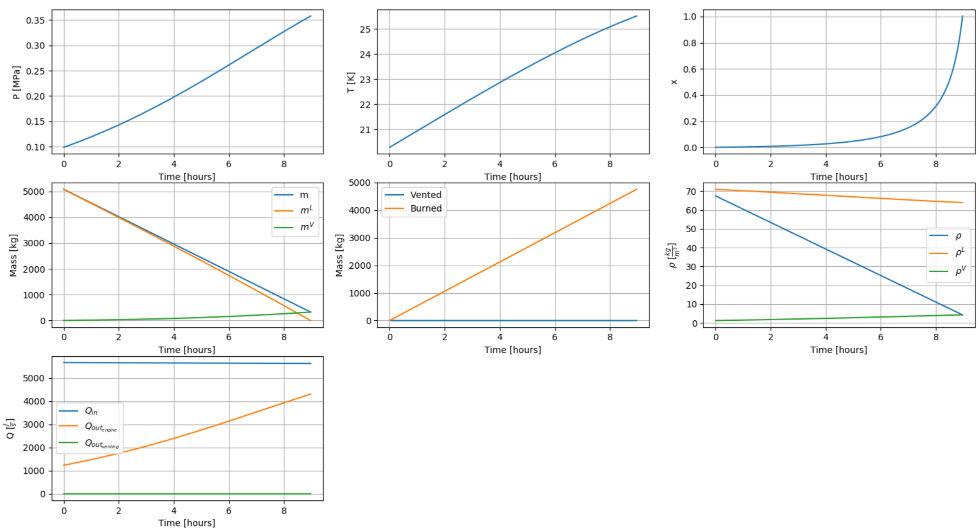

Figure 2.1: Behavior of tank in cruise

Open rotor engines were selected because of the increased efficiency of the open rotor engine. Because hydrogen was taken instead of kerosene, the combustion chamber needed adaptations. The adaptation was the fuel injection system which improved the mixing of the fuel with the air therefore reducing the NOx emissions. The sizing of the open rotor was done by scaling a reference engine resulting in the following data for the open rotor for HYDRA, shown in Table 2.2.

Table 2.2: Engine sizing

Parameter	Value
Thrust [N]	101,000
Outer diameter of the propeller [m]	3.84
Inner diameter of the propeller [m]	1.56
Length of the engine [m]	6.57
Weight of the engine [kg]	3422

The fuel system had to be adjusted to the use of the hydrogen. Because the fuel should be transported between the engines and APU at still cryogenic conditions. Another problem that came up was the temperature of the hydrogen before the combustion. The solution to this was the introduction of regenerative heating, in which the waste heat of the engine was used to heat up the fuel, which further improves the thermal efficiency. The weight of the fuel system was also estimated, and resulted in 373.5 kg.

The APU was found to be a necessary device in all aircraft, but only used on the ground. The APU was found to be a small gas generator. The APU in HYDRA has been designed such that it will run on hydrogen, by implementation of the same combustion chamber technology as for the engines. The weight was determined also for the APU and found out to be 160 kg.

2.5. Stability and Control

Stability and control are of paramount importance to aircraft design. After all, if an aircraft is not stable for all conditions normally encountered during flight, a control input or a perturbation (a gust of wind for example) will cause the aircraft to go into uncontrolled oscillation or require constant (auto)pilot input. However, if an aircraft is too stable, it will become uncontrollable, as the response to control inputs will be too slow.

Two types of stability can be discerned: static and dynamic stability. Static stability is the initial tendency of the aircraft to return to its original position when it is disturbed. Dynamic stability implies that any oscillations to the aircraft dampen out over time.

First, the aircraft balance and center-of-gravity distribution were determined by means of a loading diagram. This loading diagram plots the aircraft weight versus the center-of-gravity location as the loading process takes place, and it thus yields the range of cg locations that the aircraft would ever encounter during operation.

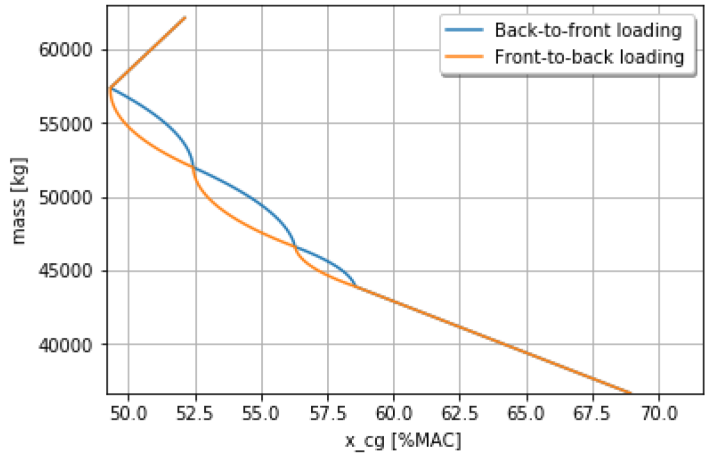

Figure 2.2: Loading diagram

Table 2.3: Center of gravity range

Minimum cg position [%MAC]	49.15
Maximum cg position [%MAC]	71.63

With the cg location in hand, the landing gear location can be determined. A number of criteria are important here:

- Nose wheel steering capacity should be adequate.
- The aircraft should not tip back during loading due to very aft cg locations.
- The aircraft should not tip back and cause a tail strike during take-off.
- The aircraft should not tip over sideways during tight turns while on the ground.
- Sufficient tip clearance should be ensured during high-bank angles when landing.

Keeping these criteria on the landing gear positioning in mind, and by means of simple statics-equations, the basic landing gear design was performed:

Table 2.4: Loading diagram input parameters

Parameter	**Value**	**Unit**
$x_{nosegear}$	3.8	m
$x_{maingear}$	22.6	m
$y_{maingear}$	2.56	m
Number of main gear struts	2	-
Number of wheels per main gear bogey	2	-
Number of nose gear struts	1	-
Number of wheels per main nose gear bogey	2	-

2.5.1. Static stability

Static stability is ensured by means of a horizontal stabilizer. Using the longitudinal moment equations for an aircraft in steady, horizontal (stick-fixed) flight, one can determine the optimal horizontal tail surface area to satisfy both the stability and control requirement(s). By means of a so-called scissor plot, the horizontal tail surface area was determined to be 71.32 square meters, or 24.07 percent of the total wing surface area.

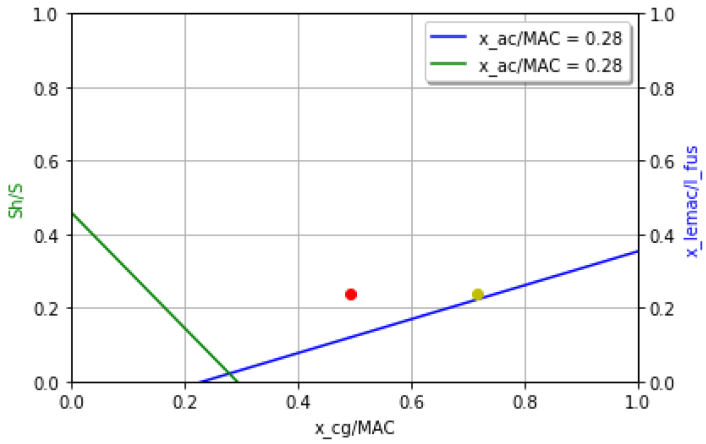

Figure 2.3: Stability and Control plot

With an area for the horizontal tail in hand, it could be sized and an airfoil could be selected. My means of a reference procedure, the tail was sized as follows:

Table 2.5: Inputs needed for the sizing of the horizontal tail.

	Horizontal tail	Vertical tail
A [-]	4	1.1
λ [-]	0.4	0.65
Λ [°]	30 (at LE)	43 (at 0.25c)

The NACA 0014 and NACA 0009 airfoils were selected for the horizontal and vertical stabilizer respectively, both for their low inherent drag.

2.5.2. Dynamic stability

For dynamic stability, a state-space model was constructed in MATLAB. This model utilizes the standard equations of motion for aircraft, and can be used to assess the dynamic response to control inputs and/or disturbances. The model outputs the eigenvalue plot and the dynamic step response curves. With the selected control and stability derivatives, the aircraft was determined to be dynamically stable under all conditions. For the plots as described in this section, the reader is kindly referred to section 7.3.

2.6. Aircraft Performance

Several requirements of the aircraft concern the performance of the aircraft during flight. Accordingly, the performance was assessed for the different phases of the flight based on the parameters from the top level concept.

The airfield performance analysis yielded the take-off and landing distance, 1329 m and 1697 m respectively. Moreover, the climb and descent phase were considered assuming a constant indicated speed for both. The cruise was also included where a gradual climb was assumed in order to keep the cruising speed constant. Combining all the phases the total distance reached, the flight time and the fuel burnt over flight were obtained. The distance was 2857 km, the flight time 3hrs 38 min and the fuel burnt 1920 kg. The overall flight distance covered for the design parameters can be seen in Figure 2.4.

Additionally, the flight envelope and the turning performance were considered in the performance analysis. The flight envelope determined a maximum load factor of 2.5. The turning performance analysis resulted in a minimum turn radius of 810 m and a minimum turning time for a full circle of 54 s.

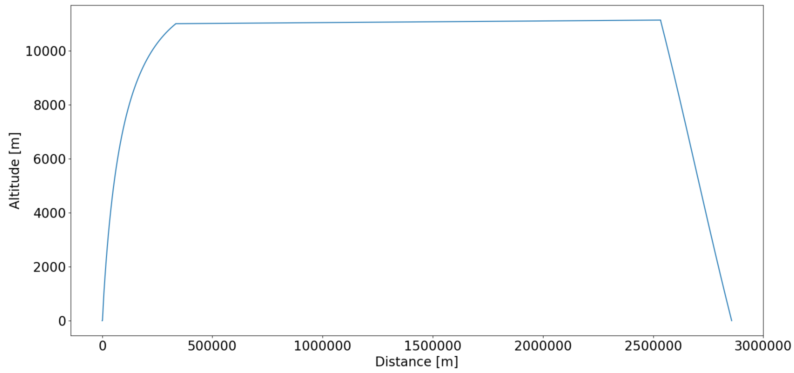

Figure 2.4: Distance of the whole flight as a function of altitude.

2.7. RAMS Characteristics

Turnround time is an important aspect of reliability and availability. With the use of conventional cargo boxes, loading times are similar to that of an A320. The time needed for refueling will also remain despite the increased volume of fuel needed due to the use bigger pumps with greater mass flow. While it is difficult to determine the reliability of each subsystem at this stage, it is probable that the probability of failure is similar to that of a conventional aircraft.

Maintainability characteristics of HYDRA will differ from conventional aircraft in the B and C type checks. Increased maintenance on the fuel system and functional system need to be performed during such checks.

There are two characteristics with regards to safety, namely location of engines and hydrogen fuel tanks. The placement of engines at the rear ensures that blade failure will not lead to a structural failure in the cabin, while rear located fuel tanks ensure that in the event of a fire, it will not spread throughout the cabin. Four type I doors and four type II doors are present to allow for speedy emergency evacuation that satisfies CS25 requirements.

2.8. Production Plan

There are three main stages to production; part manufacturing, subsystem assembly, and final assembly. It is of great importance that timing is well managed as the delay of one part will have a domino effect, delaying subsequent aircraft deliveries.

The learning curve in manufacturing should be recognized as a mean as reducing cost and increasing production numbers, with an expectation that production will begin with 16 aircraft a month initially and rise to 23 aircraft a month by the 2800th aircraft. This results in a total production of 4000 aircraft in a time of 15 years and 4 months.

2.9. Operations and Logistics

Operations concerns the tasks needed to operate the aircraft, whilst logistics covers the process of getting everything to the aircraft to make it operable.

With regard to operations, unique aspects of HYDRA include the 3-6-3 abreast seating configuration, the use of hydrogen, and a wide cargo compartment. The 3-6-3 abreast seating is not expected to increase loading times significantly. The use of hydrogen presents an infrastructural problem that requires the modification of existing pipelines. The wider cargo compartment should not be expected to increase loading times or increase costs as standard cargo containers will be utilized.

For logistics, the greatest problem faced for HYDRA is the lack of hydrogen infrastructure. It has been shown that this problem may be alleviated to a certain extent with efforts in various European nations including

France and Germany already building a hydrogen pipeline network. In other countries, modifications of traditional oil pipelines is needed or the implementation of electrolysis factories at airport locations. For the target market in southeast Asia, India has researched hydrogen infrastructure for transportation purposes and aim to have test facilities for refueling available by 2050. Japan, China, and South Korea are also investing in hydrogen as a means of fossil fuel replacement.

2.10. Sustainability Development Strategy

Given the aim of designing a truly high-efficient aircraft, sustainability is a key factor.

Through the use of hydrogen, the primary by-product is H_2O and NO_x. While, H_2O is a greenhouse gas, it's residence time in the air is only about 6-12 days, which is significantly shorter than the 100 years for CO_2. The concern with regards to NO_x may to a certain extent be solved through leaner combustion, however this is something that needs to be investigated further. There are also concerns regarding the production of hydrogen, of which about 97% is from natural and 3# from electrolysis. However, it is expected that with eyes on the long term, hydrogen production will shift more towards electrolysis.

There is a significant concern over the noise produced through the use of open rotor engines. While at this stage no detailed design with regards to engine noise has been completed, industry research with the use of CFD analysis has shown that modern day technology is able to design rotor blades such that noise regulations both current and for the future will be met.

As sustainability carries through the entire life-cycle of an aircraft, the end-of-life disposal options should be examined. With HYDRA's structure built primarily using aluminum, the material is easily recyclable. Engine's and other components are also designed for long-term use in mind and may be able to placed on other aircraft after end-of-life of aircraft.

2.11. Market Analysis

A market analysis was performed to help determine the opportunities and risks that lay in the market. The two primary competitors for HYDRA are the Boeing 737 and the Airbus 320. Reports by Boeing and Airbus predict an estimated volume of single aisle aircraft from 2016-2036 of 24810 to 29530 aircraft. A increasing proportion of these aircraft will operate in emerging markets, namely southeast Asia. Given the opportunities present in the market, an entry into service date of 2030 has been set.

Given the importance of cost over the viability and sustainability of an aircraft program, it was set early on that the aircraft would be required to have a total lifecycle efficiency that is 10% lower than the B737 and A320. The final lifecycle cost of the aircraft assuming an optimistic scenario is $872 million, which represents a $350 million decrease in price in comparison to the A320. From the perspective of the manufacturer, the break-even point lies at 265 aircraft, assuming that there is a learning curve. The final cost breakdown based on subsystems is given below.

Table 2.6: Allocated cost budget in million of dollars with contingency factor

Subgroup	Wing	Fuselage	Tail	Landing gear	Propulsion	Systems and equipment	final assembly	payload and cabin layout
Specification cost [$$10^6$]	11,4	11,7	4,2	1,3	3,8	2,5	2,5	4,62
Target cost [$$10^6$]	0,5	10,8	3,9	1,2	3,5	2,3	2,3	4,3
Contingency factor	0.08	0.08	0.08	0.08	0.08	0.08	0.08	0.08

2.12. Risk Management

Several technical risks were established and mitigation techniques were implemented. Each risk was quantified in probability of occurrence and consequence. For visualisation purposes, a risk map is produced, both prior and after mitigation.

There were 5 main technical risks identified. The first is blade penetration into the empennage due to the lack of an engine nacelle. This risk is mitigated through designing control surfaces with redundancy with both hydraulic and electrical lines. The second is the risk of propeller detachment as a result of bird strikes, which is mitigated through increases in maintenance. The third is the fire hazard from the fuel tanks, which is mitigated through a coating of fire retardant substance outside the fuel tank, and the cooling of the tank to lower risk of self combustion. The fourth is the freezing of hydrogen due to leakage. The associated consequences are not that high and are mitigated through the use of additional pressure and temperature measuring devices to ensure early detection. The fifth is that the repair of hydrogen tanks will require disassembly. Mitigation involves a repair technique that a hole on the fuselage skin can be cut out as a temporary access point to the damaged part of the tank. The hole can then be patched.

2.13. Functional Analysis

A functional flow diagram was developed which showed the logical order of functions which the aircraft must perform. This helps for when the aircraft is in operations, visualizing the sequential functions which should be undertaken on the ground and also in flight.

A functional breakdown structure was developed, slightly different from the flow diagram in that it is not sequential, but rather shows the breakdown of each of the functions which must be performed. A distinction was firstly made between operations and maintenance, and the different functions broken down from there. The operations branch was elaborated on in more detail since this is the primary function of the aircraft.

2.14. Efficiency

Ultimately, the goal was to design a true high-**efficiency** commercial aircraft. As such, efficiency is one of, if not the, most important parameters that has always been kept in mind throughout the entire design process. Use of the, now famous, efficiency equation has yielded the following results for efficiency, and it is clear that the HYDRA is, in most respects, substantially more efficient than state-of-the-art competitors.

Table 2.7: Efficiency comparison: A320 NEO vs. HYDRA

Aircraft	Range [km]	EIS	η_0 [-]	$\frac{CL}{CD}$ [-]	OEW [kg]	FW [kg]	m_{pax} [kg]	E_{sp} [J/kg]	Efficiency [J/m]
A320 NEO	5 639	2016	0.37	19.07	47000	17750	14250	4.28e7	1846
HYDRA	6 200	2030	0.40	21.50	56993	2364	16150	1.20e8	1372

2.15. Future Planning

Given the limited time and resources in the DSE, several aspects of design have not yet been explored but remain of interest. For aerodynamics, a greater detail over flow characteristics of the entire aircraft shall be performed using CFD. For structures, greater analysis of connections of subsystems such as the empennage and windows would be performed. Materials would also be examined more in depth as would the type of stringers, and the load bearing paths of different fastening methods. For stability and control, a more detailed control system would be designed and more detailed stability derivatives would be determined from aerodynamic analysis using CFD.

3

Top Level Concept

Proceeding from the Midterm report [2], it was decided to develop the concept of a hydrogen powered blended wing body aircraft with open rotor engines. In order to design a complex system, which an aircraft undoubtedly is, the system is broken down into subsystems and analyzed separately. However, simultaneously compatibility between the subsystems must be ensured. Such that when the subsystems are put together, the final system fulfills the required function whilst meeting required performance parameters.

In this chapter, the top level concept (TLC) of the aircraft is discussed. First, in section 3.1, the class I weight estimation is presented. Then, in section 3.2, the wing/thrust loading diagram is presented. In section 3.3, the internal composition, including the cabin and cargo compartment, and the external geometry, which includes the fuselage and outer wing, sizing is described. Following, the determination of the component is explained in section 3.4. Finally, the class II weight estimation is shown in section 3.6.

The N2 shown in Figure 3.1 illustrates overview of the iterative process. It is to be noted that for this design, given the time constrain and complexity of an unconventional design, only local iterations were made, and the main loop of iteration from class II weight estimation back to class I, as shown with the green boxes, was not made.

Class I weight estimation	MTOW		MTOW	MTOW	MTOW	FW_max	MTOW,OEW, FW	
	Wing-thrust loading diagram		W/S		T/W			
		Interior geometry	Geometry			Geometry	Geometry	CG location
		Geometry	**Wing-fuselage geometry**	Geometry		Geometry	Geometry	CG location
L/D	C_L_max,A		Wing sweep	**Aerodynamic analysis**				MAC and AC location
					Engine sizing		Geometry	CG location
			Geometry			**Fuel tank sizing**	Geometry	CG location
OEW							**Class II weight estimation**	Component weights
			Wing position	Geometry			Geometry	**Tail sizing**

Figure 3.1: TLC process N2 chart

3.1. Class I weight estimation

The class I weight estimation serves to obtain a first estimate of the weight of the aircraft, based on which the first iteration of the design is made. It is important to obtain an estimate that is as accurate as possible right at the beginning, because the closer the initial estimate is to the final value, the less iteration effort

Table 3.1: Blended wing body statistical data [13]

Design	VELA 3	NACRE	OREIO	N2A-EXTE	ACFA	BWB150	BWB250	BWB400
PW [t]	137	127	45.36	46.72	50	20.5	43.8	64
OEW [t]	327	307	112.85	101.82	225	38	79.9	130.9

is required during the design process. Typically, class 1 weight estimation is a statistical method based on previous designs. For conventional aircraft, an extensive database of existing designs is readily available. However, for blended wing body aircraft, there is currently no existing design in service, and all of the works on blended wing bodies are only scientific studies. Due to that, the uncertainty of such an estimation is much greater than for a conventional tube-and-wing aircraft, however at this stage it is the only available option to start the design with.

A linear relation in the form of

$$OEW = OEW_a PW + OEW_b \tag{3.1}$$

with PW being the payload weight, OEW operational empty weight and OEW_a and OEW_b the linear fit parameters is obtained. The parameters OEW_a and OEW_b are obtained as a linear least square fit through the data from Table 3.1.

To determine the maximal take-off weight (MTOW), the fuel weight needs to be calculated. Using the method of Torenbeek [66], the procedure to obtain the MTOW is performed. First, the fuel fraction required for the cruise at design range is calculated by

$$FF_{cr} = \frac{R_{mis} + R_{lost}}{\frac{\eta_0 \frac{C_L}{C_D} E_{sp}}{g} + 0.5(R_{mis} + R_{lost})} \tag{3.2}$$

where R_{mis} is the design range, η_0 is the total propulsive efficiency, $\frac{C_L}{C_D}$ the cruise lift-to-drag ratio, E_{sp} the energy density of the fuel, g the gravitational constant and R_{lost} the lost range. The lost range is a concept to incorporate the additional fuel burn required to take-off and climb to the cruise altitude and is calculated with

$$R_{lost} = (1.1 + 0.5\eta_M)\frac{C_L}{C_D} h_{ei} \tag{3.3}$$

where η_M is the correction for engine efficiency operated in non-optimal Mach number and h_{ei} is the initial cruise energy height calculated as

$$h_{ei} = h_i + \frac{V_{cr}^2}{2g} \tag{3.4}$$

where h_i is the initial cruise height and V_{cr} the cruise speed.

$\frac{C_L}{C_D}$ is taken equal to 20.0 as the literature review performed in the Midterm report [2] on the subject showed a potential of achieving values as high as 22.0. However, at the begin of this design phase, it was realized that this value was only attainable for larger aircraft, because for smaller ones, the fuselage airfoil thickness is adversely affected by the minimal height requirement of a standing person [13]. Therefore, the $\frac{C_L}{C_D}$, which is one of the design goals, was lowered right at the beginning not to be over-optimistic, which may lead to a larger amount of iterations needed as the results would not initially converge with the expected value.

Furthermore, CS-25 regulations [21] stipulate that for safety reasons, after flying the required range, the aircraft has to be able to loiter for 30 minutes. Therefore, the fuel fraction based on optimal endurance is calculated as

$$FF_{loiter} = \frac{1}{e^{\left(\frac{E_L g TSFC}{\frac{C_L}{C_D} + d\frac{C_L}{C_D}_{loiter}}\right)}} \tag{3.5}$$

with E_L the required loiter time, $TSFC$ the thrust specific fuel consumption and $d\frac{C_L}{C_D}_{loiter}$ the statistical increase of $\frac{C_L}{C_D}$ at the maximal endurance condition [72].

Consequently, with an additional 5% of required reserve fuel, the design MTOW can be calculated as

$$MTOW = \frac{PW + OEW}{-1.05(FF_{cr} - FF_{loiter}) - 0.05} \tag{3.6}$$

The inputs and results are shown in Table 3.2.

Table 3.2: Class I weight estimation data

(a) Inputs

Parameter	Value	Unit	Parameter	Value	Unit
OEW_a	2.3617	-	g	9.81	m/s^2
OEW_b	7553.35	kg	η_M	0.3	-
R_{mis}	2800	km	h_i	11000	m
PW	20000	kg	E_L	1800	m
η_0	0.4	-	$TSFC$	4.32	mg/s/N
$\frac{C_L}{C_D}$	20.0	-	$d\frac{C_L}{C_D}_{loiter}$	2.0	-
E_{sp}	119.93	MJ/kg	V_{cr}	230	m/s

(b) Outputs

Parameter	Value	Unit
OEW	47241	kg
R_{lost}	410	km
FF_{cr}	0.0324	-
FF_{loiter}	0.9965	-
$MTOW$	69493	kg

3.2. Wing-thrust loading diagram

In order to size the wings and engines, a wing-thrust loading diagram can be made [72]. The diagrams are constructed based on top-level performance limitations and outline the design space of possible wing and thrust loadings. From there, the design loading was determined at the chosen design point. The following performance indicators were considered: stall in clean and landing configuration, take-off and landing distance, cruise thrust, climb rate, climb gradient and the maximal wingspan.

The aircraft has to have favorable stall characteristics bound by maximal stall speed, hence in combination with a lift coefficient, the maximal wing loading at clean and full-flap (landing) configuration are determined by

$$\left(\frac{W}{S}\right)_{stall_{clean}} = 0.5\rho_0 V_{s_{clean}}^2 C_{L_{max_{clean}}} \tag{3.7}$$

and

$$\left(\frac{W}{S}\right)_{stall_{landing}} = \frac{0.5\rho_0 V_{s_{landing}}^2 C_{L_{max_{landing}}}}{f} \tag{3.8}$$

respectively, where ρ_0 is the sea level air density, V_s is the stall speed, $C_{L_{max}}$ the maximal lift coefficient and f the maximal landing-to-take off weight fraction. The stall speeds are not prescribed by regulations, however for commercial reasons - certain airport prescribe a maximal approach speed for example, appropriate values need to be considered. For this design, reference values of the Airbus A320 [75] were used.

Next, the minimal take-off thrust limit followed from the take-off distance which was determined from statistical data based on the required take-off distance for existing aircraft [47]. This is considered to be valid even for a blended wing body aircraft, as the take-off performance is not expected to significantly vary from conventional aircraft.The relation is

$$\left(\frac{T}{W}\right)_{TO} = \frac{\left(\frac{W}{S}\right)}{(4.7s_{TO} - 2872.8)C_{L_{TO}}\sigma_\rho} \tag{3.9}$$

where σ_ρ is the density ratio, which is taken to be 1 at take-off as a sea level altitude is assumed, s_{TO} the take-off distance, and $C_{L_{TO}}$ is taken to be

$$C_{L_{TO}} = \frac{C_{L_{max_{TO}}}}{1.1^2} \tag{3.10}$$

meaning that the aircraft should take-off at a C_L value smaller than the maximal achievable to account for a safety margin [72].

Similarly, the landing distance is taken into account using a statistical relation

$$\left(\frac{W}{S}\right)_{landing} = \frac{C_{L_{max_{landing}}} \rho_0 s_{landing}}{2f0.5847} \tag{3.11}$$

where $s_{landing}$ is the required landing distance [72].

The required cruise thrust is calculated with

$$\left(\frac{T}{W}\right)_{cr} = \frac{f_{cr}}{T_{frac_{cr}}}\left(\frac{\rho_{cr}}{\rho_0}\right)^{0.75}\left(\frac{C_{D_0}\rho_{cr}V_{cr}^2}{2f_{cr}\frac{W}{S}} + \frac{2f_{cr}\frac{W}{S}}{\pi Ae\rho_{cr}V_{cr}^2}\right) \tag{3.12}$$

with T_{frac} being the cruise throttle setting, f_{cr} the average weight fraction during cruise, ρ_{cr} the cruise-level air density, A the wing aspect ratio, e the Oswald span efficiency factor, V_{cr} the cruise speed and C_{D_0} the zero-lift drag coefficient determined by [60]

$$C_{D_0} = \frac{\pi Ae}{4\left(\frac{C_L}{C_D}\right)^2}. \tag{3.13}$$

Climb rate performance is determined by the required climb rate

$$\left(\frac{T}{W}\right)_{climbrate} = \frac{c}{\left(\frac{W}{S}\right)^{0.5}\left(\frac{2}{\rho_0 C_{L_{climbrate}}}\right)} + \left(\frac{C_D}{C_L}\right)_{climbrate} \tag{3.14}$$

where c is the climb rate, $C_{L_{climbrate}}$ and $C_{D_{climbrate}}$ the optimal coefficients for climb rate are determined using [72]

$$C_{L_{climbrate}} = (3C_{D_0}\pi Ae)^{0.5} \tag{3.15}$$

and

$$C_{D_{climbrate}} = 4C_{D_0}. \tag{3.16}$$

Additionally, the climb gradient is evaluated at a desired value at full operational condition and prescribed value at one-engine-inoperative (OEI) condition with

$$\left(\frac{T}{W}\right)_{climbgradient} = \frac{c}{V} + 2\left(\frac{C_{D_0}}{\pi Ae}\right)^{0.5} \tag{3.17}$$

and

$$\left(\frac{T}{W}\right)_{climbgradient_{OEI}} = \frac{N_e}{N_e-1}\left(\left(\frac{c}{V}\right)_{OEI} + 2\left(\frac{C_{D_0}}{\pi Ae}\right)^{0.5}\right) \tag{3.18}$$

respectively, where $\frac{c}{V}$ is the climb gradient and N_e the number of engines.

Finally, there is a lower wing loading limit determined by the maximal wing span of the aircraft

$$\left(\frac{W}{S}\right)_{min} = \frac{g\,MTOWA}{b_{max}^2} \tag{3.19}$$

where b_{max} is the maximal wing span. The wing span of the aircraft determines its airport category. Each airport is certified for aircraft up to a certain category, so exceeding certain span limits may result in not being able to fly to certain airports. The Airbus A320 is a Type C aircraft, therefore $b_{max} = 36m$ is used [1].

The summary of the used parameters is given in Table 3.3.

When all the limit lines are plotted, Figure 3.2 is the result. The lines that turned out to be bounding of design space are plotted in red, the climb criteria in black and the stall and cruise limits in blue. The design space is highlighted in green. This leads to two conclusions, which are typical for blended wing bodied aircraft [13]: 1) low wing loading 2) small design space due to the maximal span limitation. The design point is chosen at the highest wing loading with the lowest corresponding thrust loading.

The loading at the design point is $\frac{W}{S} = 2400\frac{N}{m^2}$ and $\frac{T}{W} = 0.296$.

[1] URL `https://www.skybrary.aero/index.php/ICAO_Aerodrome_Reference_Code` [cited 27/06/2018].

Table 3.3: Wing and thrust loading sizing parameters

Parameter	Value	Unit
A	4.5	-
e	0.85	-
$V_{s_{clean}}$	170	m/s
$V_{s_{landing}}$	120	m/s
$C_{L_{max_{clean}}}$	0.6	-
$C_{L_{max_{landing}}}$	1.3	-
$C_{L_{max_{TO}}}$	1.1	-
f	0.98	-
N_e	2	-

Parameter	Value	Unit
f_{cr}	0.99	-
ρ_0	1.225	kg/m^3
ρ_{cr}	0.3636	kg/m^3
$T_{frac_{cr}}$	0.8	-
s_{TO}	2500	m
$s_{landing}$	1750	m
c	15	m/s
$\frac{c}{V}$	0.2	-
$\left(\frac{c}{V}\right)_{OEI}$	0.024	-

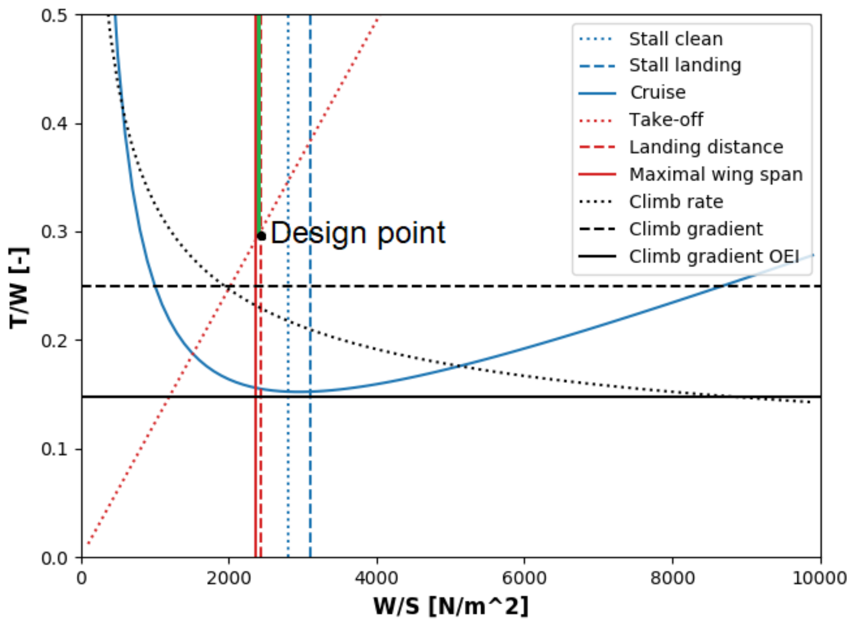

Figure 3.2: Wing-thrust loading diagram

3.3. Aircraft geometry

The determination of the aircraft geometry is split up into the determination of the center body subsection 3.3.1, the sizing of the outer wing subsection 3.3.2 and the landing gear subsection 3.3.3.

3.3.1. Center body

Transport of payload is the elementary function of an aircraft, hence the passenger cabin, cockpit and cargo compartment need to be designed. The required cabin floor area was calculated using a method from Torenbeek [65] as

$$S_{floor} = 0.6 n_{pax} \tag{3.20}$$

where n_{pax} is the number of passengers. Consequently, the cabin layout is determined. The shape of the cabin is assumed to be as the cabin seen in Figure 3.3a. It is favorable to have a narrower, but longer fuselage, as since the internal structure is fit within an airfoil shape for the outer skin, this leads to a lower fuselage area, thus leaving more area for the wings, which are more efficient at generating lift. The parameters v_1, v_2, u_1, u_2

and w_{cp}, determine the ratios of the shown lengths, and the geometry is fixed with solving

$$S_{floor} = [0.5v_1 + u_1 v_1 + 0.5u_2(v_1 + v_2)]\,{l_0}^2 + 0.5 w_{cp} l_0 \tag{3.21}$$

for l_0 with S_{floor} from Equation 3.20.

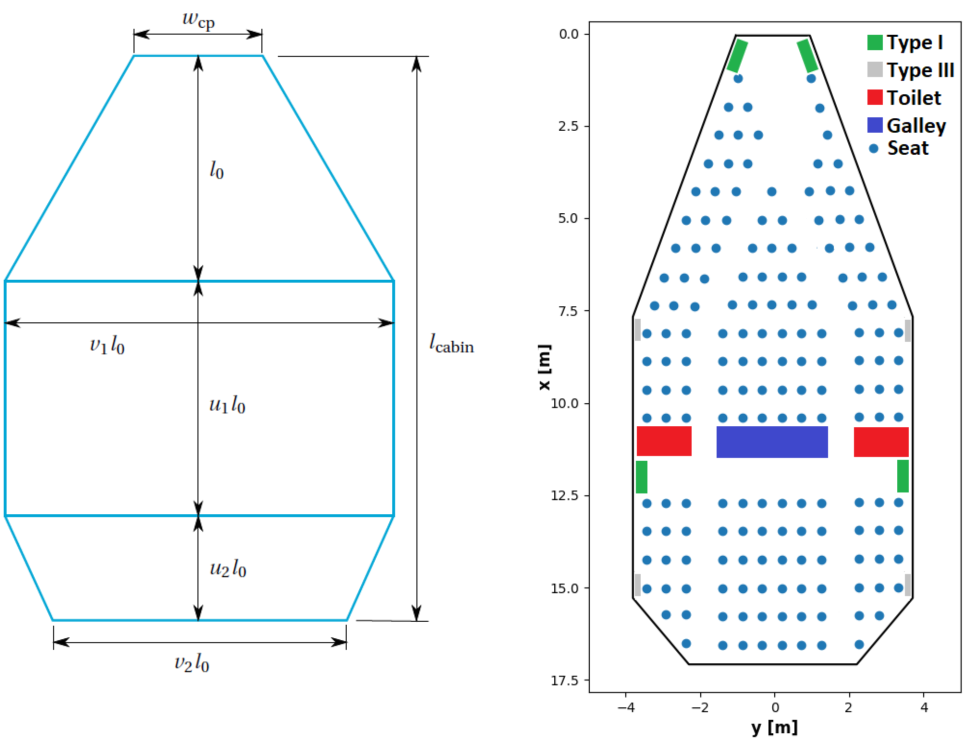

(a) Cabin general layout

(b) Seating configuration

Figure 3.3: Cabin layout

When the cabin layout is set, the passenger seating configuration is established. A 1-class low-cost configuration is considered to comply with requirement #TL2, see Table 16.3. Additional items to consider are the emergency exits, toilets and galleys. CS-25 regulations stipulate, that for aircraft seating 140 to 179 passengers are required to have 2 Type I and 2 Type III emergency exits on each side of the aircraft [21]. Type I emergency exits require an unobstructed passengerway of at least 91cm, Type III exits can be located next a passenger seat. The amount of toilets and galleys is not prescribed and therefore is a design choice. Additionally, each seat shall not be separated from the nearest aisle by more than 2 other seats. The resulting seating composition together with the exit location is shown in Figure 3.3b. The cabin contains 173 passenger seats and in the middle section, the seating is composed as 3-6-3. The summary of seating parameters is in Table 3.4.

A cockpit of 2.4x2m for 2 pilots is added in front of the cabin [70]. In order to make more efficient use of the available space, the cockpit section is lowered by 0.4 m with respect to the cabin. This allows an adequate cockpit length without enlarging the full fuselage, as well as a smaller window size to meet the required field of view. In order to roughly estimate the size of the window, the pilots eye is positioned 0.5 m from the centerline, 1.0m front the cockpit floor and 1.0m from the front of the cockpit. The side view is suggested in [70] to be +10° to -35° and the front view +20° to -20°. This will allow sufficient pilot view even in the landing configuration with an angle of attack 14, see subsection 4.3.4. The rendering of the described field of view is shown in Figure 3.5 for the left half of the aircraft. The resulting window size is measured in CATIA to be $S_{window} = 10.72m^s$ for the two windows at both side combined, measured at the intersection of the field of view and the fuselage skin.

Below the cabin, the cargo compartment is placed. Its dimension are determined such that requirement #40 of fitting 7 LD3-45W, shown in Figure 3.6, containers is met. The outline is shown in Figure A.3. It is located as front as possible for aircraft stability reasons. In result, the front wall of the cargo compartment is 3.37m back front the front of the cabin.

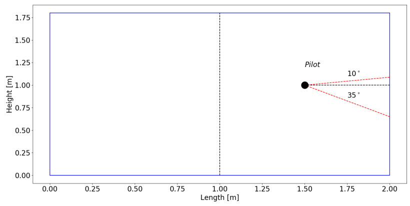

(a) Front view

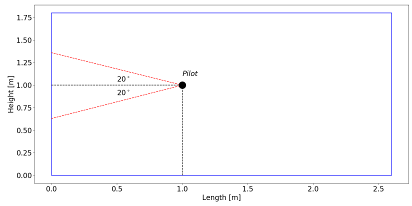

(b) Side view

Figure 3.4: Pilot sketches

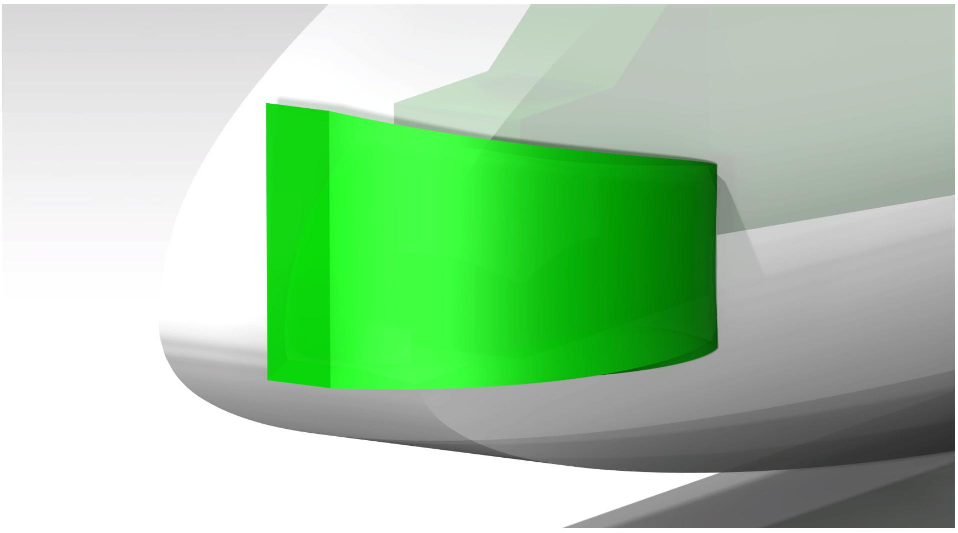

Figure 3.5: Render of the pilot view

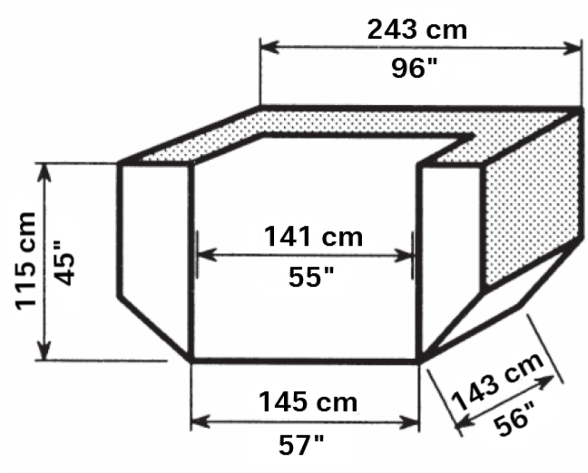

Figure 3.6: LD3-45W container dimensions [2]

After the cabin, cockpit and cargo compartment are determined, an oval pressure cell is formed around it. Due to the 3D shape of the assembly and limited time available, the assembly is modelled in CATIA, and the pressure cell geometry is tuned manually using the coordinate system of Figure 3.3b with the cabin floor located at z=0. An oval is constructed at y-locations, first at the cockpit, second and third at the front and back of the cabin's straight section and last at the end of the cabin. The center of each oval is fixed to the

[2]URL `http://goldenwave.vn/ban-tin-chung/kien-thuc-chuyen-nganh/79-container-hang-khong.html` [cited 02/07/2018].

Table 3.4: Seating parameters

Parameter	Value	Unit
n_{pax}	170	-
u_1	1.0	-
u_2	0.636	-
v_1	1.0	-
v_2	0.2	-
w_{cp}	2.0	m
p_{seat}	30	in
w_{seat}	21	in
w_{exit}	0.91	m

Parameter	Value	Unit
S_{floor}	114.0	m^2
l_0	7.56	m
$n_{pax_{max}}$	173	-
w_{aisle}	22.9	in
Type I exits	4	-
Type III exits	4	-
Toilets	2	-

yz-plane and the z-offset and the semi-minor and semi-major axes length are defined. The pressure cell is then defined by connecting the 4 ovals. The front is defined by a circular nose. The end is connected to the fuel tank, which is explained in subsection 3.4.2.

The next step is to fit the pressurized section into an airfoil shape, which is one of the key features of a blended wing body [13]. Similarly as with the cabin, CATIA is used to determine the geometry. The center airfoil is imported and defined at $y = 0.5w_{cp}$ to and $y = 0.5v_1 l_0$. The two airfoils with cord lenghts l_{f_0} and l_{f_1} respectively, are linearly connected, the shape is then mirrored around the yz-plane and the inner airfoil is connected between both sides. Finally, the y- and z-offset together with the scaling is defined such that the center body fully contains the pressurized cell.

3.3.2. Outer wing

The wing reference area is calculated using the wing loading obtained from the wing-thrust loading diagram as

$$S_{ref} = \frac{g\ MTOW}{\frac{W}{S}}. \tag{3.22}$$

For conventional aircraft, this reference area is interpreted as the area of the wing extended to the centerline of the aircraft. This is an approximation to account for the small, but non-negligible lift generated by the circular fuselage. [47]. However, for BWB the fuselage provides a significant amount of lift and it also needs to be included [13] [36] [34]. Using the geometry determined as in subsection 3.3.1, the wing surface area can be calculated as

$$S_w = 0.5(S_{ref} - S_f) \tag{3.23}$$

with S_f the fuselage area calculated to be

$$S_f = 0.5(l_{f_0} + l_{f_1})(v_1 l_0 - w_{cp}) + (w_{cp} l_{f_0}). \tag{3.24}$$

The total wing span is

$$b = (A\ S_{ref})^{0.5} \tag{3.25}$$

and as the wing starts at the end of the cabin, the span of one wing is

$$b_w = 0.5(b - v_1 l_0). \tag{3.26}$$

The root chord is obtained by

$$c_r = 2\frac{(S_w - S_{blend})}{b_w(1+\lambda)} \tag{3.27}$$

with S_{blend} the assumed area of the blend and λ the taper ratio of 0.35 as suggested in [65] for minimized drag at subsonic Mach numbers. From the definition of the taper ratio, the tip cords follows as

$$c_t = c_r \lambda \tag{3.28}$$

The last parameter that is required to fix the wing planform geometry is the wing sweep. In the first iteration, it is calculated by [38]

$$\Lambda = cos\left(\frac{k_A}{3M_{dd}} + \left(\left(\frac{k_A}{3M_{dd}}\right)^2 - \frac{\frac{t}{c}_{mean}}{3M_{dd}}\right)\right) \tag{3.29}$$

where k_A is the assumed airfoil technology factor, $\frac{t}{c}_{mean}$ the mean thickness-to-chord ratio of the airfoil and M_{dd} the drag divergence Mach number [68]

$$M_{dd} = M_{cruise} + 0.015 \tag{3.30}$$

where M_{cruise} is the cruise Mach number. In next iterations, the actual pressure distribution is considered to obtain the required sweep angle, as explained in subsection 4.2.2.

To determine the longitudinal wing location x_{wing}, the effect of in-flight stability and controllability is inspected. It has to be guaranteed that the aircraft is statically and dynamically stable at any possible flight condition and COG location. The static stability together with the tail sizing is explained in section 7.2 and the dynamic in section 7.3

The wing data used as input as well as the resulting output is presented in Table 3.5. The drawing of the wing planform is included in Figure A.2.

3.3.3. Landing gear

Finally, considering the ground loading as well as the take-off and landing conditions, the landing gear is positioned, which is explained in subsection 7.1.1. The location of the landing gear needs to be checked for compatibility with other components, such that it does not end up at the same location as another component, for example the fuel tank, and sufficient storage room is available as the landing gear should be fully retractable.

Table 3.5: Wing sizing data

(a) Inputs

Parameter	Value	Unit
M_{cr}	0.78	-
λ	0.35	-
S_{blend}	10.55	m^2
M_{dd}	0.795	-
k_A	0.95	-
$\frac{t}{c}_{mean}$	0.0394	-
l_{f_0}	33.0	m
l_{f_1}	19.5	m

(b) Outputs

Parameter	Value	Unit
S_{ref}	284.05	m^2
S_f	185.41	m^2
S_w	49.32	m^2
b	35.75	m
b_w	14.09	m
c_r	4.07	m
c_t	1.42	m
Λ	37.45	°
x_{wing}	13.25	m

3.4. Propulsion system

The propulsion system of an aircraft serves to provide it with the required moving force. Its top level sizing is divided into the engine sizing in subsection 3.4.1 and the fuel tank sizing in subsection 3.4.2.

3.4.1. Engine sizing

With the thrust loading obtained from the wing-thrust loading diagram, the required thrust is evaluated at take-off

$$T_{TO} = \frac{T}{W} MTOW\ g \tag{3.31}$$

and cruise

$$T_{cr} = \frac{C_D}{C_L} MTOW\ g. \tag{3.32}$$

The take-off thrust is used to size the open rotor engines. The method is explained in subsection 6.3.1. The cruise thrust serves to establish the fuel mass flow

$$\dot{m} = T_{cr} TSFC \tag{3.33}$$

which is then used in the fuel tank insulation sizing to determine as the heat exiting the system. The associated method is expanded in subsection 6.2.1. Additionally, the mass flow is passed on to the aircraft performance analysis, see section 8.8, to evaluate the overall flight profile. To simplify the model, the mass flow is treated as constant in this analysis, in reality it is variable and changes mainly with the altitude. The validity of the assumption is also discussed in subsection 6.2.1.

3.4.2. Fuel tank sizing

First, the fuel weight for the maximal range is calculated by Equation 3.6 with Equation 3.2 using R_{max} instead of R_{mis}. This determines the maximal fuel weight required for a flight

$$FW_{max} = 1.05\ MTOW(1 + FF_{max} - FF_{loiter}) \tag{3.34}$$

where FF_{max} is the cruise fuel fraction. This number is then passed to the thermodynamical analysis, explained in subsection 6.2.1, to determine the required fuel tank volume. The fuel tank is located right behind the passenger cabin, from which it is separated by a flat bulkhead. On the outside, it smoothly extends from the pressurized shell. The shape is determined by the oval at the end of the cabin and an oval in the aft fuselage section. The two ovals are connected and at the end of the tank, a circular bulkhead is formed. Due to the interaction with the airfoil outer shape, similarly as for the airfoil shape itself, the geometry is manually adjusted in CATIA. When a suitable geometry is obtained, the outer dimensions are used to determine the structural thickness, as explained in section 5.1. Consequently, the insulation thickness is determined, see section 6.2. The two thicknesses combined form the the wall thickness, which is then offset from the outer volume to obtain the usable inner volume. If the inner volume is not sufficient, the shape and location of the second oval is changed and the process iterated. If such iteration does still not yield a satisfactory result, the fuselage shape is modified for the next iteration. The overview of the input and output data for the propulsion sizing is shown in Table 3.6.

Table 3.6: Propulsion sizing data

(a) Inputs

Parameter	Value	Unit
R_{max}	6200	km

(b) Outputs

Parameter	Value	Unit
FF_{max}	0.0648	-
FW_{max}	4731.0	kg
$\dot{m}$	0.1473	kg/s
T_{to}	202023	N
T_{cr}	34086	N
V_{tank}	75.3	m^3

3.5. Overall configuration

The render of the centercut of the overall configuration is shown in Figure 3.7. The passenger cabin a cockpit is shown in blue, the cargo compartment in yellow, the pressurized shell in green and the fuel tank in red. It can be seen that the fuel tank indeed takes up all the usable place in the back of the aircraft. Additionally, the vertical offset of the cockpit section is seen. The ceiling of the cockpit is at an angle to allow enough headroom for the pilots entering the cockpit. Note the small misalignment at the nose and middle of the aircraft between the pressurized cell and the fuselage's airfoil. At this stage of the design, they are decided to be neglected, as they may be solved with not fully following the oval shape of the cell, but locally flattening it and adequately reinforcing, which in the overall picture would be only a small change.

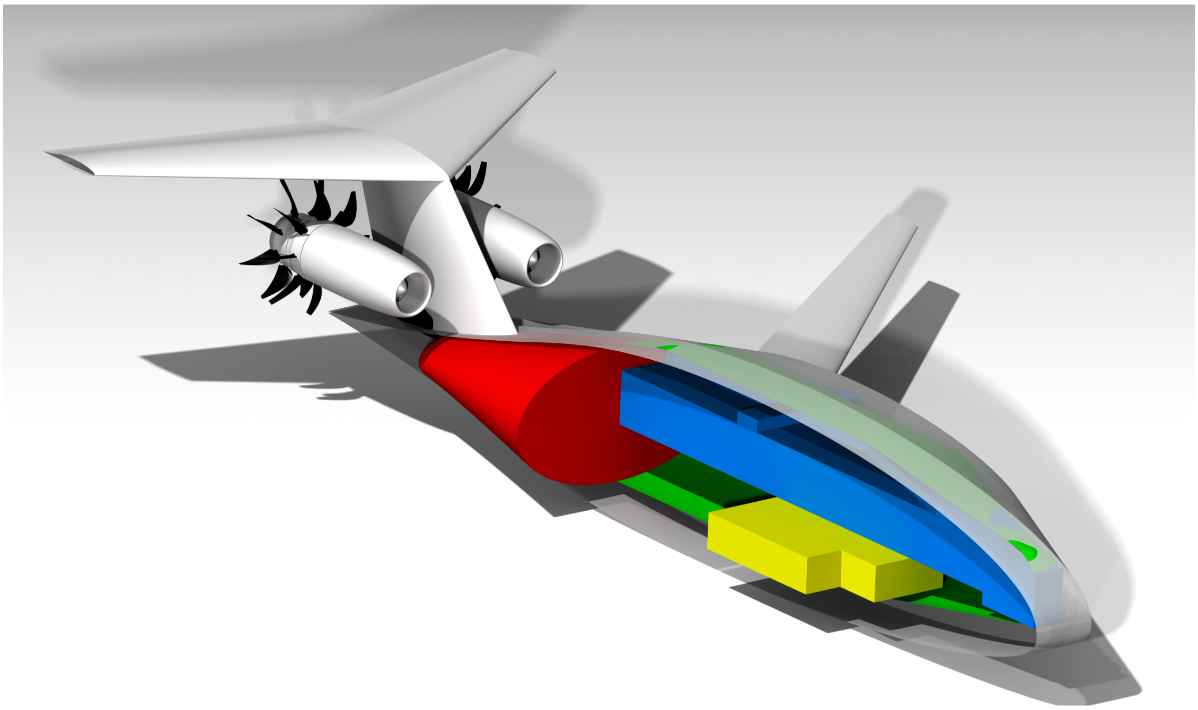

Figure 3.7: Render of the aircraft's configuration

3.6. Class II weight estimation

After the initial iteration, the Class II weight estimation is performed. This is based on the actual geometry of the aircraft, therefore it provides a more accurate result than the Class I weight estimation. The operational empty weight is broken down into

$$OEW_{II} = W_{fixed} + W_{propulsion} + W_{frame} \tag{3.35}$$

with W_{fixed} the weight of the fixed items, $W_{propulsion}$ the propulsion system weight and W_{frame} the structural airframe weight. W_{fixed} is determined as

$$W_{fixed} = W_{fc} + W_{els} + W_{iae} + W_{api} + W_{ox} + W_{fur} + W_{bc} + W_{aux} + W_{pt} \tag{3.36}$$

where the weights are as follows: W_{fc} is the fligh cotrol system, W_{els} the electrical system, W_{iae} the instrumentation, avionics and electronics, W_{api} the air-conditioning, pressurization, anti- and de-icing system, W_{ox} oxygen system, W_{fur} the furnishings, W_{bc} the baggage and cargo handling equipment, W_{aux} the auxiliary and W_{pt} the paint. Each of the mentioned sub-items is calculated by the Torenbeek method for fixed items in [51]. The calculation of W_{frame} is explained in section 5.3 and $W_{propulsion}$ in section 6.2. The description of the items included in the frame and propulsion weights are included in the respective sections.

Table 3.7: Class II weight estimation data

Parameter	Value	Unit
W_{fixed}	14078	kg
$W_{propulsion}$	15113	kg
W_{frame}	27801	kg
OEW_{II}	56993	kg

The results of the class II weight estimation are shown in Table 3.7. Comparing the class II $OEW_{II} = 56993kg$ with the class I estimation $OEW = 47241kg$, a difference of +20% is seen. As the result of the class II estimation are more accurate than from II, as they are based on more physical principles and the actual dimensions and configuration of the aircraft, this means that the aircraft is actually under-designed for its weight. For example, the wings were designed for supporting a smaller weight than they actually would, or the engines are not powerful enough to provide the aircraft with the desired performance. This shows the iterative nature of the design process as mentioned in the introduction of the chapter and shown in Figure 3.1, and with such a large difference, the design should undoubtedly be iterated to achieve a more converging result, at least within a 5% difference. However, the time constrain together with some of the design tools used not being fully automated, this was not achieved for this project. Therefore, this should be also bared in mind when interpreting the results, as it may otherwise lead to falsely optimistic conclusions. For future projects, it is strongly suggested to perform the design iteration.

4 Aerodynamics

The aerodynamic characteristics of the BWB focused strongly on the sizing of the fuselage and wing. The chapter begins with the selection of the airfoil in section 4.1. This is followed by an explanation of the 3-D wing design in section 4.2, this section also presents the results of the analysis on the aerodynamic performance of the aircraft. Next, in section 4.3 the high-lift devices design is presented. Finally, verification and validation methods are explained in section 4.4.

4.1. Airfoil selection

The airfoil selection is one of the key factors that effect aerodynamic performance of a wing or in this case the entire aircraft. Several airfoil characteristics were considered and are described in this section. The various airfoils were analyzed using Xfoil, which is software that can be used to perform a 2-D analysis of an airfoil. In the case of a BWB an airfoil must be chosen for both the center body, which houses the cabin as well as an airfoil for the outer wing section. The center body airfoil must have a thickness-chord ratio (t/c) that can achieve the required height for the cabin at a reasonable aircraft length.

4.1.1. Airfoil camber

The camber line has an effect on the lift and pitching moment of the wing. An increase in camber causes an increase in lift, resulting in an upward shift of the lift curve. However, this also increases the positive pitching moment, meaning a larger tail is required to provide stability.

4.1.2. Airfoil thickness

There are two primary considerations regarding airfoil thickness:

- Maximum thickness: as the (t/c) of an airfoil increases, an increase in $C_{l_{max}}$ was noticeable until a certain point. A thicker airfoil is more likely to stall at the trailing edge as opposed to leading edge stall seen on thinner airfoils. Furthermore, an increased (t/c) leads to an increased drag due to an increase in adverse pressure gradients, especially at higher Mach numbers [11].
- Position of maximum (t/c): The position of maximum (t/c) on an airfoil has an effect on position of peak pressure, thereby altering the lift and drag coefficient. By moving the (t/c) more to the trailing edge, a reduction in drag is noticeable due to a reduction in the pressure peak, caused by a more aft location where transition from laminar flow to turbulent flow occurs [11]. Laminar flow has lower drag, the consequence being that the flow is more prone to separation [11]. A trade-off was made with regards to the position of the (t/c) ratio since a reduction in the pressure peak also means that the pressure difference between the lower and upper surface is smaller and therefore a lower lift coefficient is obtained.

4.1.3. Airfoil critical pressure coefficient

The critical pressure coefficient is the most negative pressure coefficient of an airfoil and an important component in the determination of the critical Mach number of an airfoil. A higher critical Mach number means that higher velocities can be achieved without shock waves occurring. This is important as these local shock waves would cause a significant increase in drag which would greatly reduce the aerodynamic efficiency of the wing.

4.1.4. Summary airfoil selection

This section presents a summary of the different airfoils that were examined as well as show some of the parameters discussed earlier. The airfoil selection has been split up into two, one airfoil is selected for the center body of the blended wing body and another airfoil is selected for the outer wing of the aircraft. Different airfoils were chosen as there are different limitations and options available for this aircraft part.

Center body airfoil selection

Several airfoils have been considered for the center body of the aircraft, these are shown in Table 4.1 and for each the key parameters are indicated. Other airfoils were considered earlier on but were discarded due to obvious limitations of the airfoil, for example it was known that the airfoils should have a relatively high thickness to chord ratio to accommodate the cabin, fuel tanks and cargo compartments. Each airfoil was analyzed using Xfoil.

Table 4.1: Center body airfoil selection at zero degrees angle of attack

Airfoil name	NASA SC-0518	HSNLF-0217	NACA 63-415	NACA 24-020
t/c (%)	17.98	17.00	15.01	20.02
Max. thickness pos. (% chord)	35.35	42.42	34.80	30.0
Max. camber (% chord)	1.47	1.44	2.08	1.73
Max. camber pos. (% chord)	81.82	32.32	55.0	20.8
C_l for $\alpha = 0$	0.431	0.113	0.345	0.199
$C_{p,0}$	-0.958	-0.578	-0.711	-1.029
$C_{l,max}$	1.781	1.451	1.215	1.577
$\max(C_l/C_d)$	76.85	81.18	104.21	91.28

In Xfoil, all airfoils were run at a Reynolds number of 1,000,000. The $C_{p,0}$ was found at an angle of attack of zero degrees. The results obtained with respect to lift coefficient indicated that the supercritical NASA SC-0518 has the best lift performance, with a C_l equal to 0.4310. Another important aspect is the minimum pressure coefficient as this gives an indication of the critical Mach number of the airfoil.

Another critical aspect for the center body airfoil is the thickness of the airfoil as the airfoil must have sufficient height to accommodate the cabin of the aircraft. In this regard the NACA 63-415 airfoil was the least attractive with a maximum t/c of 15.01%. The HSNLF-0217, a natural laminar flow airfoil, meaning that the laminar flow region over the airfoil is extended significantly reducing drag.

A less negative pressure coefficient means a higher critical Mach number which was beneficial as the design cruise speed was chosen to be M = 0.78. In this respect the HSNLF-0217 was the most suitable with a significantly less negative pressure coefficient than the other airfoils that were considered.

The maximum C_l/C_d for each airfoil was also examined as an indication of the aerodynamic efficiency. Despite the 2-D airfoil analysis not including aspects such as induced drag that are very significant it may be used to compare the different 2-D analyses. In this regard the thinnest airfoil the NACA 63-415 exhibits the greatest C_l/C_d, however between the thicker airfoils the differences are much smaller and considering that much of the drag is unaccounted for the differences in reality may be smaller as airfoils such as the natural laminar flow airfoil may have much lower drag.

Finally, the HSNLF-0217 was chosen as the airfoil for the center body as it has enough thickness to accommodate the cabin coupled with the least negative pressure coefficient. In addition the extended laminar flow region will lead to a drag reduction for the center body. The only downside is the relatively low lift coefficient of this airfoil but this is acceptable in part due to the large surface area of the center body which means that sufficient lift will be provided.

Outer wing airfoil selection

Several airfoils have been considered for the outer wing of the aircraft, these are shown in Table 4.2 and for each the key parameters are indicated. The parameters were found using the Xfoil software. Note, other airfoils beside the airfoils shown in Table 4.2 were considered but are not shown for clarity or because they were eliminated early on due to obvious undesirable properties, such as no camber or very negative minimum pressure coefficient.

Table 4.2: Outer wing airfoil selection

Airfoil name	Eppler-1213	HSNLF-0213	NLF-0414F	NACA 63-415	NASA SC(2)-0614
t/c (%)	17.41	13.26	14.17	15.01	13.99
Max. thickness pos. (% chord)	22.2	43.6	46.6	34.80	36.1
Max. camber (% chord)	1.98	1.33	2.39	2.08	2.04
Max. camber pos. (% chord)	34.1	33.7	51.3	55.0	82.0
C_l for $\alpha = 0$	0.176	0.108	0.312	0.345	0.485
$C_{p,0}$	-1.007	-0.457	-0.589	-0.711	-1.009
$C_{l,max}$	1.674	1.423	1.469	1.215	1.677
max (C_l/C_d)	101.83	95.48	89.67	104.21	78.91

The outer wing airfoils were less restricted than the center body airfoil with respect to height. For this reason some thinner airfoils were considered. For the outer wing two natural laminar flow airfoils were considered, namely the HSNLF-0213 and the NLF-0414F. Again these were examined due to the extended laminar flow region of the airfoil reducing drag. The Eppler-1213 and NASA SC(2)-0614 both turned out to be relatively inadequate for this aircraft due to their $C_{p,min}$ being such a large negative value. It was also found that despite having seemingly favorable characteristics the NLF-0414F was designed for relatively low Mach numbers [69], thus this option was also not chosen.

Ultimately, the thinner natural laminar flow airfoil, the HSNLF-0213 was chosen as the airfoil for the outer wing. This was due to the suitable $C_{p,min}$ value as well as a sufficient $C_{l,max}$. The pressure graph for the selected HSNLF-0213 airfoil at is given in Figure 4.1.

4.2. 3-D wing design

Utilizing the selected airfoils and the plan-form determined from preliminary sizing, a model of the BWB was created in XFLR5. This model was analyzed using XFLR5 as this software allows for the analysis of finite wings. This analysis is required to examine the aerodynamic performance of the BWB when considering finite wing effects such as induced drag.

4.2.1. Critical mach number

The critical Mach number (M_{cr}) of the wing must be attained such that the aircraft does not encounter shock waves at cruise speed, which would significantly increase drag. The calculation of the critical Mach number follows three steps. First, the minimum pressure coefficient at low-speed incompressible flow was attained using Xfoil. The minimum pressure coefficient (C_p, 0) at an angle of attack of zero at the inviscid condition for the HSNLF-0213 was found to be -0.5. Next, this value was inputted in the Karman-Tsien compressibility correction,

$$C_p = \frac{C_{p,0}}{\sqrt{1 - M_\infty^2} + [M_\infty^2/(1 + \sqrt{1 - M_\infty^2})]C_{p_0}/2} \tag{4.1}$$

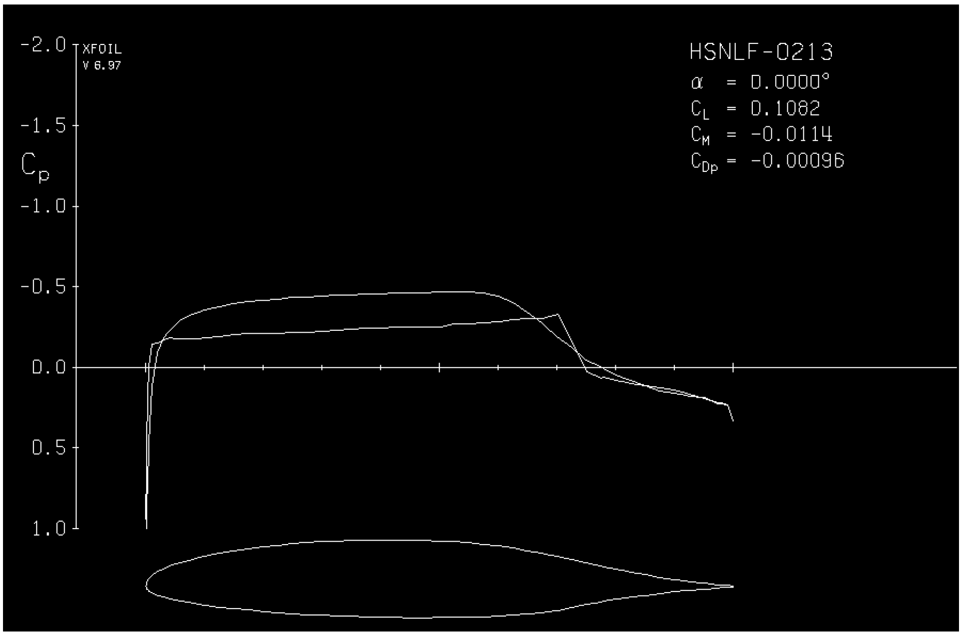

Figure 4.1: HSNlF-0213 pressure distribution at $\alpha = 0$

at a cruise Mach number (M_∞) of 0.78 the pressure coefficient was found to be -0.940. Then the critical pressure coefficient, $C_{p_{cr}}$, was determined using

$$C_{p_{cr}} = \frac{2}{\gamma M_\infty^2}\left(\left(\frac{2+(\gamma-1)M_\infty^2}{\gamma+1}\right)^{\frac{\gamma}{\gamma-1}} - 1\right) \tag{4.2}$$

Where γ is the heat capacity ratio and taken to be 1.4 for air, this yielded a critical pressure coefficient of -0.494 at the cruise Mach number. Solving Equation 4.1 and Equation 4.2 simultaneously, a critical Mach number of 0.695 is obtained. The same method is applied to both the body and outer wing, however the process is only shown for the outer wing.

It should be mentioned that the Xfoil also implements the Karman-Tsien rule as a compressibility correction, which is of greater accuracy than the Prandtl-Glauert rule as it attempts to account for some nonlinear aspects of the flow.

4.2.2. Wing sweep

As presented in subsection 4.2.1, the critical Mach number of the wing is below the cruise Mach number, which is an issue as shock waves would occur. Therefore wing sweep was added in order to increase the critical Mach number. The required sweep is obtained using [62]

$$\Lambda_{LE} = \cos^{-1}\left(\frac{M_{cr}}{M_{cr_{swept}}}\right)^2 \tag{4.3}$$

Inputting $M_{cr} = 0.695$ and $M_{cr_{swept}} = 0.78$ a required leading edge sweep angle of 37.45° was calculated.

4.2.3. Mach drag divergence number

In order to ensure that the aircraft will not encounter shock waves after the critical Mach number is met, the Mach drag divergence number was checked. The Mach drag divergence number can be obtained using [62]

$$M_{dd} = \frac{k_a}{\cos\Lambda} - \frac{(t/c)}{\cos^2(\Lambda)} - \frac{C_{L_{des}}}{10\cos^3(\Lambda)} = 0.87 \tag{4.4}$$

Where k_A is the airfoil technology factor taken as 0.95, $C_{L_{des}}$ the lift coefficient at cruise taken as 0.25. From this, a Mach drag divergence of 0.87 is obtained.

4.2.4. Wing twist

The use of wing twist is an important aspect in the consideration of stability, especially as sweep has been used, which causes a greater pitch-up moment. It is desirable for the wing tip to stall after the root stalls such that the control devices at the tip of the wing are still effective and able to maneuver the aircraft out of a stall. The use of wing twist has been utilized to delay the tip stall by ensuring that the root of the wing stalls first. A wing twist of 3.5 degrees is added to the outer wing to increase its effective angle of attack, this is based on statistics that 3-5 degrees of wing twist is typically provides adequate stall characteristics [47]. The twist is applied at the root and linearly reduces along the span of the outer wing until the wing tip; where the wing twist is 0°.

4.2.5. XFLR5 analysis

The analysis of the entire BWB was done in the XFLR5 software package. Firstly the model of the aircraft based on the preliminary sizing and the chosen airfoils a model had to be created. For the purpose of this analysis the entire blended wing body including empennage is modeled, for the empennage sizing and airfoil selection for the tail the reader is referred to subsection 7.2.2. **Unfortunately, the software does not allow accurate modelling of the aft mounted engines thus these are excluded from this analysis. The model that was used for the analysis is shown in Figure 4.2.**

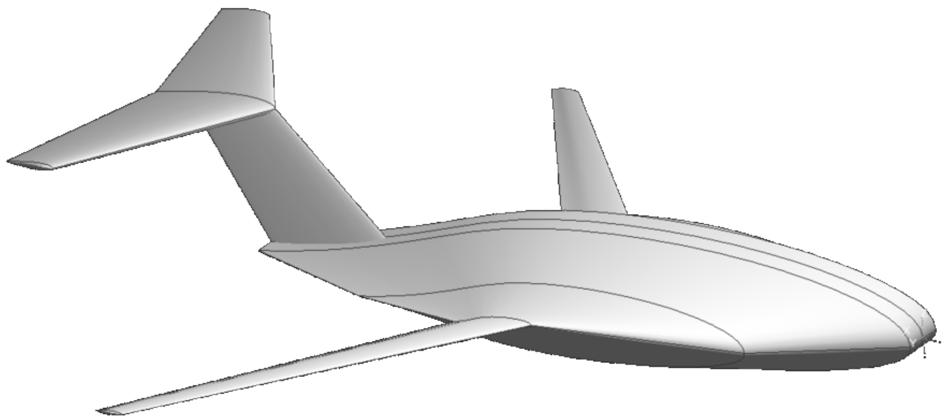

Figure 4.2: Model of the BWB used for the aerodynamic analysis in XFLR5

Aerodynamic efficiency

The aerodynamic efficiency of the BWB is measured using the lift-to-drag ratio, L/D or equivalently C_L/C_D. The C_L/C_D is found over a range of angle of attack from −5° to 11° which is when the XFLR5 methods stop converging. The C_L/C_D plotted against angle of attack, α is shown in Figure 4.3.

From Figure 4.3 it can be observed that the greatest aerodynamic efficiency is 21.5 which is achieved at an angle of attack of 3°. Aerodynamically, flying at this angle of attack during cruise would be optimal. It can be observed that the aerodynamic efficiency decreases fairly rapidly if the angle of attack were reduced from optimum angle of attack, this is expected as the angle of attack would rapidly become negative. Increasing the angle of attack beyond 3° it is observed that the C_L/C_D starts to decline albeit at a much slower rate compared to when the angle of attack is decreased.

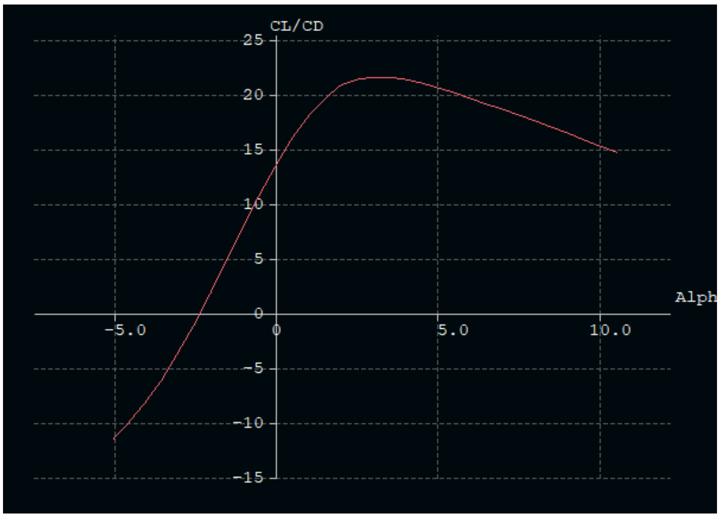

Figure 4.3: The aerodynamic efficiency of the BWB as the angle of attack varies

Maximum clean lift coefficient

Another important aerodynamic aspect that is of interest is the maximum clean lift coefficient as this will determine the required ΔC_L that must be provided by high lift devices. The C_L-α curve is shown in Figure 4.4

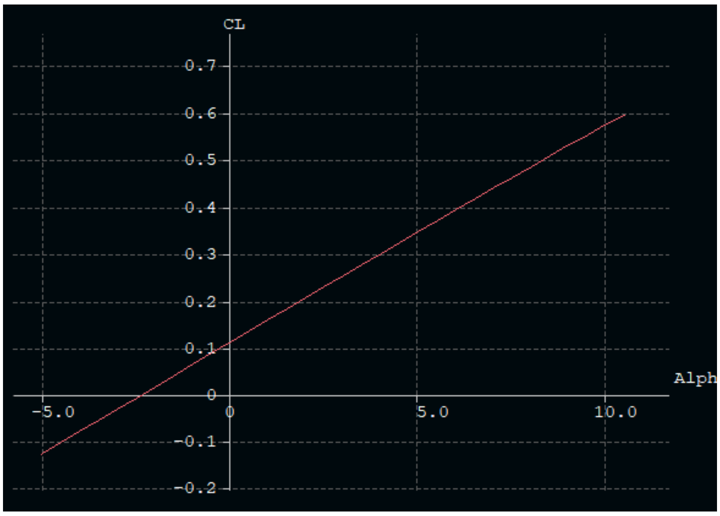

Figure 4.4: C_L-α of the entire aircraft

Unfortunately, due to the limitations of XFLR5 the solution stops converging past 11.5°. The reason the solution stops converging is because the interpolation of the viscous drag from the 2-D approximation has reached its limit and can no longer be estimated [19]. However, it is known that other aircraft, such as the Boeing 737, typically have a critical angle of attack of around 15° [1]. For this stage in the design a similar critical angle of attack was assumed, giving an estimated $C_{L,max,clean} = 0.65$. In addition to statistical data the $C_{l,max}$ obtained from the airfoil analysis yields occurs at an angle of attack of 20.5° for the HSNLF-0213 airfoil. This can be used an as indication that greater angles of attack can possibly be achieved beyond the found 11.5°. Further analysis, likely utilizing a CFD analysis, will be required to accurately determine the C_L of the aircraft at higher angles of attack.

[1] URL `http://airfoiltools.com/airfoil/details?airfoil=b737a-il` [cited 25/06/2018].

Drag bucket

The drag bucket refers the a region in the C_L vs. C_D plot where the lowest drag is experienced for a certain C_L range. The C_L vs. C_D plot for the aircraft is shown in Figure 4.5

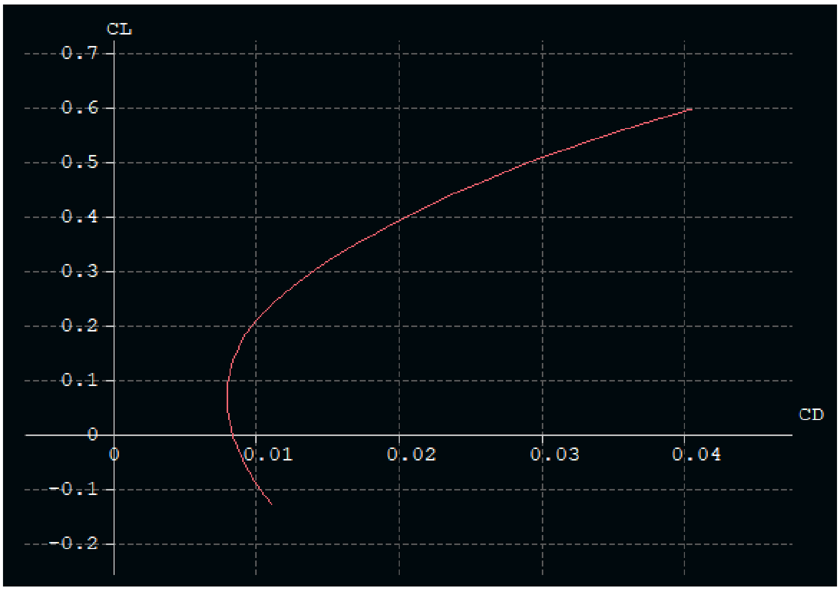

Figure 4.5: C_L vs. C_D of the entire aircraft

As can be seen in Figure 4.5 C_D is minimized when C_L is just below 0.1, the C_D is approximately 0.008. There is no clear drag bucket visible for the entire aircraft for which the drag is significantly lower.

4.3. High-lift devices

During various stages of flight a range of different lift is required. In order to satisfy the lift required at take off and landing condition whilst maintaining a reasonable drag at cruise, the implementation of high lift devices are required.

Table 4.3: Lift coefficient during various flight phases

$C_{L_{max}}$ clean configuration	0.65
$C_{L_{max}}$ at take-off	1.1
$C_{L_{max}}$ at landing	1.3

It is observed that the critical condition, which is when the maximum lift is needed, occurs in landing condition. Therefore an increase in the lift coefficient of 0.65 (ΔC_L) must be achieved through the use of high lift devices.

The sizing of flaps was determined by several key parameters. For the design, it was first assumed that a double slotted Fowler flap system would be used at the trailing edge with a take-off deflection angle of 20 degrees and a landing deflection angle of 50 degrees [61].

4.3.1. Chord ratio

An overview of various airfoil dimensions are given in Figure 4.6 to supplement understanding of this section. c is the airfoil chord with retracted flaps, c' is the airfoil chord with deployed flaps, c_f is the flap chord, Δc is the difference between c' and c, and δ_f is the angle of flap deployment, with anti-clockwise positive.

The first step is to find the chord ratio; $\frac{c'}{c}$. This value is obtained through utilizing the relationship between the deflection angle of the flap and the ratio $\frac{\Delta c}{c_f}$. From Figure 4.7 line IIb, using 20 degrees and 50 degrees

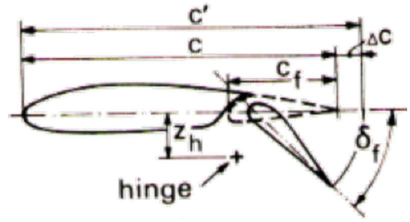

Figure 4.6: High-lift device dimensions [61]

flap deflection, values of 0.58 and 0.85 were obtained respectively for $\frac{\Delta c}{c_f}$. To obtain Δc, a flap chord length needed to be estimated. For take-off and landing configuration cases the flap chord is taken to be at 0.33 of the chord, such that the flap is attached to the rear spar and 7% of the chord is left to control systems between the nested flap and the rear spar [61]. The Δc is then obtained to be 0.191 and 0.281 for take-off and landing condition respectively. This results in a c' of 1.191 for take off and 1.281 for landing.

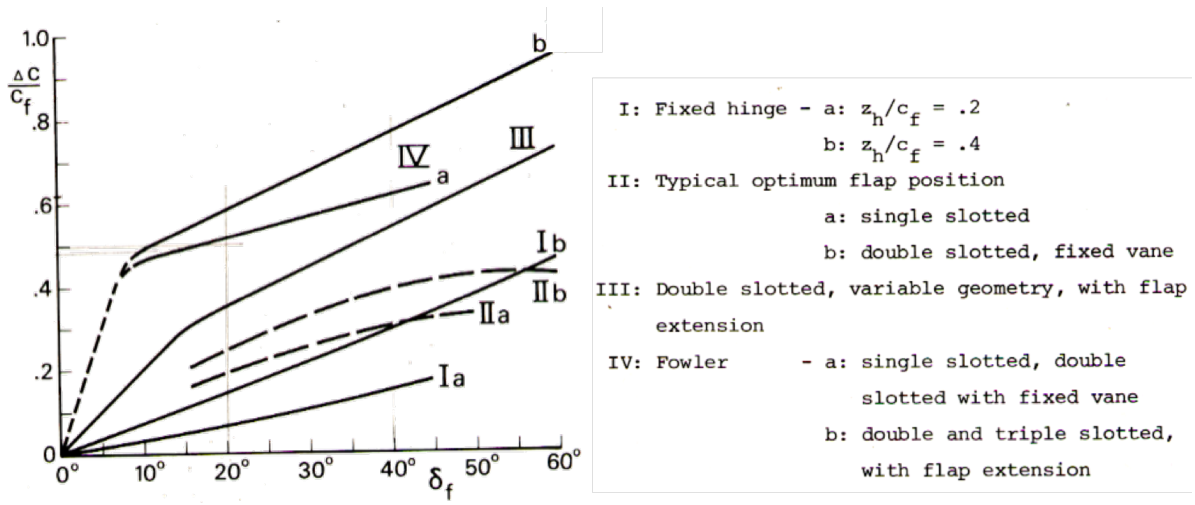

Figure 4.7: Flap deflection against $\frac{\Delta c}{C_f}$ [61]

4.3.2. Flap reference wing area

The reference wing area (S) is required to obtain a planform of the wing. The reference flap area will be based on the landing condition as the landing condition requires the greatest increase in lift. The reference flap area (S_{wf}) was found by rearranging

$$\Delta C_{L_{max}} = 0.9 \cdot \Delta C_{l_{max}} \cdot \frac{S_{wf}}{S} \cdot \cos(\Lambda_{hingeline}) \tag{4.5}$$

From Table 4.3 the required values of $\Delta C_{L_{max}}$ are 0.45 for take-off and 0.65 for landing. The hinge line is taken to be 30.5° from the wing planform. $\Delta C_{l_{max}}$ is calculated from

$$\Delta C_{l_{max}} = 1.6\frac{c'}{c} \tag{4.6}$$

Using the chord ratio found in subsection 4.3.1 $C_{l_{max}}$ was found to be 1.906 for take-off and 2.049 for landing [61]. Using these values and rearranging the Equation 4.5, the area ratio; $\frac{S_{wf}}{S}$ was calculated to be 0.338 for take off and 0.441 for landing. Next, the outer wing area can be found using

$$S = (c_r + c_t)h \tag{4.7}$$

The outer wing area (S) was found to be $75.2m^2$. Since the landing configuration is the critical case, only the landing configuration will be considered further. This results in total flap area (S_{wf}) of $33.1m^2$, thus $16.6m^2$ per wing.

4.3.3. Flap span

The flap span needs to be determined in order to ensure there is no conflict with other wing objects. The flap area has already been obtained and can be used to determine the span of the flaps through the use of

$$A_{flap} = x_{flap} * \left(\frac{c_1 + c_2}{2}\right) = 16.6m^2 \tag{4.8}$$

Where A_{flap} is the flap reference area of one wing, x_{flap} is the spanwise distance of c_2 from c_1, c_1 is the chord length at 0.5m from the root chord, this the point at which the flaps will start, and is equal to 3.88m based on the wing planform. Finally, c_2 is the chord length at the end of the flap nearer to the tip of of the wing. Through the use of the geometric relationship

$$c_2 = c_1 + x_{flap}\tan(\Lambda_{TE}) - x\tan(\Lambda_{LE}) \tag{4.9}$$

the equations can be solved simultaneously to determine the flap span and the chord at the outer edge of the flaps. From the wing geometry, the leading edge sweep angle (Λ_{TE}) is known to be 29.7°, and the trailing edge sweep angle (Λ_{LE}) is 37°. Solving Equation 4.8 and Equation 4.9 simultaneously, and taking the positive value, c_2 is found to be 3.00 m and x_{flap} is found to be 4.83m.

4.3.4. Shifting of the lift curve

The addition of high lift devices is to increase the lift coefficient such that the required lift during landing and take-off can be reached without the need for an oversized wing.

A value of $-15°$ is taken for the shift in the zero lift airfoil angle of attack ($\Delta\alpha_{0L_{airfoil}}$) for landing configuration and $-10°$ degrees for take off configuration [61]. Plugging the remaining values as obtained from subsection 4.3.2, the change in the zero lift angle of attack of the aircraft ($\Delta\alpha_{0L}$) is found as $-5.7°$ using Equation 4.10. As a double slotted Fowler flap also does increase the wing surface area, a correction must be made to the lift slope of the flap. The lift curve slope in clean configuration ($C_{L\alpha-clean}$) is 0.0463 and thus with flaps deployed is obtained using Equation 4.11 and found to equal 0.0521.

$$\Delta\alpha_{0L} = (\Delta\alpha_{0L})_{airfoil}\frac{S_{wf}}{S}\cos\Lambda_{hingeline} \tag{4.10}$$

$$C_{L\alpha flapped} = \left(1 + \frac{S_{wf}}{S}\left(\frac{c'}{c} - 1\right)\right)C_{L\alpha-clean} \tag{4.11}$$

Plotting the lift curve in the flapped configuration as the orange line on Figure 4.8, it can be seen that a max lift coefficient of 1.3 will be attained at 17.5° angle of attack. This angle of attack is too high, therefore the flaps reference area must be increased to meet a target angle of attack of 14° at the maximum lift coefficient. 14° value is relatively high but still falls in the range of take off angles for conventional transport aircraft [61]. To reach angle of attack, a leftward shift of the lift curve of approximately 3° is required, accounting for the change in lift slope too. Referring back to Equation 4.10 and Equation 4.11, the $\frac{S_{wf}}{S}$ required to achieve a $\Delta\alpha_{0L}$ of -8.7 is 0.673, resulting in a flapped lift curve slope of 0.0551. The flap reference area is recalculated to be 25.3, c_2 is 2.4m and x_{flap} is 8.05. The new lift curve is plotted as the greyline.

During the redesign phase, the implementation of slats was considered. However, given the limited space at the leading edge of the wing due to the front spar's presence at 10% chord, and the effect of slats to provide a delayed stall but limited lowering of required angle of attack it was determined to not implement them. Related to this second point, while the slats will allow for a delay in stall, the angle of attack needed to reach the $C_{L_{max}}$ of 1.3 will largely remain the same, which will likely provide a problem with scrape back angle as will be discussed in section 7.1

A summary of the flap sizing is given in Table 4.4 and a wing planform with the flap positioning is given in Appendix A.

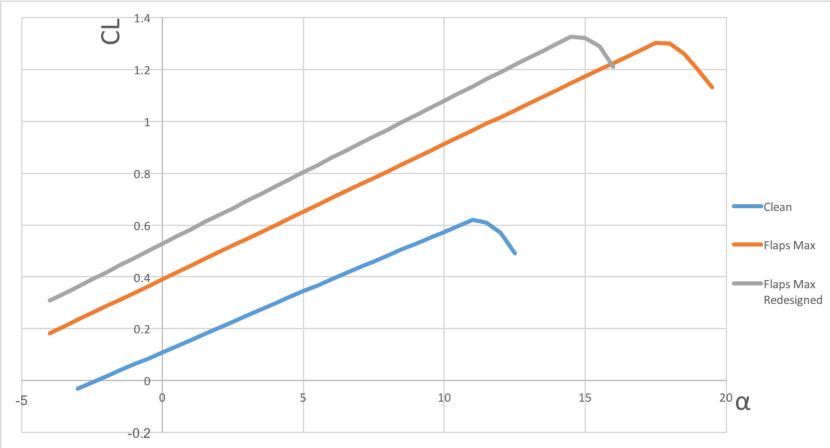

Figure 4.8: $C_L - \alpha$ curve in clean and flapped configuration

Table 4.4: Summary of flap sizing

Double Slotted Fowler Flap	Value
$\frac{c'}{c}$ [-]	1.281
$\frac{S_{wf}}{S}$ [-]	0.673
b_{flap} [m]	8.05
Reach on outer wing [-]	0.04 to 0.58

4.3.5. Flap deployment mechanism

Due to the need of flaps only during certain stages of flight, deployment mechanism and actuators need to be in place such that the flap can be deployed and retracted. Two flap deployment mechanisms were considered; the rolling track mechanism and the four bar mechanism.

Rolling Track Mechanism

The rolling track mechanism was developed by Martin F. Stephenson. For this mechanism, an actuator pushes the flaps aft along a set of tracks by rollers as shown in Figure 4.9. The advantage of this system is the high accuracy in flap positioning and the light weight of the mechanism [57]. The disadvantages of this system is the large mechanism, the fact that the flaps cannot be folded away, and the rotating parts being susceptible to jamming at high speeds [57].

Four-Bar Mechanism

The four bar mechanism is a common flap deployment mechanism used as shown in Figure 4.10. The working principle of this mechanism is that the rotation of a single link near the rear spar causes a chain reaction that sets all following links in motion, thereby leading to the deployment of the flap. The advantage of the four-bar mechanism over the rolling track mechanism is the greater compactness in storage due to systems foldability. Therefore, a low drag can be realized as the fairing for the high lift devices can be relatively small. The main disadvantage of this mechanism is the increased complexity, which leads to greater maintenance.

Upon comparison of the two high lift devices, it was determined that the four-bar mechanism would be used due to requiring less room in the wing and a smaller fairing.

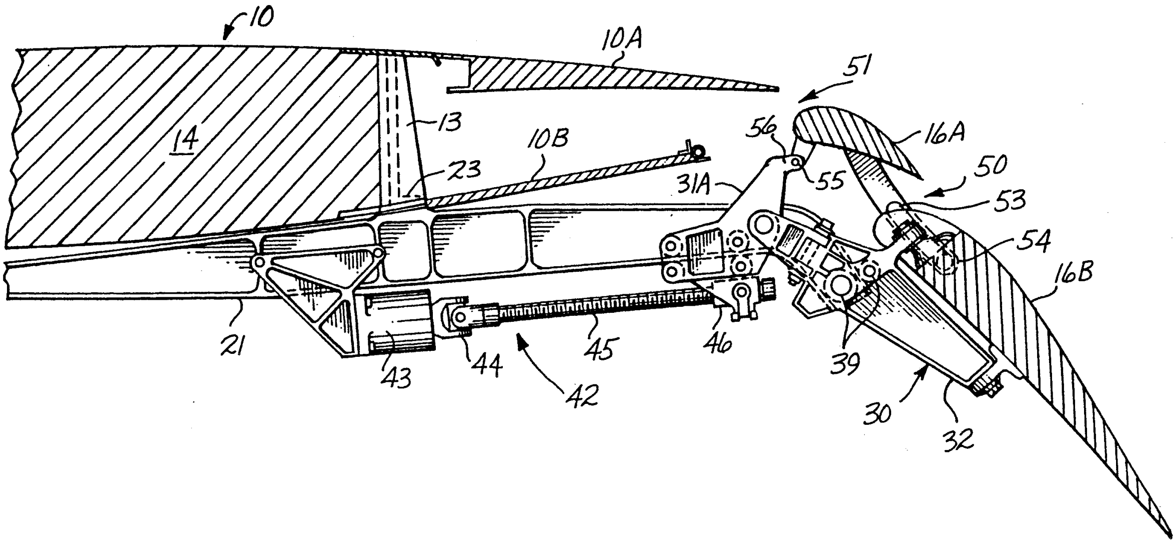

Figure 4.9: Rolling track flap mechanism [63]

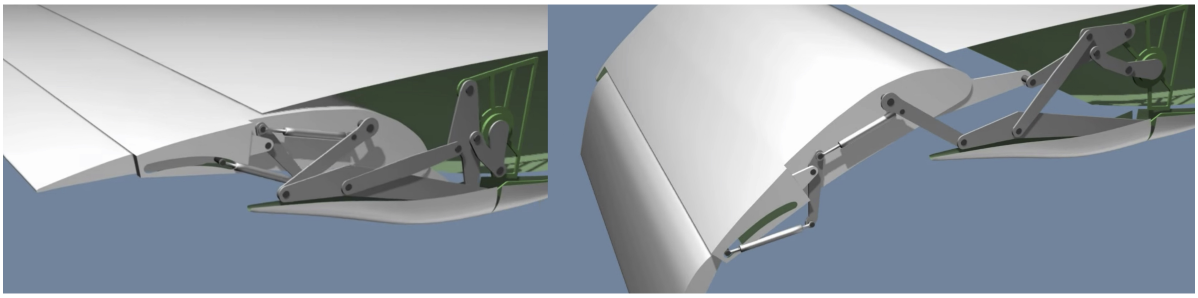

Figure 4.10: Four bar flap mechanism[2]

4.4. Verification and Validation

This section describes the verification and validation of the results obtained in the aerodynamic analysis. The aim is to present insight into the reliability and accuracy of the methods utilized in the aerodynamic analysis.

4.4.1. Verification

The primary means used to perform the aerodynamic analysis are the two software applications that have been used namely; Xfoil and XFLR5. The primary means of verification has been to examine the various outputs of the program and check whether or not they follow the expected trend. For example, the outputted $C_l - \alpha$ plots followed the expected trend of having a positive slope for relatively small angles of attack. Similar checks were performed for the $C_d - \alpha$, $C_l/C_d - \alpha$ and $C_l - C_d$ plots and all followed the expected trend. Although this is only a rudimentary verification method it does give insight that the program appears to be working in accordance with expectations. Further, verification is difficult as there is insufficient time to closely examine the intricacies of XLFR5 or Xfoil.

4.4.2. Validation

For validation of the HSNLF-0213, results obtained from XFLR5 were compared to those as obtained by NASA in wind tunnel testing. The data as obtained from NASA was classified into 3 sections, namely 2-D low speed

[2]URL `https://www.youtube.com/watch?v=kKDMjc3l_gw` [cited 26/06/2018.

performance, 2-D high speed performance, and 3-D test including the use of high lift devices[59].

For validation of the 2-D aerodynamic analysis of the HSNLF-0213, the C_l vs. C_d plot as obtained from the XFLR5 analysis was compared to that experimentally obtained wind tunnel testing from NASA. An overlay of the results from NASA and XFLR5 is shown in Figure 4.11. It should be noted that fewer points are present for the NASA data, and linear interpolation between points was completed as originally found in the NASA results.

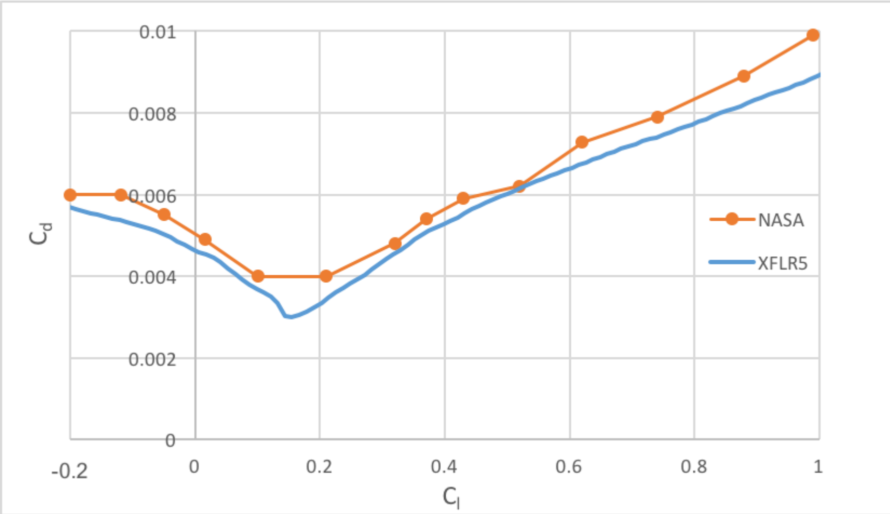

Figure 4.11: NASA wind tunnel results and XFLR5 data for the NLF-2013 at Reynolds number $9x10^6$ [59]

Comparing the NASA data with the XFLR5 data, it can be seen that the general trend of the XFLR5 results strongly resembles that as obtained from the NASA wind tunnel. The lowest C_d of both results occur at a similar C_l of approximately 0.15 for both the wind tunnel and XFLR5 model. One discrepancy that is observed is that in general, the XFLR5 model tends to underestimate drag, with the lowest $C_d \approx 0.003$ in XFLR5 against $C_d \approx 0.004$ as seen in the wind tunnel data. This was expected when using XFLR5 as according to its documentation XFLR5 tends to underestimate drag which would help explain the discrepancy [18]. It is also noticeable that at higher C_l values, a greater divergence between C_d values is observed. As an increase in C_l can be modelled as a function of angle of attack with a higher C_l value representing a higher angle of attack value, it can be expected that greater flow separation occurs at higher C_l. Due to difficulty in analyzing separation, it is expected that there is a decrease in the accuracy of XFLR5 at higher C_l. Nonetheless, at a C_l of 1, the difference is still within 15%, which is within a reasonable range. In addition, no significant amount of aerodynamic analysis was performed in XFLR5 at very high angles of attack, and therefore does not hamper the performed aerodynamic analysis in this report. For this reason, it can be said that the 2-D airfoil data as obtained from XFLR5 is verified. As the center body airfoil; the HSNLF-0217 was adapted from the HSNLF-0213, there is currently no available wind tunnel test data to evaluate the XFLR5 results obtained for this airfoil. However, due to similar characteristics between the HSNLF-0217 and HSNLF-0213, it is reasonable to assume that similar validation results will be obtained.

Validating the results obtained in the 3-D analysis is of greater difficult as this can only be done by comparing the XFLR5 results to experimental wind tunnel tests or full scale aerodynamic test performed during flight tests. This is reserved for a much later stage in the development of the aircraft once the entire design has been determined. However, in the next phase of the design the aerodynamic performance will also be analyzed using CFD. This should hopefully provide a better indication of the accuracy of XFLR5.

Despite being unable to perform complete validation of the 3-D aircraft certain aspects of the results can be examined. Firstly, similar to the 2-D analysis, XFLR5 will tend to underestimate the drag when performing the 3-D analysis. One of the reasons this could be the case is due to XFLR5 interpolating the viscous drag from the 2-D airfoil analysis, which may lead to an optimistic estimation of the viscous drag [18]. Additionally, XFLR5 is unable to model wing-fuselage interaction, which again may be a cause for an underestimation of drag.

5 Structures

The structure of the aircraft needs to be able to carry all the loads on the aircraft. For this report the cabin and wing box structure were designed and analyzed, since these are the main carrying structures. The cabin structure design is explained in section 5.1. In section 5.2 the wing box design is presented.

5.1. Cabin

To optimize the cabin shape to fit the center body airfoil shape as presented in Chapter 4, it was chosen to shape the cabin cross section as an oval.

5.1.1. Pressurization method

First, the cabin skin was analyzed for pressurization, and a skin thickness calculated based on the stresses found in the analysis.

Due to the limited resources and time available for the preliminary design phase, assumptions were made to simplify the structure. The assumptions made are:

- The stresses are only tangential in the skin, so no shear stresses in the cabin skin.
- The ellipse is symmetric in the horizontal and vertical plane, therefore the stresses will also be symmetric in those planes.

Hoop stress

When an oval shape is pressurized, contrary to a cylindrical shaped cabin, σ_{hoop} (hoop stress) will not be constant over the cross section. Therefore, the thickness of the skin will be designed to vary. The hoop stress can be determined using [9]

$$F_p = \sigma_{hoop} t_{skin}(\theta) = \Delta P \int_0^{\frac{\pi}{2}} sin(\phi(\theta)) R_{ellipse}(\theta) d\theta \tag{5.1}$$

Where F_P is the tangential force in the skin due to the internal pressure, $t_{skin}(\theta)$ the skin thickness, $\phi(\theta)$ the angle between the horizontal axis and the perpendicular with the skin, $R_{ellipse}(\theta)$ the ellipse radius and θ the ellipse angle as can be seen in Figure 5.1. In this figure $\sigma_{hoop,h}$ is the horizontal hoop stress and $\sigma_{hoop,v}$ is the vertical hoop stress.

The expression to determine the ellipse shape is

$$\frac{h^2}{b^2} x^2 + y^2 = h^2 \tag{5.2}$$

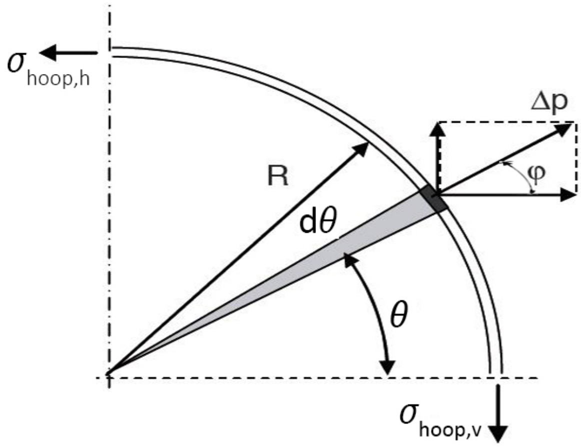

Figure 5.1: Equilibrium between pressure in ellipse and σ_{hoop} [9].

Where b is the semi-major axis and h is the semi-minor axis as can be seen in Figure 5.2. By implicitly differentiating Equation 5.2

$$\frac{dy}{dx} = -\frac{h^2}{b^2}\frac{x}{y} \tag{5.3}$$

is found. This expression can be used to determine the relation between ϕ and θ by converting Equation 5.3 to polar coordinates and taking the arctangent of this expression, which yields

$$\phi = arctan(\frac{b^2}{h^2}\frac{sin(\theta)}{cos(\theta)} \tag{5.4}$$

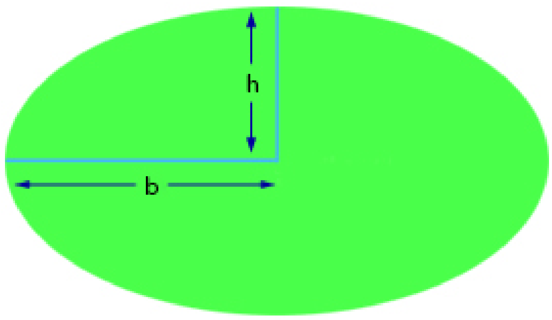

Figure 5.2: Ellipse dimensions

Converting Equation 5.2 to polar coordinates yields

$$R_{ellipse}(\theta) = \frac{h}{\sqrt{\frac{h^2}{b^2}cos^2(\theta) + sin^2(\theta)}} \tag{5.5}$$

This way the radius of the ellipse is expressed in terms of the angle θ. The final expression to determine the thickness over the cabin skin for constant σ_{hoop} is

$$t_{skin}(\theta) = \frac{\Delta P}{\sigma}\int_0^{\frac{\pi}{2}} sin(arctan(\frac{b^2}{h^2}\frac{sin(\theta)}{cos(\theta)}))\frac{h}{\sqrt{\frac{h^2}{b^2}cos^2 + sin^2}}d\theta \tag{5.6}$$

This is integral is difficult and time consuming to evaluate analytically, therefore it is analyzed numerically. The ellipse will only be analyzed from $\theta = 0$ to $\theta = \frac{\pi}{2}$, since arctan can only be evaluated between these points. So, to get the thickness for the full ellipse the thickness of the first quarter ellipse will be mirrored in the horizontal and vertical plane.

Longitudinal stress

Besides σ_{hoop}, σ_{long} (longitudinal stress) will also be analyzed. This is done using longitudinal equilibrium as is displayed in Figure 5.3. The area of the ellipse is

$$A_{ellipse} = \pi bh \tag{5.7}$$

and the area of the skin cross section is[1]

$$A_{skin} \approx \pi(b+h)(1+\frac{3a}{10+\sqrt{4-3a}})t_{skin} \tag{5.8}$$

where

$$a = \frac{(b-h)^2}{(b+h)^2} \tag{5.9}$$

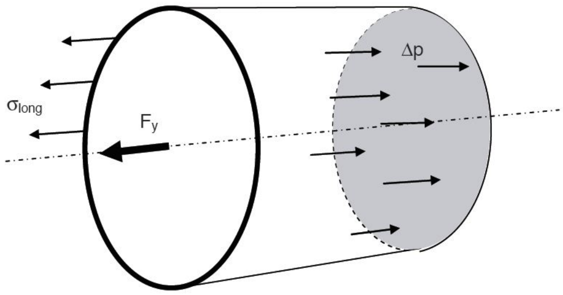

Figure 5.3: Equilibrium between longitudinal stress and pressure [9]

Using Equation 5.7 and Equation 5.8 the equilibrium is

$$F_{long} = A_{skin}\sigma_{long} = \Delta P A_{ellipse} = F_p \tag{5.10}$$

The longitudinal stress expression is

$$\sigma_{long} = \Delta P \frac{A_{ellipse}}{A_{skin}} \tag{5.11}$$

The skin thickness was first sized for the hoop stress using the method from subsection 5.1.1. Following this a sizing was done for the longitudinal stresses present, sing the method described in Equation 5.1.1, yet the thickness required for this was much lower and thus this was not the determining factor in the skin thickness sizing.

5.1.2. Materials selection

The materials are selected by analyzing the different material stresses and densities, then reiterating this into the stress analyses described in subsection 5.1.1.

The fatigue stress of the material was first looked at as a limit stress, yet the fatigue stress is measured with a cycle mean stress of zero. The cabin pressure cycle however, will be varying from zero stress to the maximum stress achieved in the pressurization, thus the mean stress of the cycle will be half of this maximum stress, and will equal the amplitude stress of the cycle. Thus the value of stress at which the material will fail must be adapted from the fatigue stress such that the mean stress and the amplitude stress are equal. Thus, in order to find where the amplitude and mean stress were equal, a line was drawn between the point where the

[1] URL `https://www.mathsisfun.com/geometry/ellipse-perimeter.html` [cited 25 June 2018].

amplitude stress was equal to the fatigue stress (mean stress equals zero), and the point where the amplitude stress equals zero, or just the ultimate stress of the material. This line was called the failure line as it is the combination of amplitude and mean stress at which the material will fail after 5e8 cycles, and can be seen in Figure 5.4, which shows how the limit stress was found for Al2024-t3.

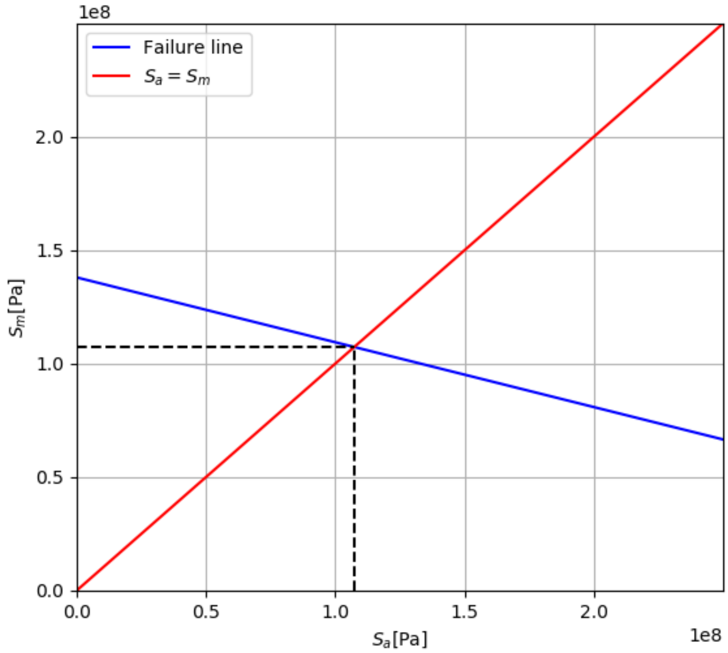

Figure 5.4: Plot showing maximum varying amplitude and mean stress for 5e8 cycles for Al2024-t3, where the dotted lines show the value where the amplitude and mean stress are equal.

In order to find the point where the mean and amplitude stress are equal, an $S_m = S_a$ line is drawn at 45 degrees from the origin, and the intersection of these two lines taken as the amplitude stress. As seen in Figure 5.4, the amplitude stress for Al2024-t3 was found to be approximately 110$[MPa]$, thus, if the stress caused by the cabin pressure is 220$[MPa]$ then the skin would fail after 5e8 cycles. Thus, taking into account a margin of safety of approximately 1.4, the analysis was performed using a limit stress of 160$[MPa]$ for Al2024-t3. There is also a large margin of safety taken into account with the number of cycles since the cabin will be pressurized much less than 5e8 times throughout the total life cycle.

Using this process and finding the limit stress for each material from the fatigue stress, including the safety factors mentioned, each of the materials shown in Table 5.1 was analyzed. As can be seen in the table, the titanium alloy allowed for the lightest cabin skin, yet this yielded a skin thickness of approximately 0.35$[mm]$, which is not able to be manufactured. Also, in [3] it was already established that titanium parts will be too expensive to manufacture.

The next lightest option was Al7075-t6, yet, looking more at the material properties, it was decided that due to the low ductility of 7075, cracks may grow too quickly and fail before a proper inspection is performed. Thus it was decided that Al2024-t3 would be the most optimal material choice for the cabin of the aircraft.

Material	$\sigma_{fatiguelimit}$ [MPa]	$\sigma_{ultimate}$ [MPa]	σ_{limit} [MPa]	ρ $[kg/m^3]$	E [GPA]	m [kg]
Al2024-T3	140	483	160	2700	72.4	911.9
Al7075-T6	160	570	170	2700	71.7	858.2
Ti2Fe3Al	675	1281	441	4650	113	570
CFRP	85	600	74.4	1600	228	1162.1

Table 5.1: Different material specifics and cabin skin weight.

5.1.3. Results

By using the semi-major axis and semi-minor axis determined in Chapter 3 as input into the numerical model of the method described in subsection 5.1.1, the thickness of the cabin skin was determined. This was obtained for all of the varying cross-sections along the length of the fuselage, revealing the results shown in Figure 5.5.

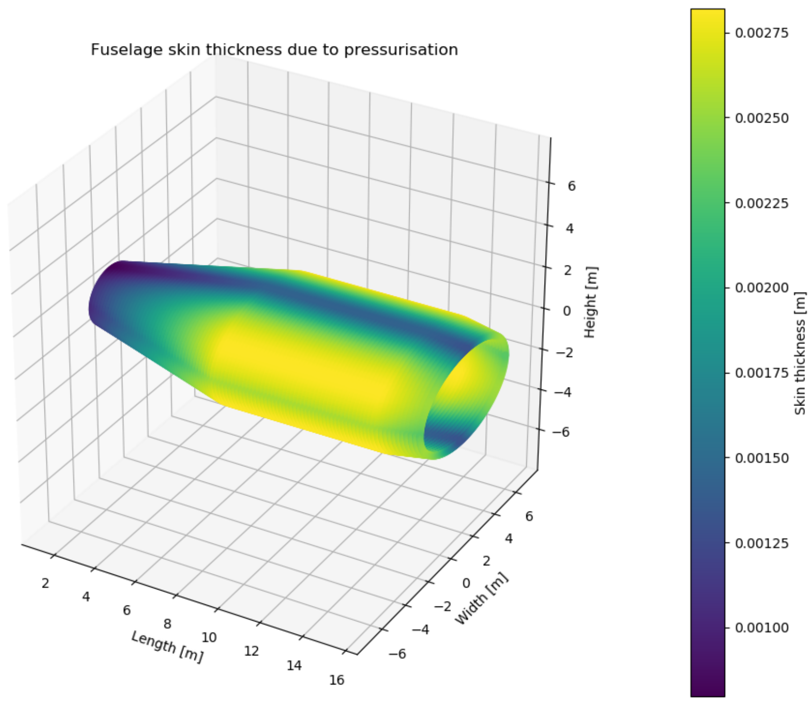

Figure 5.5: Cabin skin thickness

Table 5.2 contains the percentage weight increase for an oval cross section compared with the circular shaped cross section. Comparing the results it is found that the weight increases when $\frac{b}{h}$ increases. In Figure 5.6 the thickness variation for the ellipse and circle are plotted. In this figure it can also be seen that the area covered by the ellipse plot above the circle plot is larger than the area underneath. Using the density of Al2024-T3 the weight of the cabin is estimated to be 912 kg.

Table 5.2: Skin thickness at different cross section positions

	b[m]	h[m]	t_{min} [mm]	t_{max} [mm]	t_{eq} [mm]	%m [%]
Nose	3.8	2.4	0.41	0.69	0.54	14.0
Center	8.4	4.6	0.76	1.5	1.1	18.6
Rear	6.5	4.2	0.72	1.2	0.92	13.3

5.1.4. Verification

The model is verified by comparing the thickness obtained from Equation 5.6 with the analytic solution for a circle[9]

$$t_{skin} = \frac{\Delta PR}{\sigma_{hoop}} \tag{5.12}$$

The results for different cross sections can be found in Table 5.3. Here it can be seen that the relative difference between the numerical and analytic result is in all cases only 0.22 %. This small difference is only due to the discretization of Equation 5.6. Therefore the model can be considered as verified.

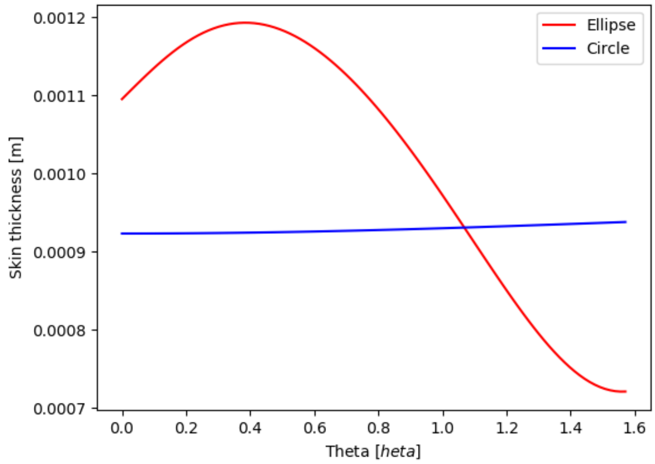

Figure 5.6: Ellipse cross section thickness compared with circle cross section thickness from $\theta = 0$ to $\theta = \frac{\pi}{2}$.

	Numerical thickness [mm]	Analytic thickness [mm]	Rel. difference [%]
Nose	0.537	0.538	0.22
Center	1.10	1.11	0.22
Rear	0.929	0.931	0.22

Table 5.3: Skin thickness comparison

5.1.5. Validation

The skin thickness results are validated by comparing the results with data from reference aircraft. For the B757 the crown skin of the fuselage is 0.89 to 0.94 mm[73]. The fuselage of the B757 is cylindrical, it has a diameter of 3.76 m[2], so the size of the aircraft is similar to that of the nose section of the oval fuselage. As can be seen in Table 5.2 the skin thicknesses of the nose section is lower than that of the B757. This can be because in the design of the skin thickness of the B757 the thickness was dominated by something else than the pressure differential.

5.1.6. Cabin stringers and frames

The loads introduced by the wing, tank, engines, and empenage will be distributed over the stringers using frames. At the locations of load introduction the frames will be designed stiffer. At the locations in between less stiff frames will be placed to distribute loading and maintain cabin skin shape when under pressurization. Unfortunately, due to limited resources a more detailed design of the frames could not be done.

Assumptions

The following assumptions are made for sizing the stringers.

- The stringer shape was not considered, only the Steiner term taken into account in the moment of inertia.
- Only stresses due to moments were considered.
- Moments due to empennage deflections were neglected.
- Thrust forces from the engine neglected.
- Only the loads at the rear of the aircraft were considered for stringer sizing, since the rear is where the most forces act.

[2]URL `https://janes.ihs.com/Janes/Display/jau_a059-jau_` [cited 23 05 2018].

- The cabin rear is analyzed as a cantilever beam at the wing box connection.
- The stringer cross sectional size was assumed constant over the whole cross section and aircraft length.
- The stringer spacing was constant over the cross section.
- No stringers in the floor.

The method

The cabin skin and stringers will both be considered to carry the bending moment introduced by the rear section of the aircraft. After the cabin ends the stringers will carry the remaining loads. First the area moment of inertia needs to be determined. For the ellipse the moment of inertia is

$$I_{yy,fus} = \frac{\pi}{4}(bh^3 - (b - t_{skin_1})(h - t_{skin_2})^3) + A_{skin} d_z^2 \tag{5.13}$$

Where t_{skin_1} is the thickness of the skin at the side t_{skin2} is the thickness of the skin at the top and d_z is the z distance from the centroid of the ellipse to the centroid of the whole cross section. Since the size of the stringers will be much smaller than the size of the cabin only the Steiner terms will be taken

$$I_{yy,str} = \sum_{i=1}^{n} A_{str} d_{z,i}^2 \tag{5.14}$$

Where n is the total amount of stringers, A_{str} is the area of one stringer and $d_{z,i}$ is the z distance from the centroid of the i'th stringer. The floor is also analyzed to carry loads, therefore the moment of inertia of the floor will be taken into account

$$I_{yy,floor} = \frac{1}{12} b_{floor} t_{floor}^3 + A_{floor} d_{z,floor}^2 \tag{5.15}$$

Where b_{floor} is the width of the floor t_{floor} is the floor thickness A_{floor} is the area of the floor and $d_{z,floor}$ is the z distance from the centroid of the floor to the centroid of the total cross section.

The cross section symmetric in the z-axis, so $\overline{y}$ (centroid in the y-direction) is on the z-axis. The cross section is not symmetric in the y-axis, $\overline{z}$ can be found as follow

$$\overline{z} = \frac{\sum A_i z_i}{A_i} \tag{5.16}$$

Where A_i is the area of each section and z_i is the z-distance is the z-positions of their respective centroids. The different moment of inertia can be summed up to get I_{tot}. Using this the stresses due to moments can be determined using

$$\sigma = \frac{M_z y}{I_{tot}} \tag{5.17}$$

Where M is the moment and y is the distance from the centroid to the location where the stress is analyzed. The moments are determined using force and moment equilibrium. First the reaction forces in the section after the pressurized cabin is determined. Figure 5.7 is the free body diagram of the forces at the rear. When applying force equilibrium the following expression for reaction force r_y is found

$$r_y = \frac{W_{ac}}{L} x_{tail} + W_{tank} + W_{emp} + W_{eng} \tag{5.18}$$

In this equation, W_{ac} is the weight of the aircraft, L is the length of the aircraft, x_{tail} is the length of the tail section, W_{emp} is the weight of the empenage and W_{eng} is the weight of the engines. The reaction moment, M_r, is

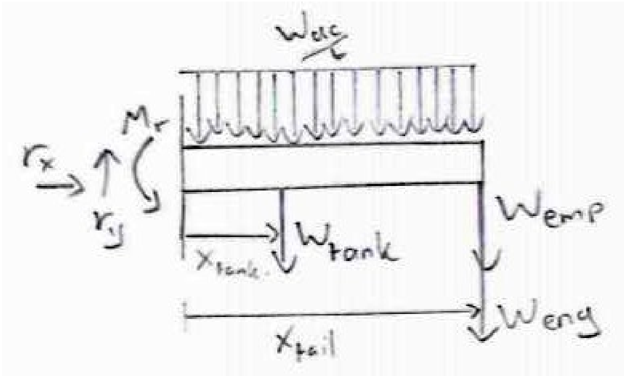

Figure 5.7: Free body diagrams of the rear after cabin section of the aircraft

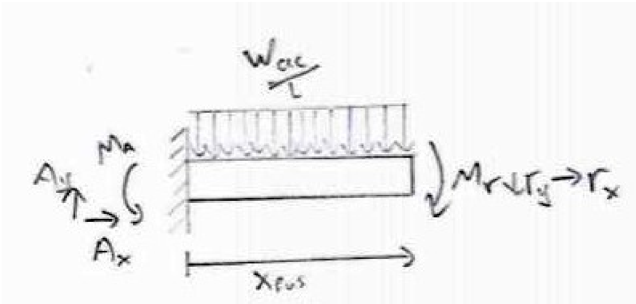

Figure 5.8: Free body diagrams of the rear cabin section of the aircraft

$$M_r = \frac{W_{ac}}{L}\frac{x_{tail}^2}{2} + W_{tank}x_{tank} + (W_{emp} + W_{eng})x_{tail} \tag{5.19}$$

Where x_{tank} is the distance from the cabin rear to the tank. These reactions will be used in the equilibrium of the cabin section of which the FBD is in Figure 5.8. The reaction force, A_y, is

$$A_y = \frac{W_{ac}}{L}x_{fus} + r_y \tag{5.20}$$

Where x_{fus} is the length of the rear part of the cabin. The reaction moment, M_r, is

$$M_A = M_r\frac{W_{ac}}{L}\frac{x_{fus}^2}{2} + r_y x_{fus} \tag{5.21}$$

The sizing of the stringers will be done by first 'guess' a stringer area. If the the computed stress is lower than the allowable stress, the area is reduced. If the computed stress is higher than the allowable the area is increased.

Results

To size the stringers an initial 'guess' area of $0.03m^2$ is taken and a stringer spacing of 0.15 m is used. The limit stress of 170 MPa and density of 2700 kg/m^3 of Al2024-t3 is used as material specifics. For the first iteration the MTOW from the Class I estimation is used which is $W_{ac} = 70.000 \cdot 9.81[N]$. The tank weight is as determined in section 6.2, which is $W_{tank} = 4737 \cdot 9.81[N]$. The engine weight will be elaborated on in section 6.3, the engine weight is $W_{eng} = 5632 \cdot 9.81[N]$. The weight of the empenage is determined using a Class II weight estimation elaborated on in section 5.3. The weight of the empenage is $W_{emp} = 4401 \cdot 9.81[N]$. The size of the stringers as a result of each of these weights can be found in Table 5.4.

	A_{str} $[mm^2]$	n_{str}	$m_{str,tot}$ [kg]
Stringers	844.4	58	2062.9

Table 5.4: String sizing results

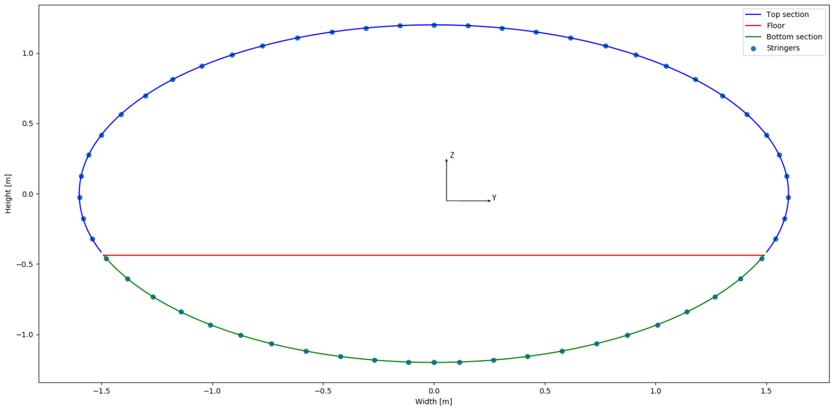

Figure 5.9: Stringer positioning on cross section

Verification

For verification the model was simplified to only one load acting on the end of the fuselage with just one stringer at the top of the fuselage bearing the entire load. This way the model can easily be calculated analytically. In Table 5.5 the comparison between the analytical and numerical solution can be seen. It can be seen that the bending stress in the numerical solution is three times higher than the stress according to the analytical solution. This is most likely due to a discretization error. The error for $\overline{z}$ is relatively small. However, the error increases for the moment of inertia. Especially for the moment of inertia of the stringers the error is particularly large. As can be seen in Equation 5.14, the moment of inertia of the stringers is quadratically dependent of the position of the centroid. Therefore if the error of $\overline{z}$ increases quadratically when determining the moment of inertia using the Steiner terms. Therefore, this model needs to be improved in the future. This does not deem our analysis invalid however, because the stresses were overestimated in Equation 5.1.6, and thus the implementation of this verification should only reduce the thickness and thus also the weight of the stringers.

	$\overline{z}$ [m]	$I_{yy,skin}$ $[m^4]$	$I_{yy,string}$ $[m^4]$	σ [MPa]
Numerical	4.38	0.0803	0.100	13.8
Analytical	4.56	0.0601	0.000096	3.44

Table 5.5: Bending stress and calculation parameters including Steiner terms.

Validation

Validation was done by comparing the stringer size with the stringers of current aircraft with similar loads. This was just by comparing the cross-sectional area of the stringers, so the actual stresses which the validating stringers carry were unknown. The area found for 737 stringer cross-sections was in the order of $10^{-5}[m^2]$, thus validating the area found in Equation 5.1.6 [32].

5.2. Wing box

In this section, the wing box design process is discussed. Firstly, the model is described to generalize the problem that is being solved, together with the assumptions made. Following that, the method and its justifications are explained. After that, the results are given with the layout of the wing box. The results are verified and validated and subsequently a few thoughts about the results are given.

5.2.1. Model

The wing box is split in two sections: outer wing box and inner wing box.
The outer wing box is modelled as a cantilever beam with the length of the wing. The cross-section is approximated by a hollow rectangle, visualized in Figure 5.10. The top and bottom skin have the same thicknesses,

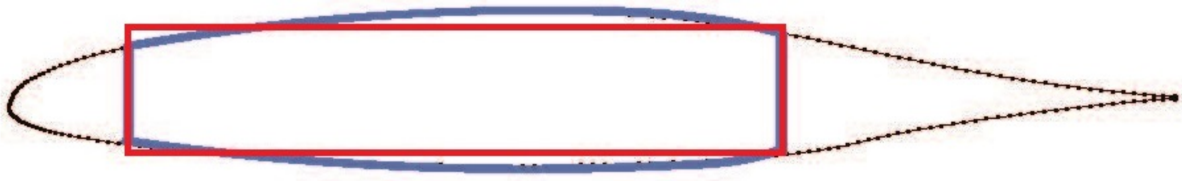

Figure 5.10: Wing box visualization in the airfoil. The wing box (blue), rectangular approximation (red).

similarly the two spars do as well. A taper ratio is implemented, thus the cross-section varies with the span of the wing in width, height and thickness. The dimensions were dictated by the Aerodynamic requirements for the design: wing box height, width, and length, with considerations for structural feasibility.
A distributed load is acting on the beam in y-direction, simulating a lift force. While at the same time a drag distributed load is acting in z-direction with the same shape as the lift but lower in magnitude (proportional to $\frac{L}{D}$). Where L' is the lift distribution, assumed to be perfectly elliptical for ease of calculation. This assumption

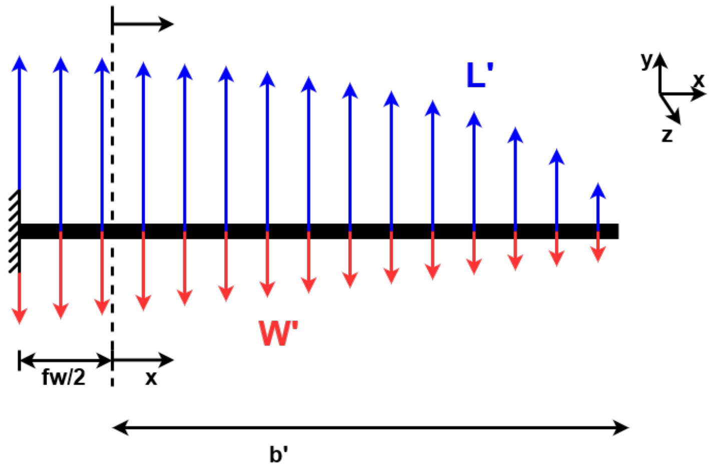

Figure 5.11: Free body diagram of the lift and weight forces acting on the wing.

was deemed sufficiently accurate since BWB designs often optimize so as to approximate elliptical distributions, as is the case with HYDRA [46]. W' is the weight distribution, calculated using the cross-sectional area of the wing box, fw is the fuselage width and b' is the wing box length.
The total distributed load w':

$$w'_y = n_{lim} n_{sf} (L' - W')$$

Where $n_{lim} = 2.5$ is the limit load factor and $n_{sf} = 1.5$ is the structural safety factor.
The same way the drag acts in z-direction with the same distribution as the lift, but lower in magnitude proportionally to the L/D.

$$w'_z = n_{lim} n_{sf} L' \frac{D}{L}$$

In the FBD, b' is the wing box length. The magnitude can be determined by the span and sweep: Figure 5.12.

Where Λ is the sweep angle, b is the aircraft span
Simple trigonometry gives the wing box length:

$$b' = \frac{b - fw}{2 sin(\frac{\pi}{2} - \Lambda)}$$

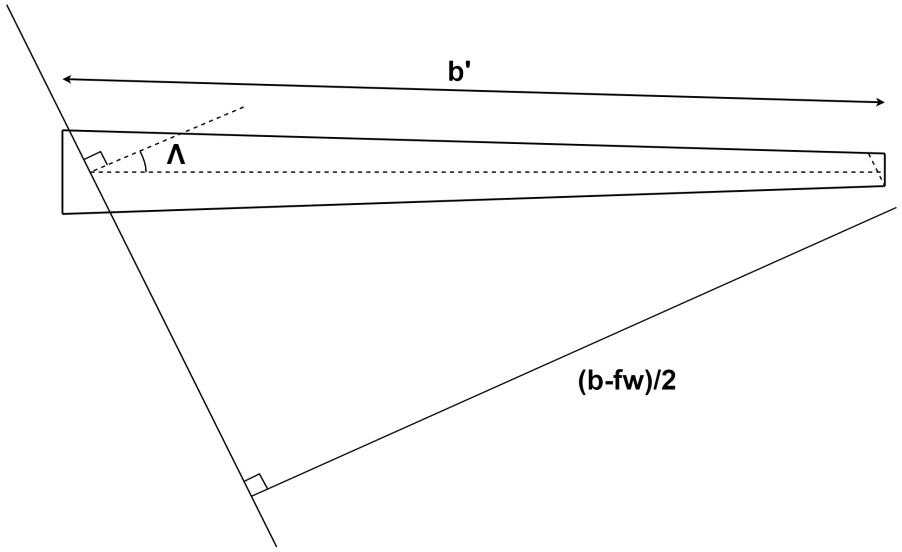

Figure 5.12: Top view of the wing-fuselage connection with sweep angle.

5.2.2. Assumptions

In order to come up with a reasonable design in a limited amount of time, assumptions need to made to simplify the model or the method. The assumptions made for the design of the wing box are as follows:

- The wing box is modelled as a beam. Therefore beam theory applies.
- Torsional loads are neglected.
- Each wall of the wing box is treated as a thin plate.
- Cross-section is treated as symmetric throughout the design. Therefore only top skin will be looked at for stringer placement, and the design shall be copied for the bottom skin.
- The inner wing box is assumed to not carry shear loads but only axial loads due to bending. These loads are the same axial loads as the wing root. Thus the design of the inner wing box is assumed to have the same thickness, rib and stringer spacing as the root section of the outer wing box.
- L' is elliptically distributed load.

Material

The material selected for the wing box is Aluminium 2024 T4. The reason for that is mainly due to the assumptions for thin plate buckling theory, where isotropic material properties provide more accurate results with this method. Since the wing box is loaded in both axial and shear loads. Subsequently, Al 2024 has predictable behaviour under compression (no lamination such as composites). Additionally, Aluminium is a very familiar material to the industry, manufacturing methods are already developed for it, cracks are easy to detect, and its ductility slows crack propagation such that they can be detected far away from failure.
Carbon fibre, for instance, provides very good strength in tension, while Al is good in compression. A combination of both was considered, however the thermal expansion of the two is different and under the temperature ranges expected for the aircraft to operate, will create internal stresses in the structure simply due to the ambient temperature changing.
Aluminium 2024 T4 parameters relevant to this section are shown in Table 5.6.

Parameter [symbol]	Value	Units
E-modulus [E]	79	GPa
Yield strength	270	MPa

Table 5.6: Aluminium 2024 T4 properties.

5.2.3. Method

The method implements the compression buckling of the top skin, bending and shear buckling of the spars. Firstly the stresses are determined with respect to the length of the beam. Following that, thin plate buckling is analyzed to establish a combination of thickness and rib and stringer spacing. The combination, which has the lowest weight is selected, and the calculation is repeated for the next rib spacing step.
The buckling iteration yields thicknesses and stringers, which change the moment of inertia of the cross-section, thus changing the stresses. Therefore, several iterations are run to establish a convergence point, where the stresses dependant on the cross-section geometry ensure that the same cross-section does not buckle.

Stresses

To calculate the internal stresses, the internal shear and moment are calculated. Their diagrams are shown in Figure 5.13a and 5.13b.

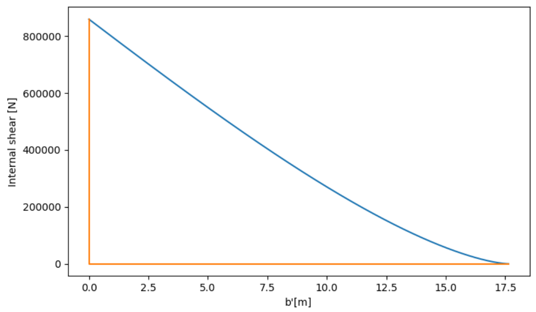

(a) Wing box internal shear.

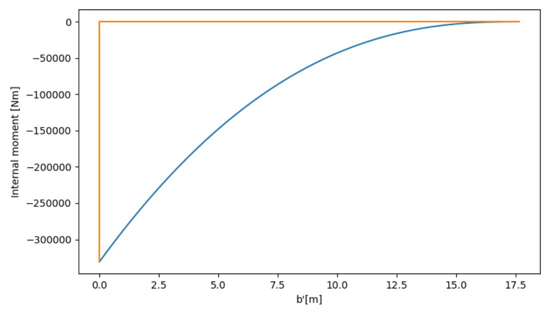

(b) Wing box internal moment

Knowing the cross-section at any span location, the axial stresses and shear flows can be determined.

Axial

The axial loads are a result of the bending moments imposed on the beam due to lift and drag Equation 5.22 and 5.23 respectively.

$$\sigma_{a_{x_1}} = \frac{M_z y}{I_{zz}} \tag{5.22}$$

Where $\sigma_{a_{x_1}}$ is the axial stress due to bending by the lift, M_z is the internal moment in z-direction, y is the cross-section distance from the x neutral axis in y-direction and I_{zz} is the area moment of inertia in z direction around the z neutral axis.

$$\sigma_{a_{x_2}} = \frac{M_z y}{I_{yy}} \tag{5.23}$$

Where $\sigma_{a_{x_2}}$ is the axial stress due to bending by the drag, M_y is the internal moment in y-direction, z is the cross-section distance from the y neutral axis in z-direction and I_{yy} is the area moment of inertia in y-direction around the y neutral axis.

Shear

The shear flow is calculated in a similar fashion as the axial stresses due to bending. Both lift and drag contributions are taken in Equation 5.24 and 5.25 respectively.

$$q_1 = \frac{S_y Q_x}{I_{xx}} \tag{5.24}$$

Where q_1 is the shear flow due to lift, S_y is the internal shear force, Q_x is the first moment of area of the cross-section around the x neutral axis.

$$q_2 = \frac{S_z Q_y}{I_{yy}} \tag{5.25}$$

Where q_2 is the shear flow due to drag, S_z is the internal shear force, Q_y is the first moment of area of the cross-section around the y neutral axis.

Total stresses

In order to estimate whether or not the structure yields under these combined loads, von Mises yield criterion is used. The resulting von Mises stress can be seen in Figure 5.14.

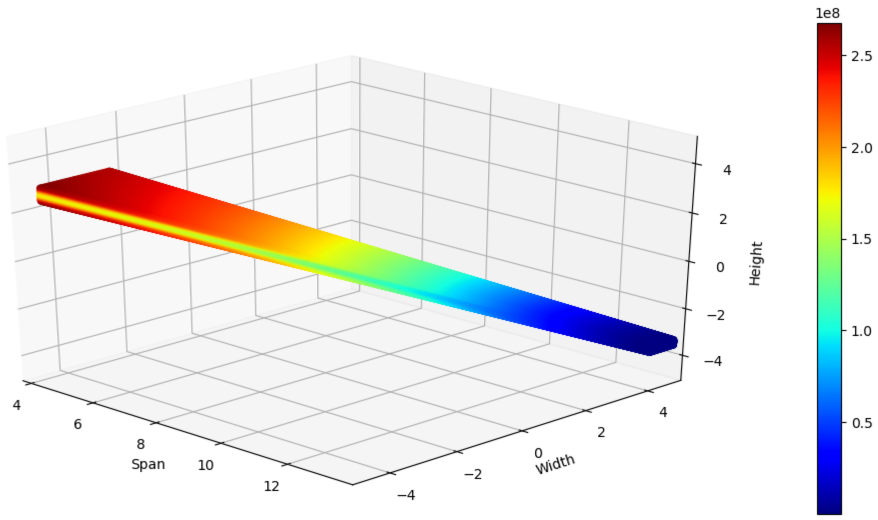

Figure 5.14: Von Mises stresses of the wing box model.

Buckling

Now that the total compressive and shear stresses are calculated, the buckling critical stresses of the skin and spars can be observed. Equation 5.26 is the general buckling equation for thin rectangular plates [43].

$$\sigma_{cr} = \eta K E \left(\frac{t_p late}{b}\right)^2 \tag{5.26}$$

Where σ_{cr} is the critical stress for buckling, η is the plasticity reduction factor, K is the buckling type coefficient, E is the E-modulus of the material, t is the plate thickness and b is the plate width. Equation 5.26 is a general thin plate buckling equation. To represent different buckling modes, the K coefficient changes. For this reason subscripts are introduced for the K coefficient and the critical stress $\sigma_c r$ and the thickness t for each of the buckling modes. The buckling modes and location that shall be observer are:

- Compression buckling of top skin: σ_{cr_c}, K_c, t_c
- Axial stress due to bending buckling of spars: σ_{cr_b}, K_b, t_b
- Shear buckling of spars: σ_{cr_s}, K_s, t_s

At this stage only elastic buckling is observed, for which the plasticity reduction factor is 1 and is not going to be present in this analysis anymore. In order to estimate rib location, number of stringers and thicknesses, the thin plate size needs to be established.

Compression buckling

In Figure 5.15 clamp condition 5 is chosen. By splitting the top skin in plates with the rib and stringers, b of the thin plate is the stringer spacing, while a is the rib spacing.

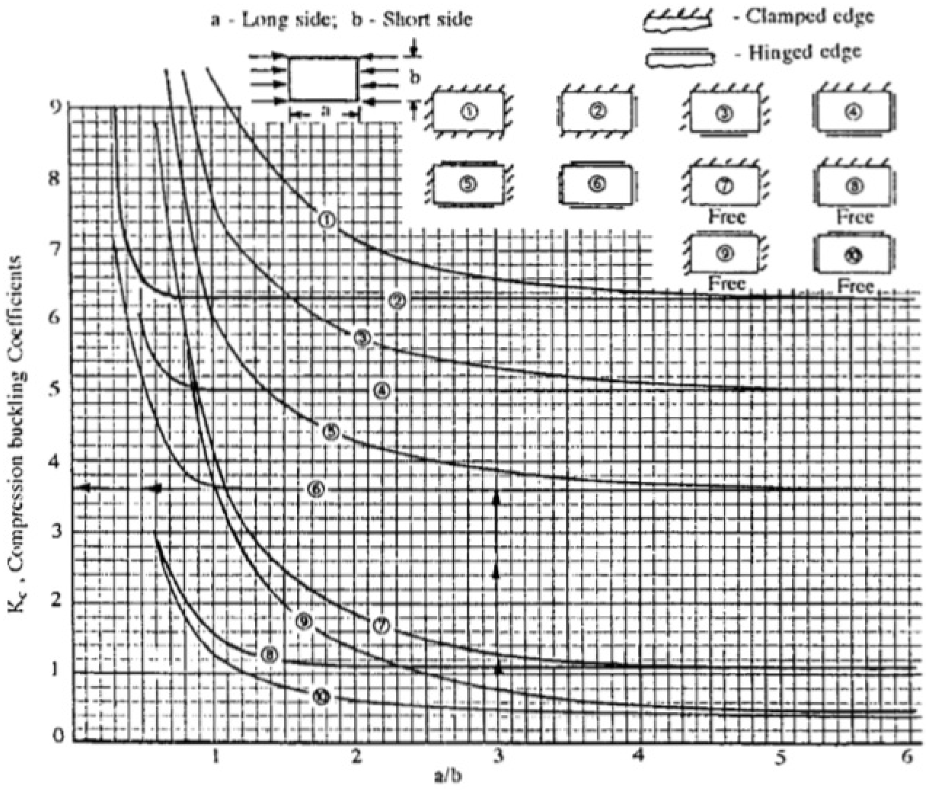

Figure 5.15: Compression buckling coefficient

Bending buckling

This mode of buckling is mainly present in the spars, in this representation b is the spar height at the given location and c is half of it, due to the symmetry assumption. The width is governed by rib placement. Clamping condition 3 is chosen.

Shear buckling

The shear buckling is observed for the spars. In shear, the clamping conditions are slightly different as the shear loads are the same no matter the plate orientation. Thus the coefficient takes only the long and short side Figure 5.17. The clamping condition selected is such that the top and bottom of the spar is clamped (top skin connections) while the sides are clamped (rib present). For the case when the rib spacing is higher than the height of the spar, this results in clamping condition 2. For the case when the rib spacing is lower than the height of the spar, clamping condition 3 holds.

Evaluation

In order to come up with the most optimal number of stringers, rib locations and thicknesses, a combination of all three is ran through a Python script. The code estimates the combinations of stringer spacing, rib spacing and thickness for which no buckling occurs. For all these combinations the least amount of weight is taken. When an optimum is found, the script loops for the next rib step.

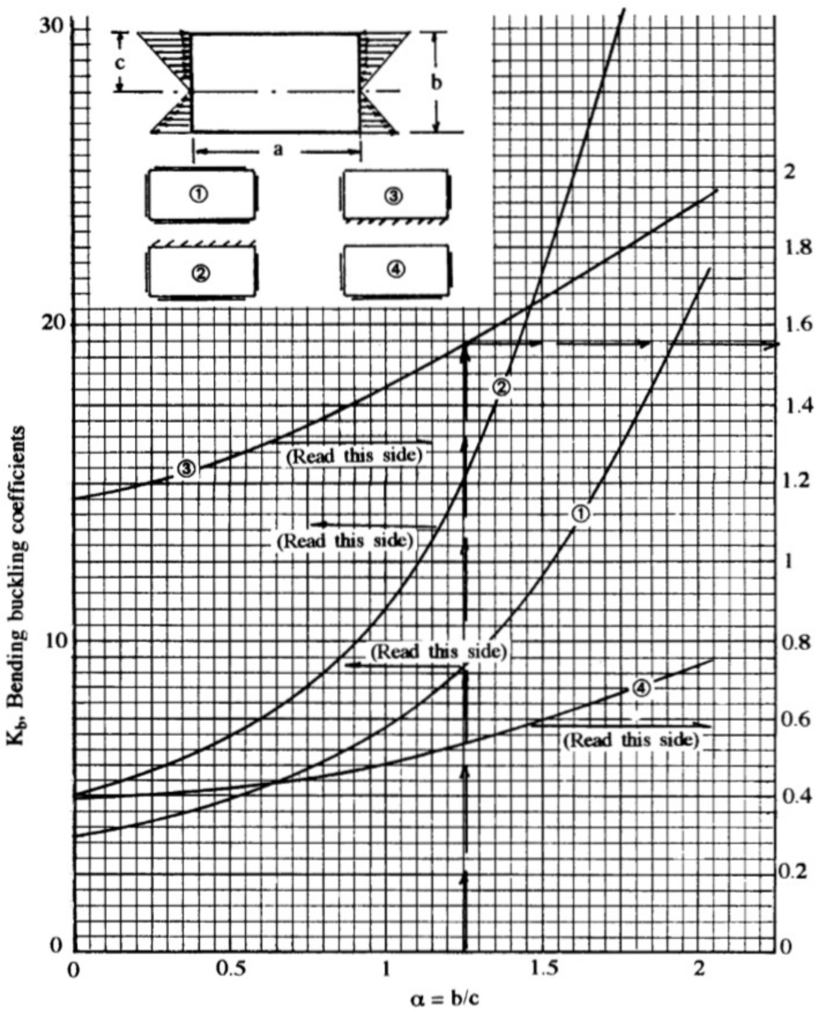

Figure 5.16: Bending buckling coefficient

5.2.4. Results

Several iterations were needed for the results to converge. That is because a high stress, requires more stringers. After adding the required stringers, the stresses are lower than before, so less stringers can prevent buckling. The number of stringers along the length of the wing box can be seen in Figure 5.18a, together with the thicknesses of the skin and spars with respect to the span Figure 5.18b.

Reiterating this design yields a von Mises stress higher than the yield stress of Aluminum. For this reason an extra stringer is added to both top and bottom skins of the wing box. The highest von Mises stress in the wing box with this extra stringer is $\sigma = 269.5MPa$ where Al 2024T4 yields at 270 MPa. The final rib and stringer layout can be seen in Figure 5.19.

The rib spacing becomes lower with the span, which is opposite to how existing aircraft are designed. At the same time, having six stringers distributed along the 2m wide skin panel appears to be low. The model does not include flanges in the estimation. Should flanges be introduced, the rib spacing will most likely increase, due to the lower weight alternative for the spars under buckling loads. By increasing the rib spacing, the required number of stringers for the top skin will increase as well. This requires significant rework of the model, which is stated in as a future suggestion for improvement in Chapter 17.

After the design process had been frozen, an error was found in the value for yield strength of Al 2024 T4. The value used during the design process was 270 MPa, while in reality the value is more around the order of 290 MPa. Additionally, a better for the purposes of the wing box, version of the same alloy- Al 2024 T3 was observed. It has a yield strength of 310 MPa [2]. Unfortunately, the error was spotted after the design was

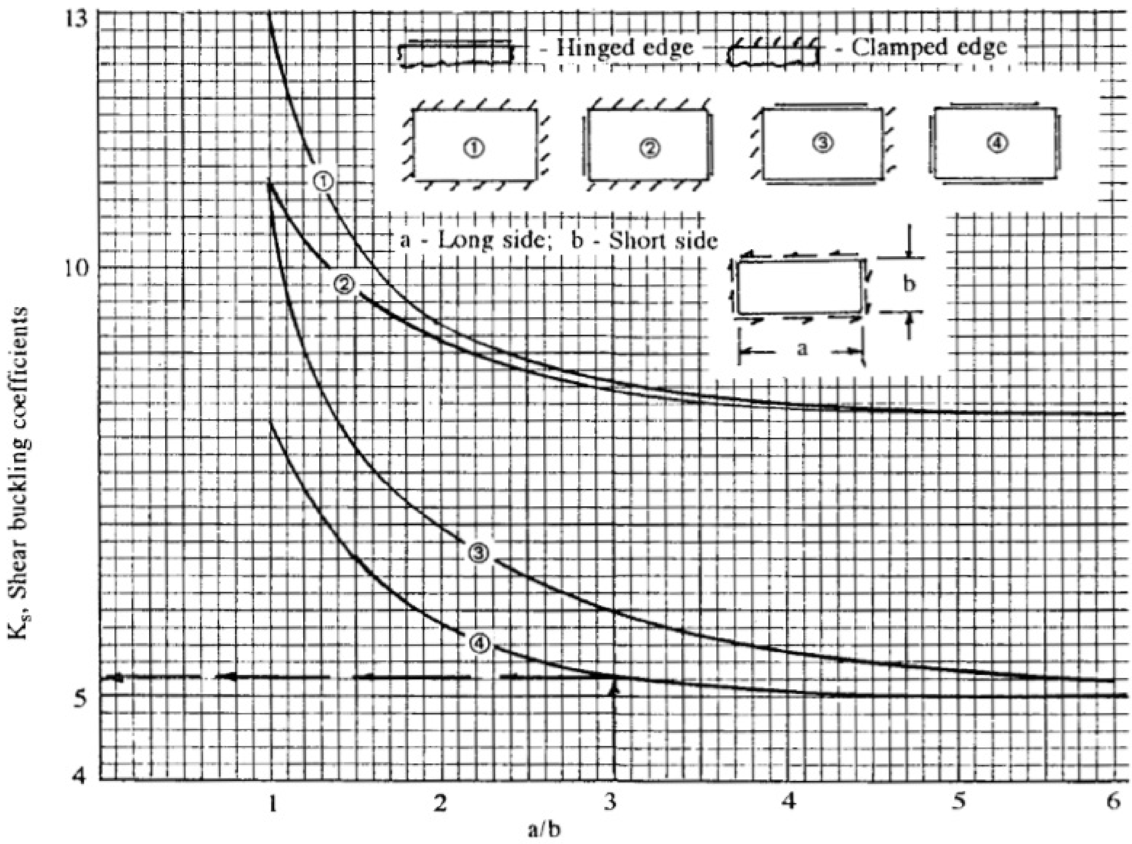

Figure 5.17: Shear buckling coefficient

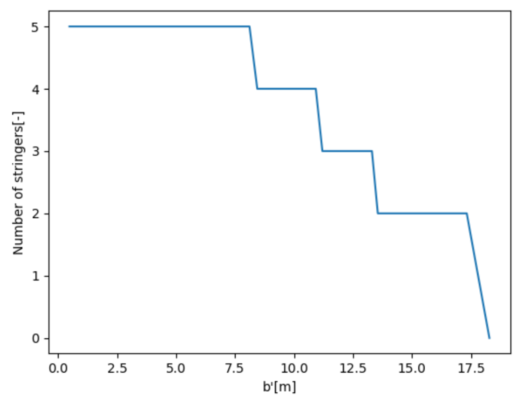

(a) Number of stringers required along the length of the wing box.

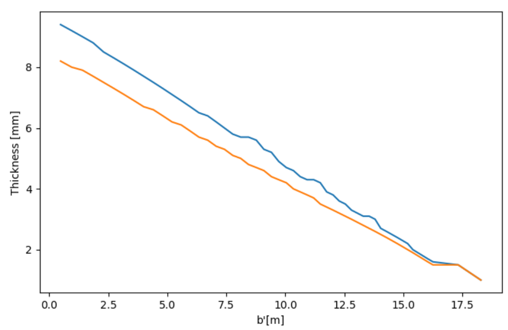

(b) Thickness of top skin (blue) and spars (orange) along the length of the wing box.

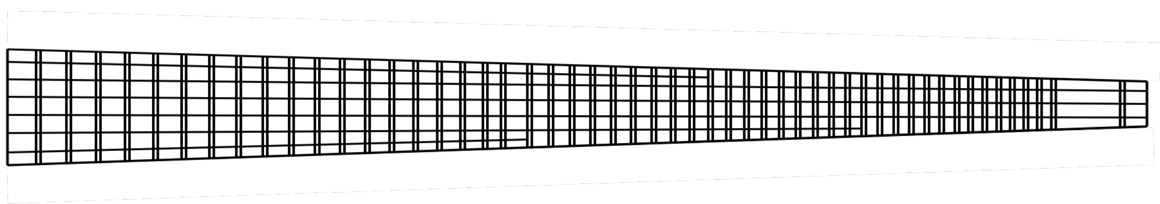

Figure 5.19: Rib and stringer layout for the wing box structure.

frozen, and a change would not be so straightforward. Fortunately, however, the yield strength is a driving factor in the buckling resistance of the wing box skin and spars. Therefore, the current state of the structure design is over engineered and the safety margin is only larger. This margin reduces the effects on one of the assumptions where the torsional loads are neglected.

5.2.5. Verification

In order to validate the method, it is needed to make sure the code calculates the correct values. In order to do that, the critical buckling stress at different key locations is calculated by hand and the result is compared to the stress at that location.

5.2.6. Validation

The best validation method would be to build the model and destructively test it. Unfortunately, due to resources and time this is not possible at this stage. Additionally, there is a lack of resources to perform a FEM test. Another way of validating would also be to observe aircraft with similar wing loading and compare the rib and stringer spacing of that aircraft with the results obtained. Unfortunately, if is not in the scope of this project to perform any of these validation methods.

5.3. Class II Weight Estimation of Airframe

A Class II Weight Estimation must be performed in order to estimate with a higher accuracy the component weights of the aircraft. As stated in section 5.1, the fuselage stringers have been sized and the skin thickness calculated. Also, from section 5.2, the wingbox was sized. These volumes were then be multiplied by the density of the chosen material, giving a weight for both the pressurized fuselage and wingbox, which is more accurate than just an estimation. However, for many of the components of the aircraft, time did not permit for such analyses of the components, and thus weight estimations were performed on the remaining components. These estimations were taken from Howe[29] and Torenbeek[65].

5.3.1. Existing weights

From subsection 5.1.1, the weights of the skin of the pressurized section, and the stringers along the skin were calculated. Thus the pressure membrane given by Howe can be replaced by these weights, and added to the fuselage weight, as seen in Equation 5.3.2.

The outer wing box estimation from Howe can also be partly excluded since the weight of the wing box based on the geometry and stresses of HYDRA was calculated in section 5.2. This can then be implemented in the outer wing weight estimation, as seen in subsection 5.3.2.

5.3.2. Weight estimations from Howe

Outer wing

For the outer wing weight estimation, penalties due to the different components present in the wing, based on Howe's method, were added to the wing box weight calculated in section 5.2. The total weight penalty due to the different additional components is

$$W_{owp} = 0.02\text{MTOW} + K_{flaps}\text{MTOW} + K_{spoilers}\text{MTOW} + K_{aux}\text{MTOW} + K_{wtips}\text{MTOW} \tag{5.27}$$

where $K_{flaps} = 0.003$ is used since single slotted flaps are being implemented. $K_{spoilers} = 0.0015$, used for the spoilers and airbrakes, $K_{aux} = -0.005$ since auxiliary surfaces are likely to be made from carbon fibre, and $K_{wtips} = 0.002$ as currently winglets are not considered in the design. The penalties are then added to the wing box weight to calculate the outer wing weight.

$$W_{ow} = W_{wb} + W_{owp} \tag{5.28}$$

Inner wing

For the inner wing weight estimation, or the inner wing airfoil cowling around the pressurized section, the weights are estimated separately to both the outer wing and the pressurized section. Firstly, the value of D_i is calculated using

$$D_i = 1.52\sqrt{\frac{N\text{MTOW}b^3 r_o e_i sec(\phi_i)sec(\gamma_i)}{\bar{\tau}+1}}\Big((1-y_k)-0.46(1-y_k)^{2.5}\Big)(1+0.53\bar{r})\big(\frac{c_r}{\tau_r}\big)^{0.25}\big(\frac{\rho_i}{\bar{A}}\big)\times 10^{-5} \tag{5.29}$$

With N the ultimate load factor, b the total span, and e_i the ratio of outer wing root chord to the centre line chord. ϕ_i is the inner wing sweep at quarter chord, γ_i the inner wing box sweep at half chord, and $\bar{\tau}$ the ratio of kink to centre line values of the thickness to chord ratios. c_r is the chord at the centre line, and τ_r the thickness to chord ratio of the inner wing. y_k is the ratio of the outer wing span to the total wing span, and ρ_i the density of the chosen material. $\bar{r}$ is the ratio of the inner to outer wing relief factors, r_i to r_o; where r_o, the outer wing relief factor, is defined as

$$r_o = 1-\Big(0.042+0.84Q_o(0.1+2R\times 10^{-5})+\frac{4.55M_v}{\text{MTOW}}\Big)y_k \tag{5.30}$$

where Q_o is the ratio of the fuel carried in the outer wing to total fuel carried (0 for the case of HYDRA), and R the design Range in km. r_i is defined as

$$\begin{aligned} r_i = 1 - 0.12 + 0.114(1-0.63y_k) + 2.27(1-0.63y_k)(Q_o+Q_i)(0.1+2R\times 10^{-5}) \\ +4.55\Big(\frac{M_v}{\text{MTOW}}\Big)+0.76\Big(\frac{M_{PAY}}{\text{MTOW}}\Big)\Big(\frac{3}{2}\Big)+4.55\Big(\frac{W_{mg}Y}{\text{MTOW}}\Big) \end{aligned} \tag{5.31}$$

where $Q_i = 1$, since all of the fuel is carried in the rear of the inner wing. $M_v = 0$ since the current design does not have winglets. M_{PAY} is the mass of the payload carried in the inner wing. c_R is taken equal to c_{k_i}, as the kink station is assumed to be at the root of the outer wing. $Y = \frac{2y}{b}$ where y is the distance of the main landing gear for the centre line.

For the inner wing rib or frame weight estimation, the following is used:

$$M_{r_i} = 4.4S_i e_i\sqrt{c_R\tau_R}(1+0.35\lambda_i)\rho_i\times 10^{-3} \tag{5.32}$$

where S_i is the surface area of the inner wing, and λ_i the taper ratio of the inner wing.

The penalty factors for the inner wing weight estimation are used to estimate the total weight penalty for the inner wing.

$$W_{iwp} = (0.02\text{MTOW}-0.005\text{MTOW})(1-y_k)+0.001\text{MTOW}+0.008\text{MTOW} \tag{5.33}$$

The second coefficient, -0.005, is implemented since auxiliary surfaces will be made of carbon fibre. 0.001 is used because of the two engines mounted on the rear of the inner wing, and 0.008 for the two main landing gears mounted under the inner wing.

Thus the total inner wing weight is estimated to be

$$W_{iw} = D_i + M_{r_i} + W_{iwp} \tag{5.34}$$

Cabin nose

Beginning with the components in the pressurized section, those located towards the nose are estimated first using the following equations.

Firstly, the front pressure bulkhead of the pressurized section is estimated as

$$W_{NPS} = \left(\frac{1.2 d_{1a} S_{ps} \Delta P \rho}{\bar{f}_t}\right) \times 10^{-3} \tag{5.35}$$

where $d_1 a$ is the width of the front of the elliptical pressurized section (where the nose cone is attached). $S_p s$ is the total surface area of the pressurized section, and ΔP the differential pressure between inside and outside of the pressurized section. $\bar{f}_t$ is defined as:

$$\bar{f}_t = 0.8 + 0.05(d_{1a} - 2) \tag{5.36}$$

For the leading edge aerodynamic fairing which extends in front of the nose of the pressurized section, the weight estimation is as follows.

$$W_{LE} = 0.0025 S_{LE} \rho \tag{5.37}$$

Where S_{LE} was assumed equal to S_{ps}, since the difference was considered negligible and truly calculating the area of the section of the inner airfoil in front of the pressurized section was deemed too time consuming.

The windscreen weight was estimated as

$$W_{WS} = 0.75 S_{WS} V_D \Delta P \tag{5.38}$$

where S_{WS} was assumed to be $3[m^2]$. V_D is the design dive speed, taken as 1.25 times the cruise speed.

Crew floor is estimated using

$$W_{CF} = (7 + 1.2B) S_{CF} \tag{5.39}$$

where S_{CF} is the area of the cockpit floor, the floor area in the nose cone.

For doors and miscellaneous items:

$$W_{NMisc} = 0.002\text{MTOW} \tag{5.40}$$

Thus, the weight of the nose of the pressurized section is estimated.

$$W_{Nose} = W_{NCS} + W_{LE} + W_{WS} + W_{CF} + W_{NMisc} \tag{5.41}$$

Remaining pressurized cabin

For the remainder of the pressurized cabin, the majority of the weights were calculated based on the actual stresses which are expected for the aircraft. This was explained in detail in subsection 5.1.1 and subsection 5.1.6, where the skin and stringer weights were determined. section 5.2 not only calculates the weights of the outer wing, but also the torsion box through the fuselage needed to withstand the loads coming from the wing.

That which is missing from this analyses when compared to the weight estimations from Howe is cabin and freight(cargo) floor weights, and penalties for apertures, such as passenger or cargo doors. The cabin floor is taken by multiplying the dimensions of the inner cabin by the thickness of typical aircraft floors. The freight floor is estimated using

$$W_{frf} = 2.6(1 + 0.6 B_{frf}) S_{frf} \rho \cdot 10^{-3} \tag{5.42}$$

where B_{frf} is the width of the freight floor and S_{frf} the area.

The apertures penalty is estimated to be

$$W_{APT} = 60S_{APT} \tag{5.43}$$

where S_{APT} was taken for the 4 type 1 and 4 type 3 doors on the aircraft.

Thus the pressurized section weight is found to be

$$W_{PS} = W_{skin} + W_{str} + W_{tb} + W_{cf} + W_{frf} + W_{APT} \tag{5.44}$$

5.3.3. Weight estimations from Torenbeek

The weight estimation for both the landing gear and empennage is explained in the following section, for which the Torenbeek method was used [65]. Since Torenbeek's method is in imperial units, all inputs and outputs had to be converted, since every other aspect of the design for HYDRA is metric.

Landing gear

The estimation for the main landing gear is

$$W_{mg} = K_{mg}(A_{mg} + B_{mg}\text{MTOW}^{0.75} + C_{mg}\text{MTOW} + D_{mg}\text{MTOW}^{1.5} \tag{5.45}$$

where $A_{mg} = 40$, $B_{mg} = 0.16$, $C_{mg} = 0.019$, $D_{mg} = 1.5 \cdot 10^{-5}$, and $K_{mg} = 1$. All of these coefficients are given in Torenbeek for low wing passenger aircraft [65].

The nose gear is the same, just with a change in coefficients.

$$W_{ng} = K_{ng}(A_{ng} + B_{ng}\text{MTOW}^{0.75} + C_{ng}\text{MTOW} + D_{ng}\text{MTOW}^{1.5} \tag{5.46}$$

where $A_{ng} = 20$, $B_{ng} = 0.1$, $C_{ng} = 0$ $D_{ng} = 2 \cdot 10^{-6}$, and $K_{ng} = 1$.

Empennage

For the vertical tail, the estimation from Torenbeek is

$$W_v = N_v K_v S_v \left(\frac{3.81 S_v^{0.2} V_D}{1000\sqrt{cos(\Lambda_{1/2_V})}} - 0.287 \right) \tag{5.47}$$

where N_v is the number of vertical tails (1), S_v the area, and $\Lambda_{1/2_v}$ the sweep at half chord.

K_v is defined as

$$K_v = 1 + 0.15\left(\frac{S_h * h_h}{S_v * b_v} \right) \tag{5.48}$$

where S_h is the horizontal tail area, and h_h the height of the horizontal tail mount on the vertical tail, which is assumed to be 0.3[m] from the top. b_v is the span of the vertical tail.

For the horizontal tail

$$W_h = N_h K_h S_h \left(\frac{3.81 S_h^{0.2} V_D}{1000\sqrt{cos(\Lambda_{1/2_h})}} - 0.287 \right) \tag{5.49}$$

where $N_h = 1$, $K_h = 1$ since it is not a variable incidence stabilizer, and $\Lambda_{1/2_h}$ the half chord sweep of the horizontal tail.

Total airframe weight

Thus, the total airframe weight is then estimated as it is the sum of all the above components.

$$W_{af} = W_{ow} + W_{iw} + W_{Nose} + W_{PS} + W_{mg} + W_{ng} + W_v + W_h \tag{5.50}$$

Table 5.7: Airframe weight estimation calculations

Subsystem weight	Component weights	Total weight [kg]
W_{ow}	$W_{wb} + W_{owp}$	3520
W_{iw}	$D_i + M_{r_i} + W_{iwp}$	3594
W_{Nose}	$W_{NCS} + W_{LE} + W_{WS} + W_{CF} + W_{NMisc}$	3147
W_{PS}	$W_{skin} + W_{str} + W_{APT} + W_{frf} + W_{cf}$	10397
W_{LG}	$W_{mg} + W_{ng}$	2743
W_{emp}	$W_v + W_h$	4401
W_{AF}	W_{ow}+ W_{iw}+ W_{Nose}+W_{PS}+W_{LG}+ W_{emp}	27802

6

Power and Propulsion

This chapter will discuss the Power and Propulsion systems of HYDRA. First the architecture of the Power and Propulsion is addressed in section 6.1. Followed by tank sizing, and engine sizing in section 6.2 and section 6.3 respectively.

6.1. Architecture

In this chapter the power and propulsion architecture is discussed. The architecture can be seen in Figure 6.1. The cryogenic tank has a total of 4 valves, they are used for fuelling and venting and provide fuel to the APU and open rotors. The fuel is leaving the tank by a pipe close to the bottom of the tank by using pumps and pressure valves to regulate the mass flow. Venting is done by using the pressure difference between the inside and the outside of the tank. The APU is used initially to provide power to all the electrical systems and to provide power needed to start the engine. Once the engines are running, the APU can be shut down as the engines will provide the power needed during flight. The cold hydrogen fuel is passed though a heat exchanger at the exhaust of the engine. This is to heat the fuel and improve the efficiency of the cycle [42].

6.2. Tank sizing

In this section the sizing of the hydrogen tanks is discussed. First in subsection 6.2.1 the thermodynamic model is elaborated on after which the model is verified in subsection 6.2.2. The behaviour of the model in different possible scenarios and the final tank parameters are shown in subsection 6.2.3.

6.2.1. Thermodynamic model

The thermodynamic model is based on earlier research done on cryogenic storage systems [35]. The model is based on self pressurization of cryogenic tanks due to heat flow into the tank. The model is obtained by applying he first law of thermodynamics and conservation of mass. This gives the homogeneous equation for a pressure change.

$$\frac{dP}{dt} = \frac{\phi_E}{V}\left\{Q + W + \dot{m}_i\left[h_i - h - \rho\left(\frac{\partial h}{\partial \rho}\right)_P\right] - \dot{m}_o\left[h_o - h - \rho\left(\frac{\partial h}{\partial \rho}\right)_P\right] + \rho^2\left(\frac{\partial h}{\partial \rho}\right)_P \frac{dV}{dt}\right\} \tag{6.1}$$

Where the energy derivative $\phi - E$ is defined as

$$\phi_E = \frac{1}{\rho\left(\frac{\partial u}{\partial P}_\rho\right)} \tag{6.2}$$

For self pressurization of the tank without mass flow in or out of the tank and a constant volume, the equation can be simplified to the following

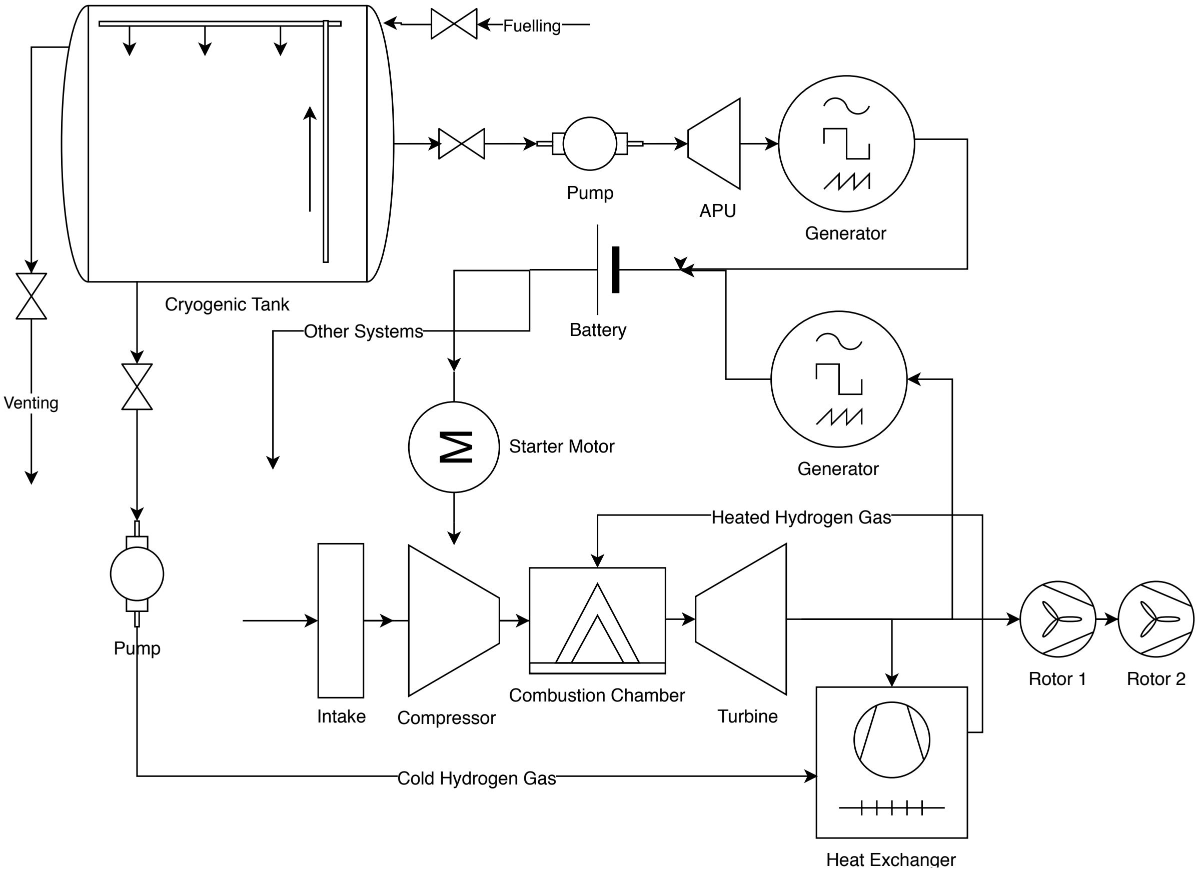

Figure 6.1: Power and Propulsion Architecture

$$\left(\frac{dP}{dt}\right) = \frac{\phi_E Q}{V} \tag{6.3}$$

In the case of having a mass $\dot{m}$ leaving the tank the equation takes the following shape

$$\frac{\phi_E}{V}\left[Q_{in} - \dot{m}_{hydrogen} h_{fg}(x+\rho^*)\right] \tag{6.4}$$

where x is the vapor quality of fluid leaving the tank, $\rho^* = \rho_g/(\rho_f - \rho_g)$, $h_f g$ the difference in the enthalpy between the fluid and gas.

The assumptions made by the model are listed below

- The hydrogen is always in liquid-vapor equilibrium
- Uniform temperature in the tank
- Constant volume in the tank
- Hydrogen leaving the tank is fully liquid and has a vapor quality $x = 0$
- The hydrogen leaving the tank due to venting has a vapor quality $x = 1$

The thermodynamic model requires the properties of hydrogen for every time step. The properties are collected from the NIST [1] database for a range of pressures and temperatures. This data is incorporated in the Python code such that the properties can be called when needed.

[1] URL `https://webbook.nist.gov/cgi/cbook.cgi?ID=1333-74-0` [cited 22 June 2018]

Figure 6.2 shows the $P-v$ diagram for hydrogen with constant temperature lines. The figure can be split into multiple domains. The left domain, left of the liquid line, is where hydrogen is in a fully liquid state. The middle domain, between the liquid and vapor line, is where hydrogen is in liquid-vapor equilibrium. finally the right domain, right of the vapor line, is where hydrogen is in a fully vapor state. The hydrogen will always be in the center domain because of the assumptions made with the model. This assumption is seen valid as in cruise conditions the hydrogen is in a steady state with constant volume, massflow and temperature.

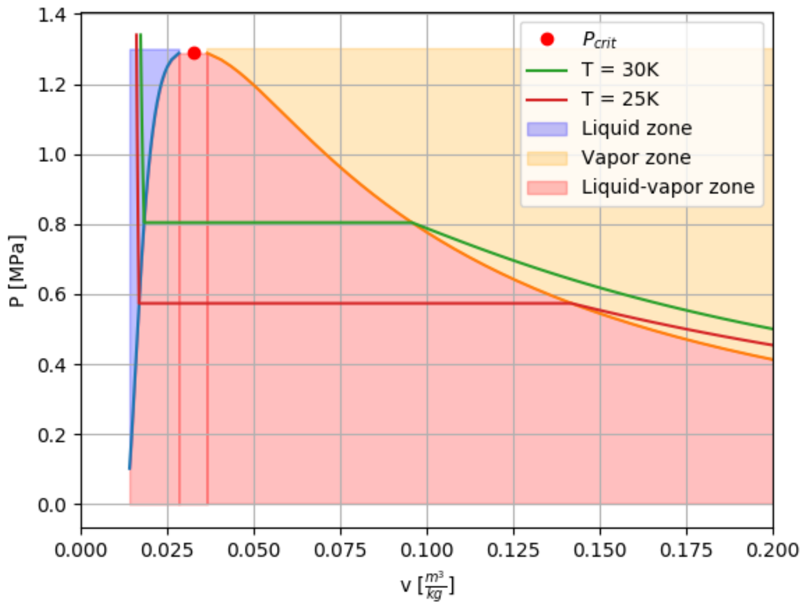

Figure 6.2: P - v diagram

Since the tanks are at cryogenic conditions the heat flow into the tanks should be kept under control. As the increased energy in the system increases the pressure and therefore an increase in temperature as can be seen from Figure 6.2. The pressure in the tank should be kept under a certain level in order maintain structural integrity of the tank. A heat transfer model is created to determine the heatflow in the tanks. The following assumptions were made in the creation of the heat transfer model:

- On the outside surface of each tanks only natural convection and radiation is present.
- The only form of heat transfer on the inner surface is natural convection and no radiation.
- The geometry is simplified as a box, with rectangular end surfaces and trapezoidal side plates.
- Heat transfer through pipes and tank connections are neglected.
- Assume outside temperature to be be at ambient temperature.
- Only conduction through the insulation.

In order to reduce the heat flow in the tank, insulation is applied. Figure 6.3 shows the different layers on the tank. The inner layer is an aluminium tank liner, the aluminium alloy is AA2219. This properties of this alloy are beneficial at the cryogenic temperatures. Furthermore due to the small size of the hydrogen molecules, the hydrogen tends to escape from the pressure vessel, but aluminium in general performs well at containing hydrogen molecules [74]. After the aluminium inner liner the insulation begins. The first layer of insulation is a foam layer and is the most effective layer in the insulation. After the foam layer a layer of MAAMF is applied this is a layer consisting out of Mylar-Aluminiumfoil-Aluminiumfoil-Mylar-Fiber. This provides the vapor barrier and keeps hydrogen from escaping further. The different layers of the MAAMF are shown in Figure 6.3, the fiber is Dacron fiber. Then another layer of foam is applied which is still effective but less effective than the first layer of foam. After the second layer of foam a second layer of MAAMF is applied. Which is then covered with a glass fiber fairing. This configuration was based on the configuration described in [74]. The thickness of the aluminium inner liner and the fairing, it was assumed that these two layers are load carrying. The inner liner as main component and the fiber glass fairing as a secondary structure if the aluminium might fail. Due to the elliptical shape of the tank, the thickness of the aluminium inner liner and the glass fiber fairing were determined using the method described in subsection 5.1.1. The thicknesses of the layers are shown in Table 6.3. In some thermal vessels a vacuum is used to eliminate heat transfer. Due to the vacuum the only means of heat transfer is radiation, thus conduction and convection are eliminated. The vacuum was considered, but was deemed structural unfeasible because the inner tank would have been suspended in the outer layer.

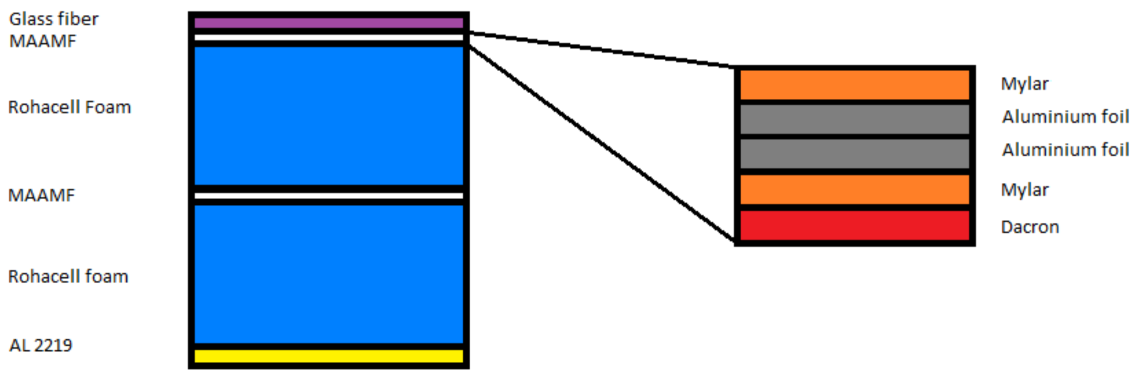

Figure 6.3: The different layers of insulation shown, with a close up on the MAAMF barrier.

The heat transfer model is set up just like an electric circuit where the insulation is equal to the resistance. Each layer has its own thermal resistance and it depends on the configuration of the insulation or heat transfer methods present they can be added as resistances in series or parallel. The method for the determination of the thermal resistances was as follows. After the configuration of the insulation was known the resistance for each of the layers can be determined. Since the tank is assumed to be a box, the equations for flat plates will be used in the calculations for the heat flow. The geometry of the tank assumed as a box is shown in Figure 6.4. All of the formulas describing the heat transfer model were obtained from [31] and [39].

$$R_{cond} = \frac{L}{k \cdot A_{tank}} \tag{6.5}$$

Equation 6.5 was used for determining the thermal resistance of the flat plates, in which k represents the thermal conductivity coefficient of the material. In order to optimize the insulation the value of k should be small. The foam that is used has the lowest value for k of all the materials used and therefore the thickness of the foam layers will be maximized to provide sufficient insulation. In order to determine the total resistance of the insulation a summation of each layer should be done, because the layers are placed in series and therefore can be added simply, which is similar to the electric circuit with resistances in series.

After determining the resistance of the insulation the thermal resistance for the internal natural convection was next to be determined. Due to the simplifications applied to the geometry the calculations could be performed with more ease, since for the actual elliptical shape no empirical relations exist.

$$R_{conv} = \frac{1}{h_c \cdot A_{tank}} \tag{6.6}$$

Equation 6.6 was used to determine the convective resistance. In which A is the area and h is the convective coefficient. In order to determine the convective coefficient, which is a function of the Nusselt number and the thermal conductivity coefficient k of the fluid.

$$h_c = \frac{Nu \cdot k}{L} \tag{6.7}$$

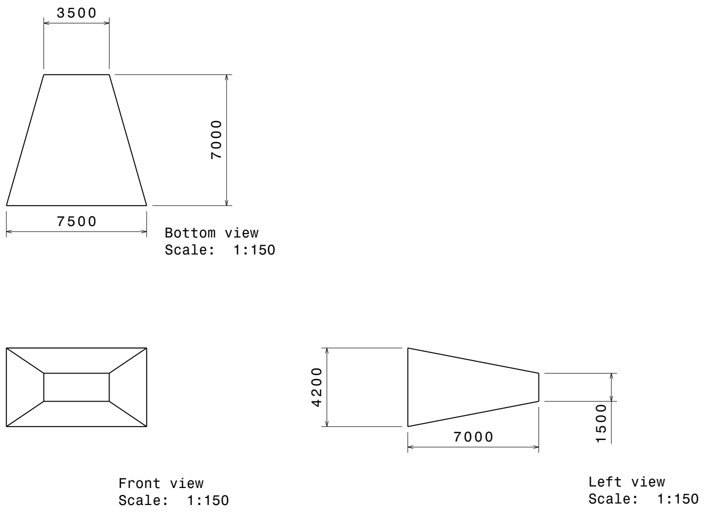

Figure 6.4: The geometry of tank for the assumed box shaped tank

Equation 6.7 shows the relation used to determine the convective coefficient. For the Nusselt number different empirical relations exist for different orientations of the flat plates.

$$Nu = \left(0.825 + \frac{0.387 \cdot Ra^{1/6}}{(1 + (\frac{0.492}{pr})^{9/16})^{8/27}}\right)^2 \tag{6.8}$$

$$Nu = 0.54 \cdot Ra^{1/4} Ra < 1 \cdot 10^7 \tag{6.9}$$

$$Nu = 0.15 \cdot Ra^{1/3} Ra > 1 \cdot 10^7 \tag{6.10}$$

$$Nu = 0.27 \cdot Ra^{1/4} \tag{6.11}$$

Equation 6.8 is used to determine the Nusselt number for a vertical flat plate, in the simplified box design there are four of these. Equation 6.9 and Equation 6.10 show the equations used for the bottom plates, dependent on the magnitude of the Rayleigh number, Ra, Equation 6.9 or Equation 6.10 is used. Equation 6.11 was used for the Nusselt number for the horizontal top plate in the box.

From the previous equations it is seen that the Nusselt number is a function of the Rayleigh number and the Prandtl number as is the case in Equation 6.8. In order to determine the Rayleigh number the following equation is used:

$$Ra = Gr \cdot Pr = \frac{g \cdot \beta \cdot (T_{sur} - T_{\infty}) \cdot L^3}{\mu^2} \cdot Pr \tag{6.12}$$

In Equation 6.12 it can be seen that the Rayleigh number is a function of the Prandtl and the Grashof number. The grashof number is given by the folowing equation.

$$Gr = \frac{g \cdot \beta \cdot (T_{sur} - T_{\infty}) \cdot L^3}{\mu^2} \tag{6.13}$$

In Equation 6.13 it can be seen that it is the left hand part in Equation 6.12 before the multiplication with the Prandtl number. Furthermore the β in the equation is one over the average temperature of the wall and the fluid and is given by:

$$\beta = \frac{1}{\frac{T_{sur} + T_{\infty}}{2}} \tag{6.14}$$

The Prandtl number is given by:

$$Pr = \frac{c_p \cdot \mu}{k} \tag{6.15}$$

Equation 6.15 shows that the Prandtl number is the ratio of the c_p and viscosity over the thermal conductivity of the fluid. For the internal convection the properties were taken from the NIST properties.

For the external surface both radiation and natural convection were considered as means of heat transfer. The same equations as described in Equation 6.6 until Equation 6.15 were used for the external convection. Only the properties of air were used for the calculations [2].

Next to convection, radiation is the other form of heat transfer on the external part of each tank. To determine the thermal resistance for the radiation, an coating was selected to reduce the effect of the radiation. The radiation coefficient is given by the following formula:

$$h_r = \epsilon \cdot \sigma \cdot (T_{sur} + T_\infty) \cdot (T_{sur}^2 + T_\infty^2) \tag{6.16}$$

In Equation 6.16 ϵ represents the emissivity of the material that is used as coating. σ represents the Stefan - Boltzmann constant. To go from the radiation coefficient to the thermal resistance Equation 6.17 is used to determine the resistance.

$$R_{ext_{rad}} = \frac{1}{h_r \cdot A_{tank}} \tag{6.17}$$

After knowing all the different resistances they need to be added to get the total thermal resistance of the system. For the internal convection and the conduction is simple addition because no parallel factors are present. For the external part where both natural convection and radiation occurs the total resistance for the external part should be calculated first and then the result can be added to the other parts in series.

$$\frac{1}{R_{ext_{tot}}} = \frac{1}{R_{ext_{conv}}} + \frac{1}{R_{ext_{rad}}} \tag{6.18}$$

Equation 6.18 shows the total external thermal resistance. The same method is used as in the electrical circuits with parallel resistances.

$$R_{tot} = \sum_{i=1}^{n} R_i \tag{6.19}$$

The total thermal resistance is taken by summing all the resistances from each layer as shown inEquation 6.19. After the total thermal resistance is known the heat flow into the system can be determined.

$$Q = \frac{\Delta T}{R_{tot}} \tag{6.20}$$

The heat flow is determined by Equation 6.20. The temperature difference is the difference between the temperature of the hydrogen and the temperature of the atmosphere around the tank. In figure Figure 6.5 the temperature of every layer is shown. The colors for every section, are the same colors as in Figure 6.3, to differentiate between the different layers.

Insulation optimization

When optimizing for constant pressure the following condition holds

$$Q_{in} = Q_{out} \tag{6.21}$$

[2] URL `https://www.engineeringtoolbox.com/dry-air-properties-d_973.html` [cited 21 06 2018].

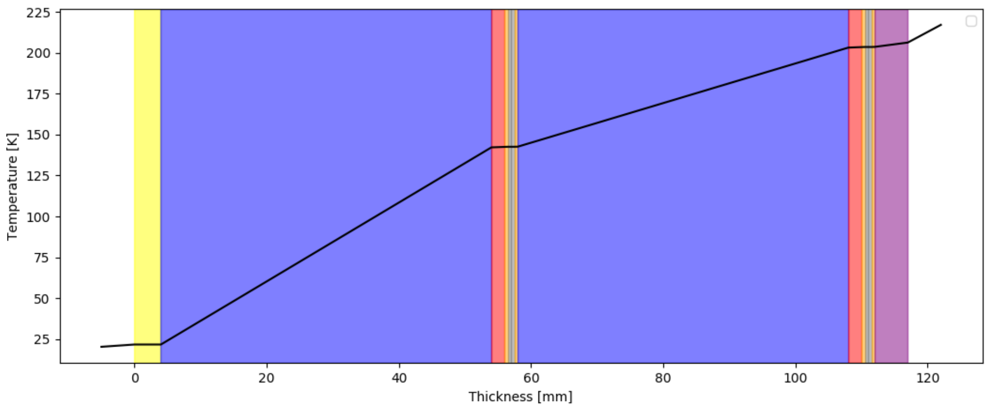

Figure 6.5: Temperature throughout the tank layers

where Q_{in} depends on the level of insulation of the tank and can easily be changed by varying the thickness of the foam layers. Q_{out} depends on the state of the hydrogen and the mass flow out of the tank. This means that Q_{out} changes depending on Q_{in} and that calculating the optimum insulation thickness will require many simulations in order to converge. Because of this, the insulation thickness will be estimated based on the Q_{out} at the initial step to save time as shown in Equation 6.22. This will give a first order estimate of the thickness that can then later be optimized manually.

$$Q_{out_{estimate}} = \dot{m}_{hydrogen} h_{fg} \frac{\rho^V}{\rho^L - \rho^V} P_{max} \tag{6.22}$$

The first order estimate for insulation thickness required can be calculated by using the heat flow calculation. This is done by calculating the heat flow entering the tank for different insulation thickness at the initial state of the hydrogen tanks.

6.2.2. Model verification

Results for the model are presented in [35] and can be used to verify a correct implementation of the model. The verification is split into multiple parts or units. The first unit is the verification of the hydrogen properties, second the energy derivative followed the verification of self pressurization of a tank. Finally the heat flow calculations are validated.

The data provided from NIST is assumed to be valid but the implementation of this data in Python has to still be verified. This is done using CoolProp,a thermophysical property database. CoolProp offers similar functionality compared to REFPROP, a software developed by NIST, but is open source and free to use. The results of both methods can be seen in Table 6.1. The values for both implementations are similar which verifies the correct implementation of the NIST data.

Table 6.1: Verification of data sets

	Own implementation using NIST data				CoolProp			
$T[K]$	v^L	v^V	h^L	h^V	v^L	v^V	h^L	h^V
20.28	70.95	1.30	-900	448196	70.95	1.30	-891	448223
25	64.70	3.89	54158	4463355	64.70	3.89	54161	463370
33	38.07	24.65	255732	343343	38.08	24.64	255694	343404

The energy derivative can be verified by results as presented in [35] by using the same parameters. A comparison between the energy derivatives can be seen in Figure 6.6. Both the energy derivatives behave in a similar manner with less than 2% difference. This verifies a correct implementation of the energy derivative.

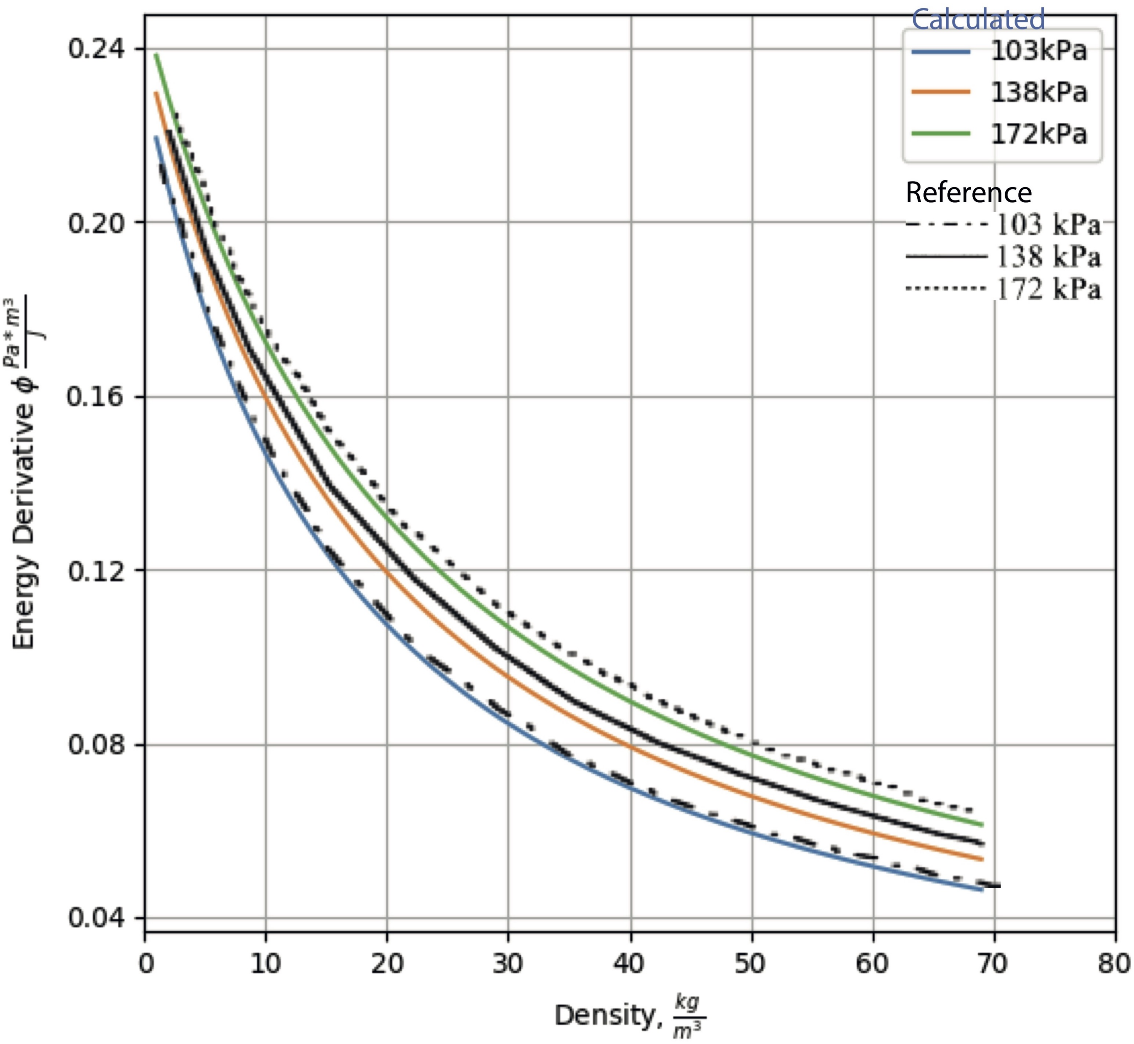

Figure 6.6: Comparison between energy derivatives

The self pressurization can be verified by results as presented in [35] by using the same initial parameters. The results form the two implementations can be seen in Figure 6.7 It can be seen that results of both implementations are very similar and show a similar behaviour. Some discrepancies can be seen however only over longer time frames. This can be explained by the propagation of small errors throughout the program. These small errors can be caused by small differences in the hydrogen properties and energy derivative.

For the heat transfer model the verification of the model was done by checking the surface temperatures of each layer, by going from the cryogenic section to the ambient section and taking the initial temperature of the hydrogen or by calculating from the ambient section to the cryogenic section and taking the ambient temperature as the initial temperatures. Both initial temperatures together form the ΔT used in the calculation of the heat flow into the tanks. By multiplying the resistance of each layer with the total heat flow of the system, the temperature difference of each layer can be calculated. This difference should be added with the initial temperature to form the new initial temperature of the next layers. What should happen is that the temperature increases until the ambient if going from the hydrogen to the ambient. Then the second check is by going the other way around. What should happen in that case, is that the temperature decreases in every layer until it reaches the temperature of the hydrogen when arriving in the hydrogen layer. When doing this calculation the result does add up, therefore shows that the model works as intended. The same procedure was taken for verification of the insulation itself since it the only means of heat transfer is caused by conduction. The results showed the same trend as described for the whole model, therefore showing that the conduction model works as it was intended to work.

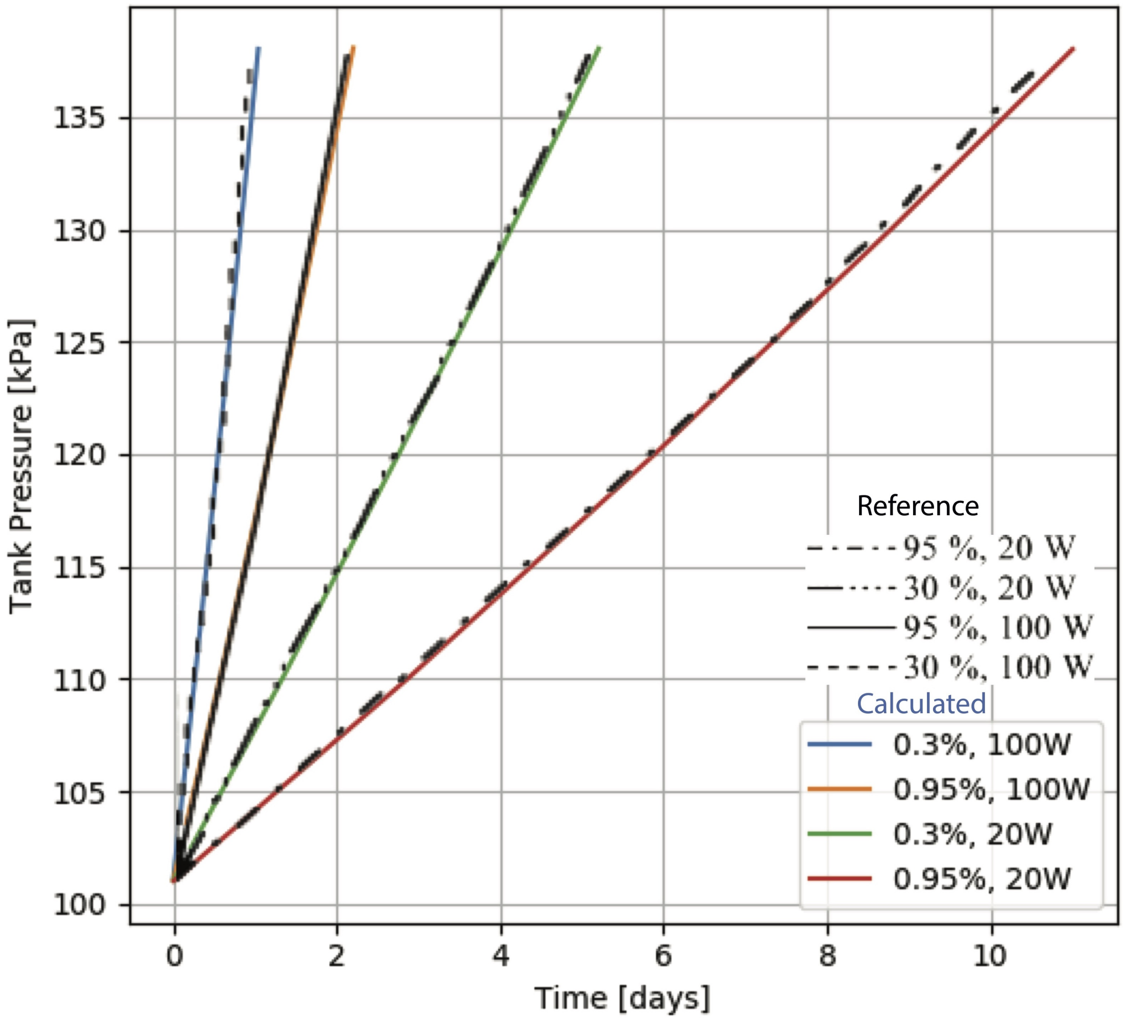

Figure 6.7: Comparison between self pressurization, $V = 52m^2$

6.2.3. Results

In this section the results of the thermodynamic model are presented. All input parameters are specified in Table 6.2. With the input parameters the insulation optimization can be used to get an estimate of the insulation thickness required. This allows for the calculation for the initial tank volume and hydrogen mass together with the total tank thickness. The final tank parameters are shown in Table 6.3. The actual tank is shown in Figure 6.8 with the corresponding dimensions. A more detail plot of the behavior of the tank in cruise in shown in Figure 6.9.

Tank weight

The weight of the tank is estimated using the same method as described in subsection 5.1.6. The tank dimensions from Table 6.2 are used to calculate the thickness of the aluminum inner liner and the outer glass fiber fairing. Then by using the thickness, area and density, the mass of each layer is calculated. The total mass of the tank can be found in Table 6.3

Self pressurization

Self pressurization occurs when there is no mass leaving the tanks. Self pressurization happens when the aircraft is standing on the ground and it is therefore important that the tank can withstand self pressurization for some period of time. In this scenario the outside temperature from Table 6.2 is changed to 40 degrees

Table 6.2: Input parameters

Parameter	Value	Unit
$T_{hydrogen}$	20.28	K
$T_{outside}$	218.15	K
β_{fill}	0.95	$[-]$
P_{max}	4	bar
r_{vent}	0.05	m^2
$\dot{m}$	0.0147	$\frac{kg}{s}$
k_{al2219}	120	W/mK
$k_{glassfiber}$	0.04	W/mK
k_{mylar}	0.155	W/mK
k_{alfoil}	237	W/mK
k_{dacron}	0.1368	W/mK
t_{dacron}	0.002	m
t_{mylar}	0.0005	m
t_{alfoil}	0.0005	m

Table 6.3: Final parameters

Parameter	Value	Unit
V	75.3	m^3
$m_{hydrogen}$	4731	kg
m_{tank}	4737	kg
t_{foam1}	0.063	m
t_{foam2}	0.063	m
$t_{alu_{liner}}$	0.00335	m
$t_{glass\ fiber}$	0.003	m
t_{total}	0.1405	m

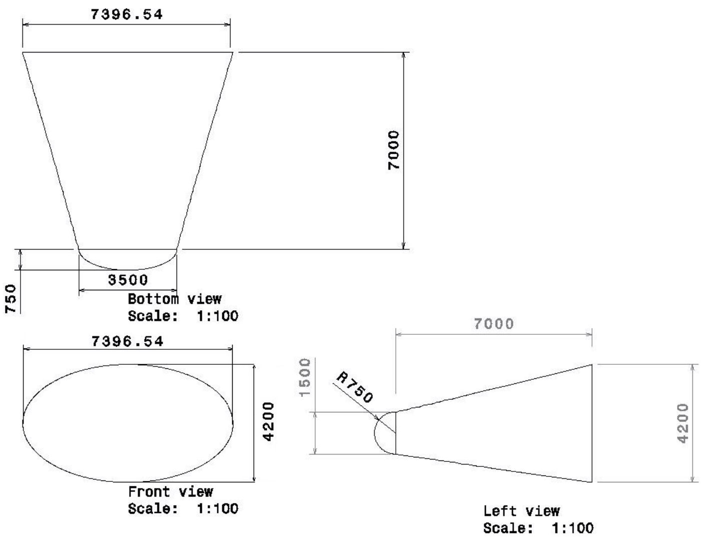

Figure 6.8: The dimensions of the tank

Celsius to emulate a hot airport. The results for a 1 hour period can be seen in Figure 6.10. It can be seen that the pressure increases to over 1.5 bar in one hour.

Venting

Venting is used to deliberately lower the pressure in the tank and is also used as a safety feature to prevent the tank from over pressurizing. Venting is triggered by passing a certain pressure level and will stop after a certain predefined pressure level. The pressure that triggers the venting process should be below the maximum pressure of the tank. In Figure 6.10, the pressure increases rather rapidly. Figure 6.11 shows the same tank in the same scenario but now with venting enabled. It can be seen that the pressure increases to the maximum design pressure within 4 hours at the ground at 40 degrees Celsius.

Heating

Heating can be used to raise the temperature and therefore also the pressure in the tank. This can be usefull when the pressure inside the tank is lower than the pressure outside. This scenario can occur at the end of

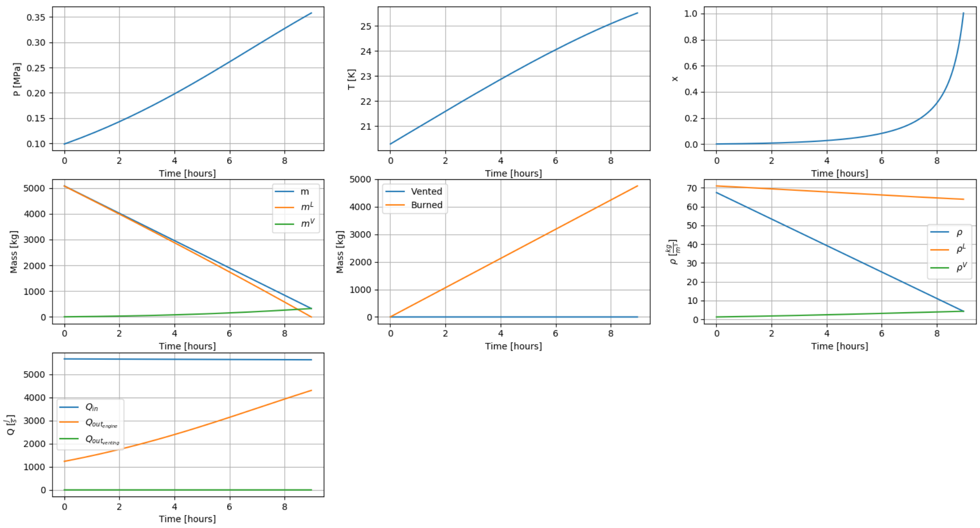

Figure 6.9: Behavior of tank in cruise

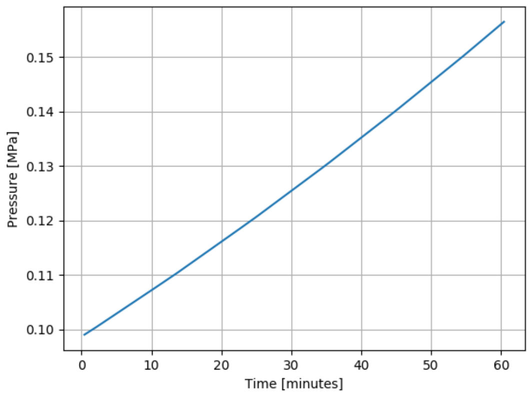

Figure 6.10: Self pressurization

cruise then the aircraft is descending to the ground. In Figure 6.12 a Q_{in} of $100kW$ is set. This allows the tank to increase the pressure from outside cruise pressure to sea level pressure in 15 minutes. The trend is exponential up until P_{crit} of hydrogen at which the assumption of equilibrium is no longer valid. In practice this point will not be reached as the tank is design to vent far before this point. The reason that this method is investigated is because pressurization with use of air is not a possibility as it will mix with the hydrogen and produce a flammable mixture.

Fuelling

Fuelling a closed tank will increase the pressure and therefore also the temperature. To combat this venting can be used. This mean that fuelling the tanks will lead to a loss of hydrogen due to venting. Fuelling with venting can be seen in Figure 6.13.

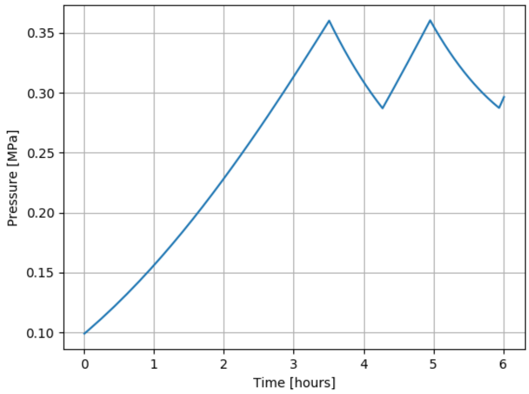

Figure 6.11: Venting

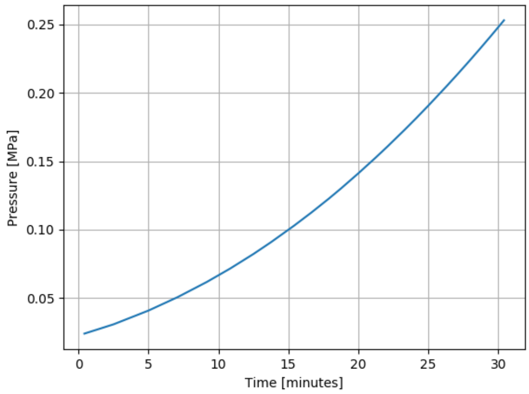

Figure 6.12: Heating at $Q = 100000W$

6.2.4. Model sensitivity analysis

A sensitivity analysis of the tank design is crucial in determining how the model reacts to changes in the design. The design of the tank is very much dependent of the required fuel mass which in term is dependent on many other departments, the sensitivity analysis is isolated as much as possible. The tank geometry used for the analysis is cylindrical. The effects on the entire design will be discussed after the sensitivity analysis. The isolation of the analysis means that the parameters as shown in Table 6.4 will be used as input. The parameters subject to the sensitivity analysis are shown in Table 6.5. These parameters have been chosen as they have the biggest effect on the tank wall thickness and required tank volume.

Table 6.4: Parameters fixed for sensitivity analysis

Parameters	Value	Unit
$m_{hydrogen}$	4731	kg
$\dot{m}$	0.0147	$\frac{kg}{s}$

In Figure 6.14 the tanks mass is given as function of the outside temperature. The outside temperature is used to calculate the insulation thickness and therefore the mass of the tank. The tank mass increases as the higher outside temperature requires a thicker insulation thickness to keep the hydrogen cool.

In Figure 6.15 the tank mass is given as a function of the maximum inside pressure. A higher P_{max} requires a higher a thicker aluminum inner liner. This causes an increase in tank weight. Advantages of a higher P_{max} is that the starting pressure in the tank can also be higher increasing the density of the hydrogen allowing a

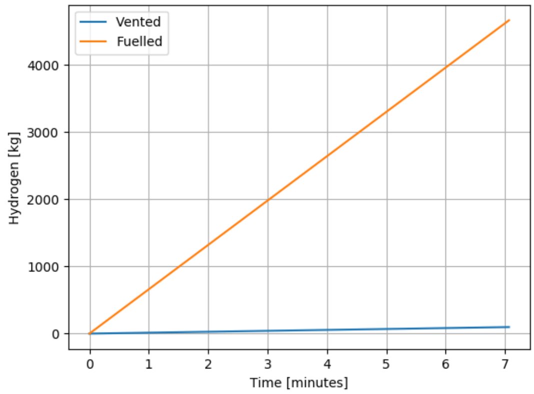

Figure 6.13: Fuelling with venting

Table 6.5: Parameters subject to analysis

Parameters	Range	Comment
$T_{outside}$	$-55C° - 40C°$	This range is from the cruise outside temperature and a hot dessert.
P_{max}	0.101 - 1.2 MPa	Pressures from atmospheric to close to $P_{critical}$ of hydrogen.
$\frac{l}{d}$	1 - 9	The length over diameter ratio of the tank

slightly smaller tank. Trail and error has shown however that this effect is minimal and that a increase in P_{max} increases tank mass irregardless.

In Figure 6.16 shows the tank mass as a function of the length over diameter ratio. It can be seen that a longer tank is heavier than a more spherical tank.

From the sensitivity analysis shows the influence on the tank mass when changing the parameters introduced in Table 6.5. The maximum design pressure has the biggest influence on tank mass and the main argument for increasing it is the decrease in outer tank volume. This can solve issues when fitting the tank in the aircraft if space if limited. After maximum tank pressure, the $\frac{l}{d}$ ratio has the biggest impact on tank mass. Finally the outside temperature which has the least impact on tank mass.

Implications of these results are the following. If the fuselage becomes smaller then there will be less space for the fuel tank requiring a higher density requiring a higher tank pressure making the tank heavier. If the $\frac{t}{c}$ if the fuselage decreases then the tank will have to be slimmer increasing the $\frac{l}{d}$ making the tank heavier.

6.3. Engine sizing

Due to the differences of the fuel properties when using hydrogen compared to a fuel on hydrocarbon basis, the engines and fuel system need to be changed. The changes need to be made in the combustion chamber, fuel system, and a heat exchanger is needed to vaporize the hydrogen[66]. The turbomachinery itself does not need adaptations. Also because the design will be propelled by an open rotor the changes and availability of these engines will also be discussed.

6.3.1. Open rotor

In the midterm phase a propulsion system trade-off was done and resulting from the trade off the open rotor engine came out on top. Based on the required thrust the engine was sized. The thrust was determined in the preliminary sizing and was found to be $170kN$ for take off. The engine was sized based on the design found in [27]. The design found in the paper was around $120kN$ for each engine while only $85kN$ was needed for a single engine. By scaling the engines the dimensions were computed for the required engines. The following formulas were used for the sizing of the engine [53].

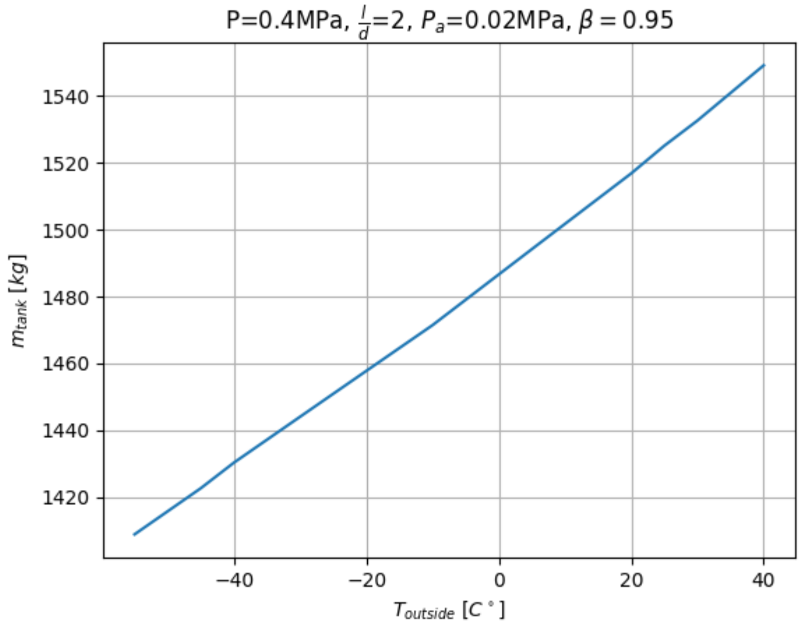

Figure 6.14: Tank mass as function of outside temperature

$$SF = \frac{\frac{T_{TO}}{2}}{T_{sealevel}} \tag{6.23}$$

$$D_{eng_{outer}} = D_{outer} \cdot (SF)^{0.5} \tag{6.24}$$

$$D_{eng_{inner}} = D_{inner} \cdot (SF)^{0.5} \tag{6.25}$$

$$L_{eng} = L \cdot (SF)^{0.4} \tag{6.26}$$

$$W_{eng} = W \cdot (SF)^{1.1} \tag{6.27}$$

In Equation 6.23 the sizing factor is determined. It is based on the ratio between the take off thrust defined by the preliminary sizing and the thrust at sea level from the design found in[27]. The sizing factor is used to determine all the further parameters.

Table 6.6: Input data for engine sizing[27].

Parameter	Value
Thrust at sealevel [N]	121,436
Outer diameter of the propeller [m]	4.21
Inner diameter of the propeller [m]	1.71
Length of the engine [m]	7.07
Weight of the engine [kg]	4,182

In Table 6.6 the input values for the equations are stated. The result of the calculations are shown in Table 6.7.

Table 6.7: Output data for engine sizing

Parameter	Value
Outer diameter of the propeller [m]	3.84
Inner diameter of the propeller [m]	1.56
Length of the engine [m]	6.57
Weight of the engine [kg]	3422

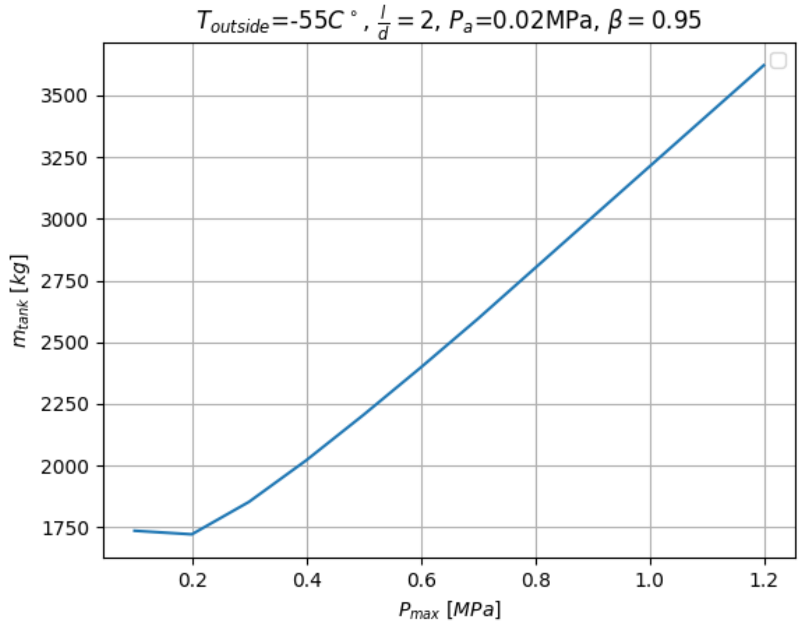

Figure 6.15: Tank mass as function of maximum tank pressure

The next step in the engine analysis is finding a manufacturer. The status quo is that the aircraft is constructed by the manufacturer and that the engine is made by an external party. This system will most likely still be around at the entry into service. Therefore the capabilities of the engine manufacturers should be reviewed. Recently only Safran has demonstrated an open rotor design. The French manufacturer was backed by airbus to research an open rotor design. Other large manufacturers such as General Electric, Rolls Royce and Pratt & Whitney, have recently not shown a working prototype. General Electric and Pratt & Whitney have shown a working prototype in the past, while Rolls Royce has created concepts. The fact that multiple companies have had a working open rotor engine in the past, shows that within 12 years it should be possible to have different options in the open rotor market. This would assume that the engine manufacturers see a potential market for such an engine.

6.3.2. Combustion chamber

When burning hydrogen the only reaction product is water, but due to the heat of the combustion oxygen and nitrogen can start to react which forms NO_x. NO_x is identified as a greenhouse gas and in order to slow down the process of global warming the emission of NO_x should remain under a certain level. In order to ensure combustion with a reduced figure of NO_x production the following measures should be taken.

- Miniaturizing the combustion zone
- Reduce the residence time of the reactants in the combustion zone
- Enhancing the mixing process

For the combustion of hydrogen the enhanced fuel mixture procedures and the miniaturization of the combustion zone can be achieved by micro mixing. This is done by decreasing the size of the fuel injectors and increasing the number of injectors. The micro injectors cause multiple micro flames instead of a larger flame that can be found in current combustion chambers. Multiple smaller flames cause the reaction time to be smaller therefore reducing the combustion zone and the residence time [26].

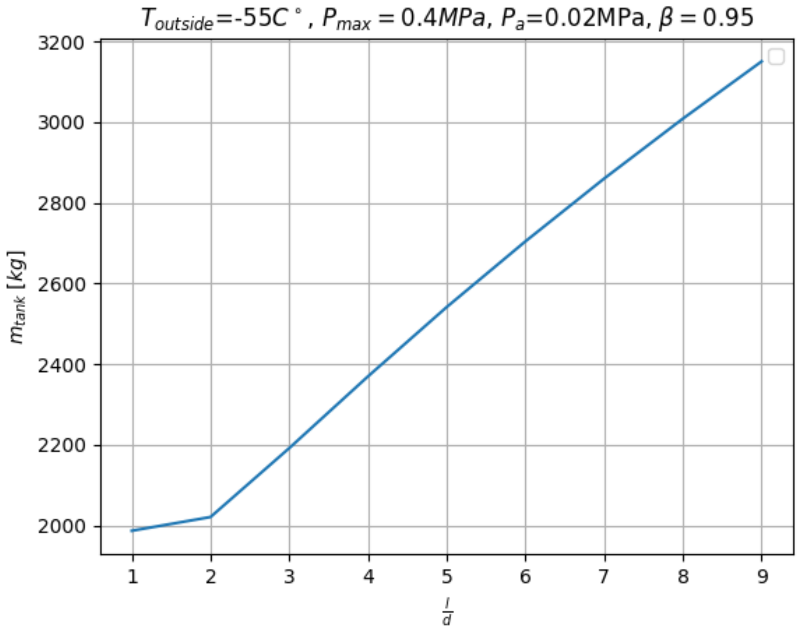

Figure 6.16: Tank mass as function of length over diameter ratio

6.3.3. Emissions

During the combustion of the hydrogen, the hydrogen reacts with oxygen to produce water and energy, following

$$H_2 + \frac{1}{2}O_2 \longrightarrow H_2O \tag{6.28}$$

From the combustion reaction it can be seen that only water is produced, but research has shown that NO_x will also form in the combustion of hydrogen. The rate at which this happens is around 4.3 $\frac{g}{kg}$ hydrogen. For a flight where the fuel tanks will be full and thus $4731kg$ of fuel will be used. Table 6.8 shows the emissions produced at max fuel [17]. The effect of the emissions is discussed in Chapter 12.

Table 6.8: Emissions produced in the combustion of hydrogen

Compound	Amount [kg]
H_2O	42276
NO_x	20.3

6.3.4. Fuel systems

The hydrogen is stored in a single tank making balancing between multiple tank not necessary. However the fuel still has to be transported to the two engines and the APU. Therefore a fuel distribution system should be developed that can fulfill these needs. Furthermore this system should also distribute the fuel during the refill phase in operations[66]. The fuel systems should also cope with the cryogenic temperatures of the fuel. Which does not compromise the other structural parts of the aircraft.

Before the hydrogen can be combusted it needs to be changed into a vapour and heated to improve the efficiency of the combustion. The solution to this problem is putting a heat exchanger in the exhaust of the engine[66]. This will use heat, which would normally be wasted, to heat up the hydrogen, therefore increasing overall thermal efficiency.[42] Similar systems occur in rocket nozzles which are cooled by the fuel, but this is to cool the engine walls instead of heating the fuel.

A weight estimation has been done to determine the weight of the fuel system. The Torenbeek method was used as described in [51].

$$W_{fs} = 80 \cdot (Ne + Nt - 1) + 15 \cdot Nt^{0.5} \cdot \frac{W_f}{kfsp}^{0.333} \tag{6.29}$$

The weight of the fuel system is determined by using Equation 6.29. In which Ne equals the number of engines installed, in this case two. Nt equals the number of tanks, which is one. The W_f is the fuel weight and $kfsp$ is the density of the fuel. The weight of the fuel system includes all the pipelines and pumps necessary to pump the fuel around the different tanks. The results for the weight estimation for the fuel system was $249kg$. Due to the fact that the system needs insulation on the pipes, and different pump system, an unconventionality factor of 1.5 is applied resulting into $373.5kg$. While a kerosene fuel system with 2 engines and 2 fuel tanks, each in every wing, and the weight of the fuel is scaled according to the specific energies of both fuels, gives a weight of $267kg$.

6.3.5. Auxiliary Power Unit

The task of the Auxiliary Power Unit (APU) is to provide electrical power, pneumatic power and Hydraulic power when the aircraft is on the ground. The APU is usually an small gas generator in the back of the aircraft, due to its high power density. The APU further provides power needed on the start up of the main engines. When one or more engines are running the APU becomes abundant as the engines themselves provide enough power, to power the systems in the aircraft.

The APU that is found in the Boeing 737 and the A320 is the Honeywell 131-9[58]. This APU provides 447 kW of power and weights 160 kg [28].Since the size of the HYDRA is similar to these aircraft, it is assumed that a similar system will be installed. The only adaptation to the APU is that it should run on hydrogen. Since the APU will be a small gas turbine the adaptation to the APU will be the same as the adaptation to the combustion chamber of the engine itself stated in subsection 6.3.2.

$$W_{APU} = \frac{0.004 + 0.013}{2} \cdot W_{to} \tag{6.30}$$

A further weight estimation of the power unit has been done with Equation 6.30, which taken from Roskam [51] using the Torenbeek method. Which includes the weight for all the controls and hydraulics as well. Furthermore the dimensions for the APU were taken from data provided by Honeywell. The width of the APU is 83.3 centimeters and the length of the APU is 132.1 meters[28].

6.3.6. Sloshing

When the aircraft starts to manoeuvre the fuel will flow around in the tanks due to the inertia of the liquid. This will effect the dynamics of the vehicle, which is unwanted for operations. Usually devices are created to arrest the movement of the liquid and therefore reducing the negative effect of the fuel movement.

In the current generation of aircraft the fuel is stored in the wingbox. Throughout the wingbox the ribs restrict the movement of the fuel automatically. In HYDRA the tank is not present in the wings, and therefore special barriers should be placed in the tank. In trucks that transport fluids certain barriers are also installed, they are semi walls which restricts most of the fuel movement. With the single elliptical fuel tanks it was therefore opted to install similar devices as in a liquid transporting truck. Thin walls are installed which reduce the effects of sloshing as shown in Figure 6.17. Since the walls are thin and usually have openings in them, the effect on the volume is negligible.

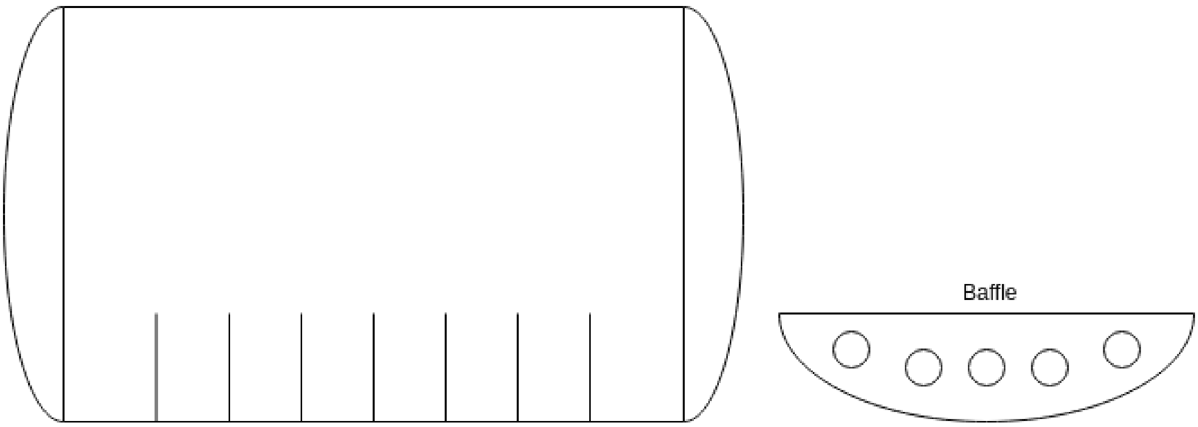

Figure 6.17: Sloshing Barriers

7

Stability and Control

This chapter deals with the stability and control of the aircraft. First, the balance of the aircraft will be discussed, followed by the landing gear positioning. Subsequently, sizing for static and dynamic stability is discussed and results presented.

Two types of stability are discerned: static and dynamic stability. Static stability is the initial tendency of the aircraft to return to its original position when it is disturbed. Dynamic stability implies that any oscillations to the aircraft dampen out over time. For both types, an aircraft can be positively, neutrally or negatively stable. Control implies that the aircraft is sufficiently controllable. This means that the aircraft's control surfaces are sufficiently effective in all operational conditions and that the aircraft responds reasonably quickly to control inputs by the (auto)pilot. Pursuant to CS 25.171, an aircraft must demonstrate (both static and dynamic) longitudinal, directional and lateral stability, in any condition normally encountered during flight. [21] Pursuant to CS 25.143, an aircraft must be safely controllable and manoeuvrable during all flight phases. [21]

7.1. Aircraft balance

The design of the landing gear, horizontal tail and wing location depend greatly on the center of gravity of the aircraft. Where the wings and horizontal tail ensure balance of the aircraft during flight, the landing gear needs to be positioned such that the aircraft can never tip over during the loading of the aircraft, and such that the nose gear carries enough loads to ensure nose wheel steering effectiveness.

As the aircraft needs to be stable for all center of gravity ranges, the maximum and minimum center of gravity locations need to be determined. This is done by means of a loading diagram, which shows the change of the aircraft center of gravity location as payload, fuel and cargo are loaded onto the aircraft, in any possible configuration. If the outcome of the loading diagram for a given wing position does not satisfy any stability and/or other requirements, the wing position can be changed and a new loading diagram generated.

The loading process assumes cargo to be loaded first, followed by passengers and finally fuel. For passengers, two loading sequences are considered: front-to-back and back-to-front loading. The input parameters for the loading diagram can be found in table Table 7.1. It bears noting that the cargo weight includes checked passenger luggage.

Table 7.1: Loading diagram input parameters

Parameter	**Value**	**Unit**
Passenger weight	75	kg
Seat pitch	0.762	m
Number of seats abreast	10	-
Number of rows	17	-
Cargo weight	7250	kg
Fuel weight	4757.28	kg
Boarding sequence	Windows - Middle - Aisles	-

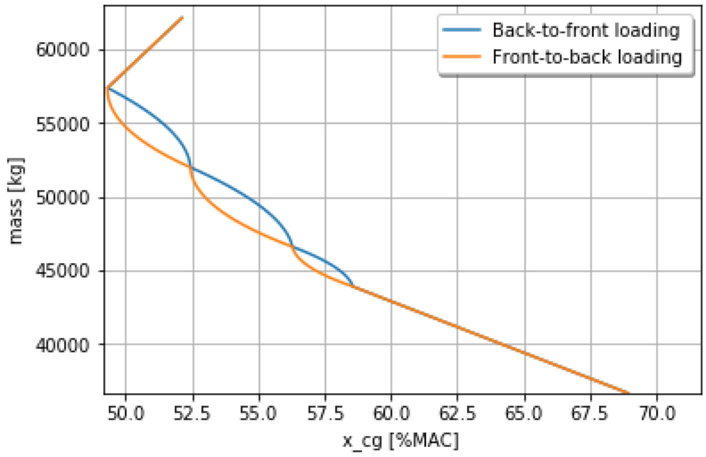

Figure 7.1: Loading diagram

In this loading diagram, the cg as a percentage of the mean aerodynamic chord is plotted against the mass of the aircraft as it is loaded. The plot starts at the center of gravity of the aircraft at OEW, and ends at the cg at MTOW.

The minimum and maximum cg locations from the diagram yield the operational cg range; the range outside of which the cg of the aircraft will not go for any possible loading. As a safety margin, 2 percent is added to these minimum and maximum cg positions, to finally yield the cg range used for stability and control calculations.

Table 7.2: Center of gravity range

Minimum cg position [%MAC]	49.15
Maximum cg position [%MAC]	71.63

7.1.1. Landing gear location

With the cg range known, the landing gear location can be determined. It is important that the landing gear location is such that:

- Nose wheel steering capacity is adequate.
- The aircraft does not tip back during loading due to very aft cg locations.
- The aircraft does not tip back and cause a tail strike during take-off.
- The aircraft does not tip over sideways during tight turns while on the ground.
- Sufficient tip clearance is ensured during high-bank angles when landing.

For the reasons above, the landing gear location is determined using the aft-most cg location from the cg range.

Using the equation from Figure 7.2, in combination with the fact that for adequate nose wheel steering capacity P_n should be equal to or greater than $0.08MTOW$ [50],

$$W - 0.08MTOW - n_s P_m > 0 \tag{7.1}$$

which yields

$$\frac{0.92MTOW}{n_s} > P_m \tag{7.2}$$

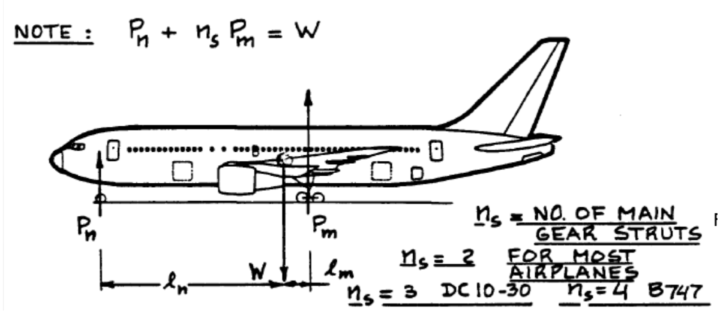

Figure 7.2: Landing gear parameters [50]

Where P_m is the load on the main landing gear, and n_s is the number of main landing gear struts, which is equal to 2. This yields a main landing gear load of 313595 N, and a nose landing gear load of 54538 N.

Then, using the dimension conventions from Figure 7.2,

$$\sum_{CCW+} M_{P_n} = -l_n \cdot W + (l_n + l_m) \cdot P_m = 0 \tag{7.3}$$

Where l_n is equal to 17.29 m (maximum cg distance from the nose) minus 3.8 m (the distance from the nose of the aircraft to the nose gear). Using $MTOW$, and P_m as determined above, solving Equation 7.3 yields a value for l_m of 1.5 m.

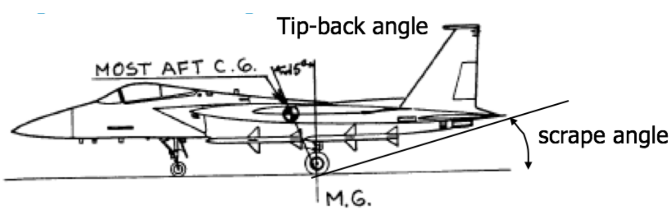

Figure 7.3: Landing gear angles [50]

To avoid tip-over (and subsequently, tailstrike) during take-off, the tip-back angle should be greater than the scrape angle (see Figure 7.3). With the scrape angle of the aircraft being 13 degrees, and the tip-back angle being 27 degrees, the tip-back requirement is satisfied. This scrape angle conflicts with the 14° needed for landing conditions, and must be resolved upon the next iteration.

Finally, to prevent lateral tip-over [50]:

$$y_{MLG} > \frac{l_n + l_m}{\sqrt{\frac{l_n^2 \tan^2(\Psi)}{z^2} - 1}} \tag{7.4}$$

With Ψ being equal to 55 degrees [50], and z being equal to 3 meters (from initial sizing), y_{MLG} is equal to 2.56 meters.

With x measured from the nose of the aircraft, and y measured in spanwise direction from the centerline of the aircraft.

7.2. Static Stability

7.2.1. Sizing for stability and control

In most aircraft, longitudinal stability and control are ensured by means of a horizontal tailplane. This also applied to the HYDRA. This horizontal stabilizer needs to be large enough and far enough from the aerodynamic center of the wings to ensure stability, as well as controllability. For this, a so called scissor plot is used.

Table 7.3: Loading diagram input parameters

Parameter	Value	Unit
$x_{nosegear}$	3.8	m
$x_{maingear}$	22.6	m
$y_{maingear}$	2.56	m
Number of main gear struts	2	-
Number of wheels per main gear bogey	2	-
Number of nose gear struts	1	-
Number of wheels per main nose gear bogey	2	-

A scissor plot shows the ratio of the horizontal tail surface area to the wing surface area versus $x_{cg}[\%MAC]$. For stability, the following equation is used[23]:

$$\bar{x}_{cg} = \bar{x}_{ac} + \frac{C_{L_{\alpha_h}}}{C_{L_{\alpha_{A-h}}}}\left(1 - \frac{d\epsilon}{d\alpha}\right)\frac{S_h l_h}{S\bar{c}}\left(\frac{V_h}{V}\right)^2 - 0.05 \tag{7.5}$$

Where $\bar{x}_{cg}$ is the x location of the cg $[\%MAC]$, $\bar{x}_{np}$ is the x location of the aerodynamic center $[\%MAC]$, $\frac{d\epsilon}{d\alpha}$ is the downwash gradient, $\frac{S_h l_h}{S\bar{c}}$ is the tail volume coefficient, and $\frac{V_h}{V}$ is the ratio of the air velocity between the horizontal tail and the wing. Furthermore, $C_{L_{\alpha_h}}$ is the gradient of the lift coefficient of the horizontal tail, and $C_{L_{\alpha_{A-h}}}$ is the gradient of the lift coefficient of the aircraft minus the horizontal tail. The 0.05 is added as a stability margin.

For control, the equation is [24]

$$\bar{x}_{cg} = \bar{x}_{ac} - \frac{C_{m_{ac}}}{C_{L_{A-h}}} + \frac{C_{L_h}}{C_{L_{A-h}}}\frac{S_h l_h}{S\bar{c}}\left(\frac{V_h}{V}\right)^2 \tag{7.6}$$

Where $[\%MAC]$, $C_{m_{ac}}$ is the moment coefficient about the aerodynamic center, $C_{L_{A-h}}$ is the lift coefficient of the aircraft minus tail, and C_{L_h} is the lift coefficient of the horizontal stabilizer. For a derivation of these equations, the reader is referred to [23] and [24]. The values for the parameters in the stability and control equations are listed in Table 7.4.

Table 7.4: Stability and control input parameters

Parameter	Value	Unit	Source
$\bar{x}_{ac}$	39.2	-	Aerodynamics department
$\frac{d\epsilon}{d\alpha}$	0.0003869	-	Roskam Estimation [49]
$\frac{V_h}{V}$	1	-	Roskam Literature [49]
$C_{L_{\alpha_h}}$	0.01745	1/rad	Aerodynamics department
$C_{L_{\alpha_{A-h}}}$	0.0384	1/rad	Aerodynamics department
$C_{m_{ac}}$	-0.013	-	Aerodynamics department
$C_{L_{A-h}}$	1.3	-	Aerodynamics department
C_{L_h}	-0.8	-	Roskam estimation [49]
l_h	18.08	m	Preliminary sizing
$\bar{c}$	21.814	m	Aerodynamics department

In order to determine the required horizontal stabilizer size for stability and control, Equation 7.5 and Equation 7.6 need to be rewritten to yield the horizontal tail size coefficient $\frac{S_h}{S}$.

$$\frac{S_h}{S} = \frac{1}{\frac{C_{L_{\alpha_h}}}{C_{L_{\alpha_{A-h}}}}\left(1 - \frac{d\epsilon}{d\alpha}\right)\frac{l_h}{\bar{c}}\left(\frac{V_h}{V}\right)^2}\bar{x}_{cg} - \frac{\bar{x}_{ac} - 0.05}{\frac{C_{L_{\alpha_h}}}{C_{L_{\alpha_{A-h}}}}\left(1 - \frac{d\epsilon}{d\alpha}\right)\frac{l_h}{\bar{c}}\left(\frac{V_h}{V}\right)^2} \tag{7.7}$$

$$\frac{S_h}{S} = \frac{1}{\frac{C_{L_h}}{C_{L_{A-h}}}\frac{l_h}{\bar{c}}\left(\frac{V_h}{V}\right)^2}\bar{x}_{cg} + \frac{\frac{C_{mac}}{C_{L_{A-h}}} - \bar{x}_{ac}}{\frac{C_{L_h}}{C_{L_{A-h}}}\frac{l_h}{\bar{c}}\left(\frac{V_h}{V}\right)^2} \tag{7.8}$$

Using the inputs from Table 7.4 and Equation 7.7 and Equation 7.8, the scissor plot can be generated. Additionally, the maximum and minimum operational cg locations are overlaid.

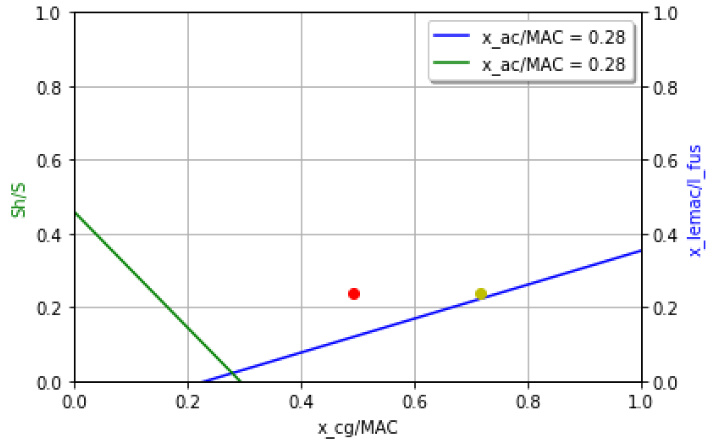

Figure 7.4: Stability and Control plot

As can be clearly seen in Figure 7.4, stability is the limiting factor for the operational cg range. From the plot, a tail size coefficient of 0.2407, which yields a horizontal stabilizer surface area of 71.32 square meters.

The matching of the cg range to the scissor plot is an iterative process. For a certain wing position, the cg range is overlaid on the scissor plot and shifted down until either stability or controllability prevents any further decrease of the horizontal stabilizer size. Then, a new wing position is taken, resulting in a new cg range, which is then again overlaid onto the scissor plot and shifted down to arrive at the smallest horizontal stabilizer size. The plots and values in this section are the final result of these iterations.

As long as the tail size coefficient is such that all possible cg locations fit between the stability and control lines in the scissor plot, the aircraft is statically stable. Clearly, for the HYDRA, this is the case.

7.2.2. Tail Sizing

The tail sizing is following from the static stability determined in subsection 7.2.1. The static stability outputs the ratio of the horizontal tail surface over the reference wing surface. However, in order to fully size the aircraft, the aspect ratio A_h, the taper ratio λ and the sweep angle Λ is needed. These inputs are based on statistics of aircraft and are given in Table 7.5. The table also contains the input for the vertical tail, where S_v/s is also determined with statistics and equals 0.2. Both the horizontal and vertical tail size can be seen in Figure 7.5.

Table 7.5: Inputs needed for the sizing of the horizontal tail.

	Horizontal tail	Vertical tail
A [-]	4	1.1
λ [-]	0.4	0.65
Λ [°]	30 (at LE)	43 (at 0.25c)

Horizontal tail airfoil selection

An important aspect in designing the empennage is choosing an airfoil for the horizontal and vertical tail. Typically the airfoils used for vertical and horizontal tails are symmetric to ensure that they exhibit similar

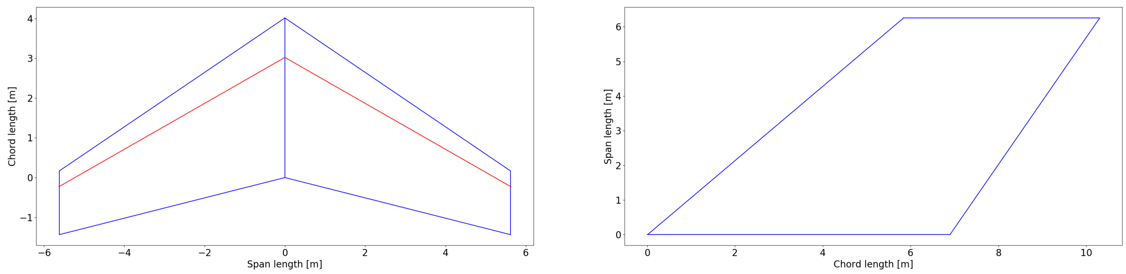

(a) The dimensions of the horizontal tail. (b) The dimensions of the vertical tail.

Figure 7.5: Dimensions of the empennage.

characteristics at both positive and negative angles of attack. Four symmetric NACA airfoils were examined for the horizontal tail; NACA0012, NACA0014, NACA0015 and NACA0018.

Airfoil name	NACA 0012	NACA 0014	NACA 0015	NACA 0018
$C_{p,0}$	-0.6101	-0.4873	-0.5243	-0.6255
$C_{l,max}$	1.601	1.367	1.434	1.198
α_{crit}[°]	17.5	16.5	17.0	15.0
C_{d_0}	0.00768	0.00593	0.0067	0.00664

Table 7.6: Airfoils considered for the horizontal tail plane

From Table 7.6 the three key parameters of the airfoils are shown; $C_{p,min}$ which must be sufficiently low to ensure that flow over the horizontal tail is not supersonic, $C_{l,max}$ to ensure that enough force can be created by the horizontal tail, α_{crit} to ensure that the horizontal tail does not stall before the BWB. With regards to the critical Mach number of the airfoil the NACA 0014 seems the most suitable as this has the least negative $C_{p,min}$. Similarly, with respect to minimizing drag NACA 0014 again seems to be the most suitable with the lowest C_{d_0}. All airfoils would likely stall after the wing except for the NACA 0018 for which the airfoil stall angle is only 15° which is close to the stall angle of the wing, for this reason this airfoil is discarded. Ultimately, the NACA 0014 is chosen for the vertical tail as this should be feasible with respect to critical Mach number and C_l whilst having the least drag of the 4 examined airfoils.

Vertical tail airfoil selection

The vertical tail airfoil is selected in a similar manner to the horizontal tail, again a symmetric airfoil is desirable, as an asymmetric airfoil on the vertical tail would induce an unwanted yawing moment even in straight and level flight without rudder deflection. The airfoils considered for the vertical tail are thinner in order to reduce the structural weight of the vertical tail [5]. The three airfoils considered are the NACA 0009, NACA 0010 and the NACA 0012. For the vertical tail the thickness of the airfoil is leading in order to limit the structural weight of the vertical tail, each of these airfoils are able to achieve the cruise speed of aircraft without experiencing supersonic flow. Ultimately, the thinnest airfoil, the NACA 0009 was chosen.

Last but not least, the downwash caused by the wing affecting the horizontal tail should not cause the tail to stall at little angle of attacks. Hence, the stall due to downwash is verified by looking at the full aircraft configuration, as can be seen in Figure 7.6.

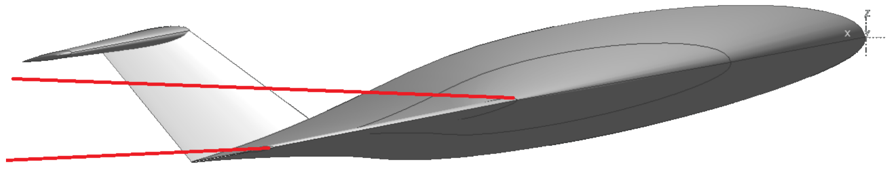

Figure 7.6: Downwash from the outer wing

7.3. Dynamic Stability

7.3.1. Aileron Design

The aileron design is used for the roll control of the aircraft. The design is based on the roll requirement for the aircraft depending on the class of the aircraft. Table 7.7 contains the roll requirements, the aircraft falls under the Class II requirement[4].

Class	Bank angle [°]	roll time [s]
I	60	1.3
II	45	1.4
III	30	1.5
IVA	90	1.3
IVB	90	1.0
IVC	90	1.7

Table 7.7: Roll requirements for the different aircraft classes.

In order to design the aircraft the starting input parameters are needed. In Table 7.8 the parameters are given where b_{start} is the starting spanwise position of the aileron, δ_{max} is the maximum deflection angle and c_a/c_w the chord ratio of the aileron over the wing. b_{start} and δ_{max} are determined statically[55], c_a/c_w is used from section 5.2 accounting for the space between the rear spar and the trailing edge.

Parameters	Value	Unit
b_{start}	85 % of b_{we}	-
δ_{max}	20	°
c_a/c_w	0.4	-

Table 7.8: Input parameters for the aileron design.

From the input parameters in Table 7.8 the rolling moment coefficient due to aileron deflection can be computed with the following equation[55],

$$C_{l_{\delta a}} = \frac{2 c_{l\alpha} \tau}{S_{ref} b} \int_{b_1}^{b_2} c(y) y dy \tag{7.9}$$

where $c_{l\alpha}$ is the lift coefficient of the wing airfoil determined from section 4.1, b is the wing span and $c(y)$ is the wing chord in function of the span position. Th last parameter τ is the aileron effectiveness which can be determined with Figure 7.7.

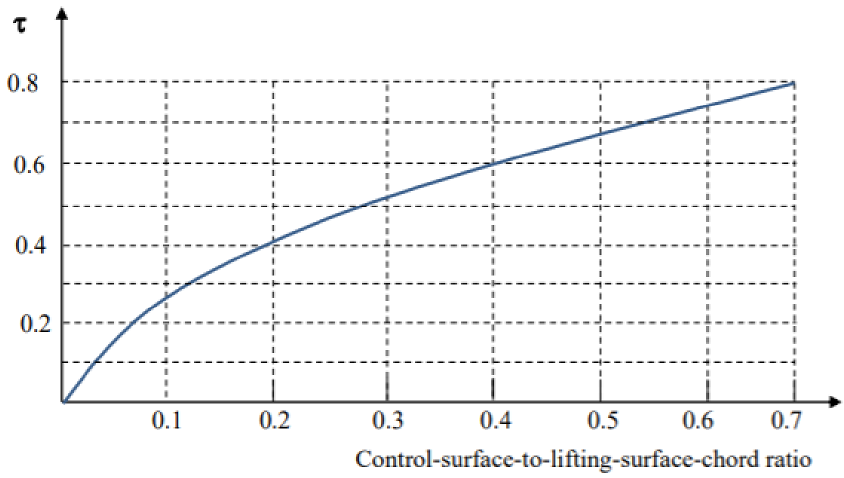

Figure 7.7: The aileron effectiveness as a function of the aileron to wing chord[55].

The change in the rolling moment due to roll rate is determined by the following equation,

$$C_{l_p} = -\frac{4(c_{l_\alpha} + c_{d_0})}{S_{ref} b} \int_{b_1}^{b_2} c(y) y^2 dy \tag{7.10}$$

where c_{d_0} is the drag coefficient at zero lift. Hence from Equation 7.9 and Equation 7.10 the aircraft roll rate P can be computed with the following,

$$P = -\frac{C_{l\delta_a}}{C_{l_p}} \delta a_{max} (\frac{2V_s}{b}) \tag{7.11}$$

where V_s is the stall speed and used from Chapter 3. Hence, in order to determine the span needed Equation 7.9, Equation 7.10 and Equation 7.11 are reiterated until the the bank time to reach 45° equals 1.3s. This results in an aileron span of 1.2618 m, which can be seen in Appendix A.

7.3.2. Stability Derivatives

In order to assess longitudinal and lateral dynamic stability derivatives of the aircraft, two different methods are used. Several derivatives are determined via simplified equations, referenced as SE in Table 7.9 and Table 7.10. The simplified equation used are listed below[40], in addition to that the speed, weight and density are taken for cruise condition.

The non-dimensional aerodynamic force along the X-axis at initial, steady flight condition is given by,

$$C_{X_0} = \frac{W}{\frac{1}{2}\rho V^2 S} sin(\gamma_0) \tag{7.12}$$

The non-dimensional aerodynamic force along the Z-axis at initial, steady flight condition is given by,

$$C_{Z_0} = -\frac{W}{\frac{1}{2}\rho V^2 S} cos(\gamma_0) \tag{7.13}$$

The derivative of the aerodynamic forces along the Z-axis with respect to angle of attack is given by,

$$C_{Z_\alpha} = -C_{L_\alpha} - C_D \tag{7.14}$$

The derivative of the aerodynamic forces along the Z-axis with respect to pitching velocity is is given by,

$$C_{Z_q} = -2C_{N_{h\alpha}} (\frac{V_h}{V})^2 \frac{S_h l_h}{S\bar{c}} \tag{7.15}$$

The derivative of the aerodynamic forces along the Z-axis with respect to angle of attack change is given by,

$$C_{Z_{\dot{\alpha}}} = -C_{N_{h\alpha}} (\frac{V_h}{V})^2 \frac{d\epsilon}{d\alpha} \frac{S_h l_h}{S\bar{c}} \tag{7.16}$$

The moment derivative with respect to the angle of attack change is given by,

$$C_{m_{\dot{\alpha}}} = -C_{N_{h\alpha}} (\frac{V_h}{V})^2 \frac{d\epsilon}{d\alpha} \frac{S_h l_h^2}{S\bar{c}} \tag{7.17}$$

Derivative	Value	Source
C_{X_0}	$9.756{\cdot}10^{-7}$	SE
C_{X_u}	-0.0155	XFLR5
C_{X_a}	0.0603	XFLR5
$C_{X_{\dot{a}}}$	0.0	SE
C_{X_q}	0.0	SE
C_{Z_0}	-0.0260	SE
C_{Z_u}	-0.0004	XFLR5
C_{Z_a}	-0.0584	SE
$C_{Z_{\dot{a}}}$	$-3.955{\cdot}10^{-6}$	SE
C_{Z_q}	-0.0199	SE
C_{m_u}	-0.0006	XFLR5
$C_{m_{\dot{a}}}$	$-6.735{\cdot}10^{-5}$	SE
C_{m_q}	-1.553	XFLR5

Table 7.9: Longitudinal stability derivatives of the aircraft.

Derivative	Value	Source
C_{Y_b}	-0.362	XFLR5
C_{Y_p}	-0.002	XFLR5
C_{Y_r}	0.284	XFLR5
C_{l_b}	-0.0736	XFLR5
C_{l_p}	-0.195	XFLR5
C_{l_r}	0.065	XFLR5
C_{n_b}	0.124	XFLR5
$C_{n_{\dot{b}}}$	0.0	SE
C_{n_p}	-0.0095	XFLR5
C_{n_r}	-0.1011	XFLR5

Table 7.10: Lateral stability derivatives of the aircraft.

7.3.3. Dynamic stability model

In order to assess the dynamic stability and responses of the aircraft, a computer model is required. The software of choice is MATLAB, because of the ease with which dynamic systems can be assessed, and the simplicity of the linear simulation interface to assess dynamic responses to control inputs.

When applying a computer model to analyze a real-world problem, inevitably some simplifications will have to be applied. The equations of motion of an aircraft will be used for the state-space computer model. Some simplifications include the small-angle approximation, linearization of the equations of motion, and steady reference frames. The numerical model is, due to these approximations, only valid for small to moderate control inputs and angles of attack.

Starting with the symmetric and asymmetric equations of motion,

$$\begin{bmatrix} C_{X_u} - 2\mu_c D_c & C_{X_\alpha} & C_{Z_0} & 0 \\ C_{Z_u} & C_{Z_\alpha} + \left(C_{Z_{\dot{\alpha}}} - 2\mu_C\right) D_c & -C_{X_0} & C_{Z_q} + 2\mu_c \\ 0 & 0 & -D_c & 1 \\ C_{m_u} & C_{m_\alpha} + C_{m_{\dot{\alpha}}} D_c & 0 & C_{m_q} - 2\mu_c K_Y^2 D_c \end{bmatrix} \begin{bmatrix} \hat{u} \\ \alpha \\ \theta \\ \frac{q\bar{c}}{V} \end{bmatrix} = \begin{bmatrix} -C_{X_{\delta_e}} \\ -C_{Z_{\delta_e}} \\ 0 \\ -C_{m_{\delta_e}} \end{bmatrix} \delta_e \tag{7.18}$$

$$\begin{bmatrix} C_{Y_\beta}-\left(C_{Y_{\dot\beta}}-2\mu_b\right)D_b & C_L & C_{Y_p} & C_{Y_r}-4\mu_b \\ 0 & -\frac{1}{2}D_b & 1 & 0 \\ C_{\ell_\beta} & 0 & C_{\ell_p}-4\mu_b K_X^2 D_b & C_{\ell_r}+4\mu_b K_{XZ} D_b \\ C_{n_\beta}+C_{n_{\dot\beta}}D_b & 0 & C_{n_p}+4\mu_b K_{XZ} D_b & C_{n_p}-4\mu_b K_Z^2 D_b \end{bmatrix} \begin{bmatrix} \beta \\ \phi \\ \frac{pb}{2V} \\ \frac{rb}{2V} \end{bmatrix} = \begin{bmatrix} -C_{Y_{\delta_a}} & -C_{Y_{\delta_r}} \\ 0 & 0 \\ -C_{\ell_{\delta_a}} & -C_{\ell_{\delta_r}} \\ -C_{n_{\delta_a}} & -C_{n_{\delta_r}} \end{bmatrix} \begin{bmatrix} \delta_a \\ \delta_r \end{bmatrix} \tag{7.19}$$

Since these equations are linear first order differential equations, they can be represented by means of a Linear Time-Invariant (LTI) state-space system of the form

$$\dot{\mathbf{x}} = \mathbf{A}\,\mathbf{x} + \mathbf{B}\,\mathbf{u} \tag{7.20a}$$

$$\mathbf{y} = \mathbf{C}\,\mathbf{x} + \mathbf{D}\,\mathbf{u} \tag{7.20b}$$

Where **A** is the state-matrix, **B** the input matrix, **C** the output matrix and **D** the feed-through matrix.

The equations of motion in LTI state-space form are as follows:

$$\begin{bmatrix} -2\mu_c \frac{\bar c}{V}\frac{d}{dt} & 0 & 0 & 0 \\ 0 & \left(C_{Z_{\dot\alpha}}-2\mu_C\right)\frac{\bar c}{V}\frac{d}{dt} & 0 & 0 \\ 0 & 0 & -\frac{\bar c}{V}\frac{d}{dt} & 0 \\ 0 & C_{m_{\dot\alpha}}\frac{\bar c}{V}\frac{d}{dt} & 0 & -2\mu_c K_Y^2 \frac{\bar c}{V}\frac{d}{dt} \end{bmatrix} \begin{bmatrix} \hat u \\ \alpha \\ \theta \\ \frac{q\bar c}{V} \end{bmatrix} = \begin{bmatrix} -C_{X_u} & -C_{X_\alpha} & -C_{Z_0} & 0 \\ -C_{Z_u} & -C_{Z_\alpha} & C_{X_0} & -\left(C_{Z_q}+2\mu_c\right) \\ 0 & 0 & 0 & -1 \\ -C_{m_u} & -C_{m_\alpha} & 0 & -C_{m_q} \end{bmatrix} \begin{bmatrix} \hat u \\ \alpha \\ \theta \\ \frac{q\bar c}{V} \end{bmatrix} + \begin{bmatrix} -C_{X_{\delta_e}} \\ -C_{Z_{\delta_e}} \\ 0 \\ -C_{m_{\delta_e}} \end{bmatrix} \delta_e \tag{7.21}$$

$$\begin{bmatrix} \left(C_{Y_{\dot\beta}}-2\mu_b\right)\frac{b}{V}\frac{d}{dt} & 0 & 0 & 0 \\ 0 & -\frac{1}{2}\frac{b}{V}\frac{d}{dt} & 0 & 0 \\ 0 & 0 & -4\mu_b K_X^2 \frac{b}{V}\frac{d}{dt} & 4\mu_b K_{XZ}\frac{b}{V}\frac{d}{dt} \\ C_{n_{\dot\beta}}\frac{b}{V}\frac{d}{dt} & 0 & 4\mu_b K_{XZ}\frac{b}{V}\frac{d}{dt} & -4\mu_b K_Z^2\frac{b}{V}\frac{d}{dt} \end{bmatrix} \begin{bmatrix} \beta \\ \phi \\ \frac{pb}{2V} \\ \frac{rb}{2V} \end{bmatrix} = \begin{bmatrix} -C_{Y_\beta} & -C_L & -C_{Y_p} & -\left(C_{Y_r}-4\mu_b\right) \\ 0 & 0 & -1 & 0 \\ -C_{\ell_\beta} & 0 & -C_{\ell_p} & -C_{\ell_r} \\ -C_{n_\beta} & 0 & -C_{n_p} & -C_{n_r} \end{bmatrix} \begin{bmatrix} \beta \\ \phi \\ \frac{pb}{2V} \\ \frac{rb}{2V} \end{bmatrix} + \begin{bmatrix} -C_{Y_{\delta_a}} & -C_{Y_{\delta_r}} \\ 0 & 0 \\ -C_{\ell_{\delta_a}} & -C_{\ell_{\delta_r}} \\ -C_{n_{\delta_a}} & -C_{n_{\delta_r}} \end{bmatrix} \begin{bmatrix} \delta_a \\ \delta_r \end{bmatrix} \tag{7.22}$$

For the symmetric and asymmetric case respectively, the **C** matrices are

$$\mathbf{C} = \begin{bmatrix} V & 0 & 0 & 0 \\ 0 & 1 & 0 & 0 \\ 0 & 0 & 1 & 0 \\ 0 & 0 & 0 & \frac{V}{\bar c} \end{bmatrix} \tag{7.23}$$

$$\mathbf{C} = \begin{bmatrix} V & 0 & 0 & 0 \\ 0 & 1 & 0 & 0 \\ 0 & 0 & \frac{2V}{b} & 0 \\ 0 & 0 & 0 & \frac{2V}{b} \end{bmatrix} \tag{7.24}$$

For the symmetric case the feed-through matrix **D** is of dimension 4x1, and for the asymmetric case of dimension 4x2. In both cases they contain only zeros.

7.3.4. Symmetric stability and response

Using the stability and control derivatives from subsection 7.3.2, the eigenvalues and corresponding eigenmotions of the aircraft can be determined. For longitudinal dynamic stability, two eigenmodes can be discerned: short period motion and phugoid motion.

In order to calculate the eigenvalues for the symmetric case, equation Equation 7.25 is used.

$$\begin{vmatrix} C_{X_u} - 2\mu_c\lambda_c & C_{X_\alpha} & C_{Z_0} & 0 \\ C_{Z_u} & C_{Z_\alpha} + \left(C_{Z_{\dot\alpha}} - 2\mu_c\right)\lambda_c & -C_{X_0} & C_{Z_q} + 2\mu_c \\ 0 & 0 & -\lambda_c & 1 \\ C_{m_u} & C_{m_\alpha} + C_{m_{\dot\alpha}} & 0 & C_{m_q} - 2\mu_c K_Y^2 \lambda_c \end{vmatrix} = 0 \tag{7.25}$$

Finding the determinant and solving for 0 yields the eigenvalues. A plot of these eigenvalues can be found in Figure 7.8.

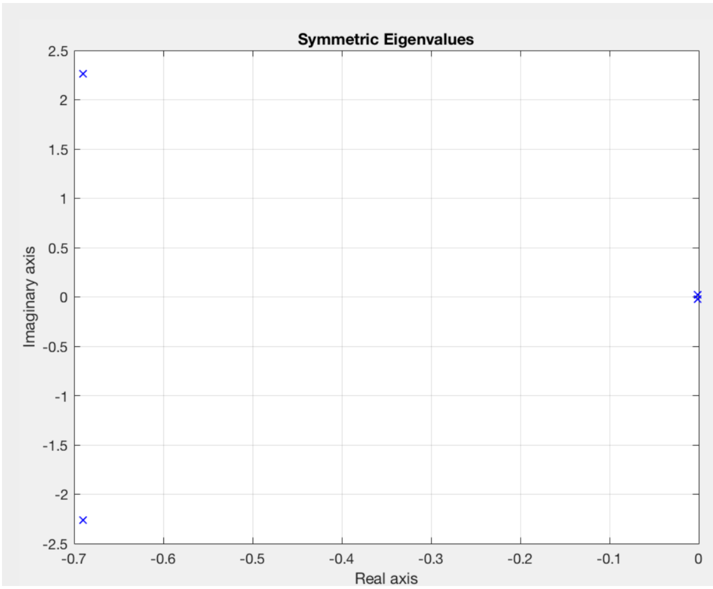

Figure 7.8: Symmetric eigenvalues

Now, the period P and the time to half amplitude $T_{\frac{1}{2}}$ can be determined.

$$P = \frac{2\pi}{\eta_c}\frac{\bar{c}}{V} \tag{7.26a}$$

$$T_{\frac{1}{2}} = -\frac{0.693}{\xi_c}\frac{\bar{c}}{V} \tag{7.26b}$$

Where ξ_c and η_c are the non-dimensional real and imaginary parts of the eigenvalues.

Mode	Eigenvalue	Period P (s)	$T_{\frac{1}{2}}$
Short period	$-0.6902 \pm 2.2648i$	0.254	0.0919
Phugoid	$-0.0016 \pm 0.0225i$	25.6092	39.3665

Table 7.11: Non-dimensional symmetric eigenvalues and parameters

The Routh-Hurwitz criterion states that in order for a system to be dynamically stable, the real parts of its eigenvalues should all be negative [41]. As can be seen, for the symmetric case, the real parts of the eigenvalues are indeed negative and thus the time-responses to control inputs and/or disturbances are stable.

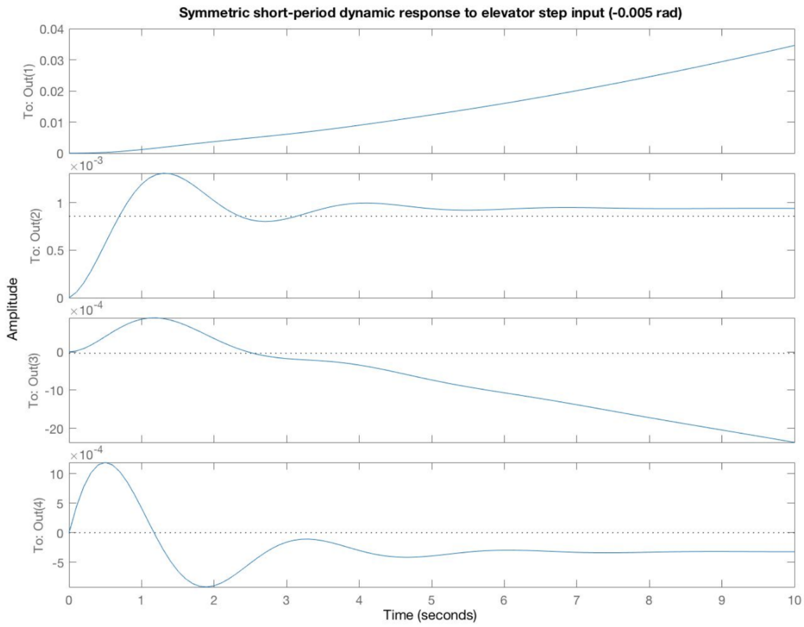

Figure 7.9: Short-period response

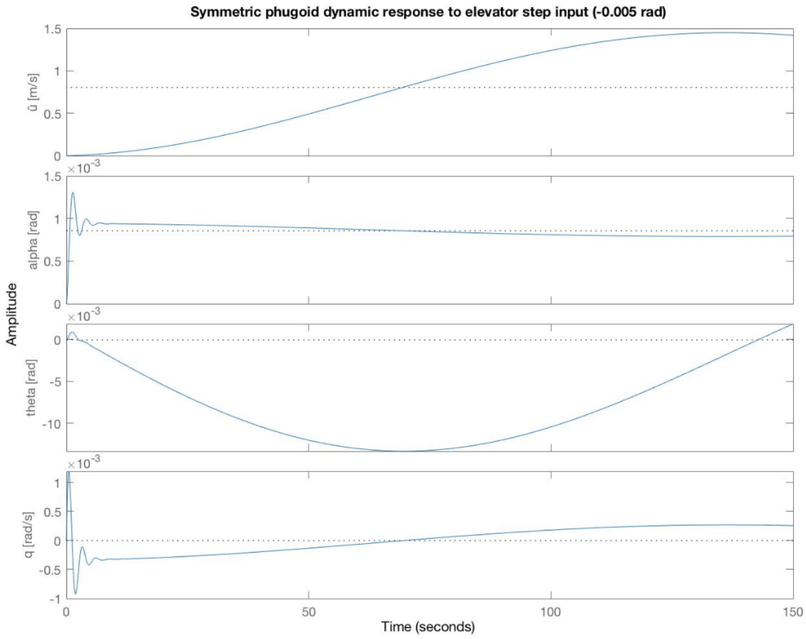

Figure 7.10: Phugoid response

7.3.5. Asymmetric stability and response

For asymmetric dynamic stability, three eigenmodes can be discerned: first aperiodic, second aperiodic and periodic.

Calculating the eigenvalues for the asymmetric case:

$$\begin{vmatrix} C_{Y_\beta} - \left(C_{Y_{\dot{\beta}}} - 2\mu_b\right)\lambda_b & C_L & C_{Y_p} & C_{Y_r} - 4\mu_b \\ 0 & -\frac{1}{2}\lambda_b & 1 & 0 \\ C_{\ell_\beta} & 0 & C_{\ell_p} - 4\mu_b K_X^2 \lambda_b & C_{\ell_r} + 4\mu_b K_{XZ}\lambda_b \\ C_{n_\beta} + C_{n_{\dot{\beta}}}\lambda_b & 0 & C_{n_p} + 4\mu_b K_{XZ}\lambda_b & C_{n_p} - 4\mu_b K_Z^2 \lambda_b \end{vmatrix} = 0 \tag{7.27}$$

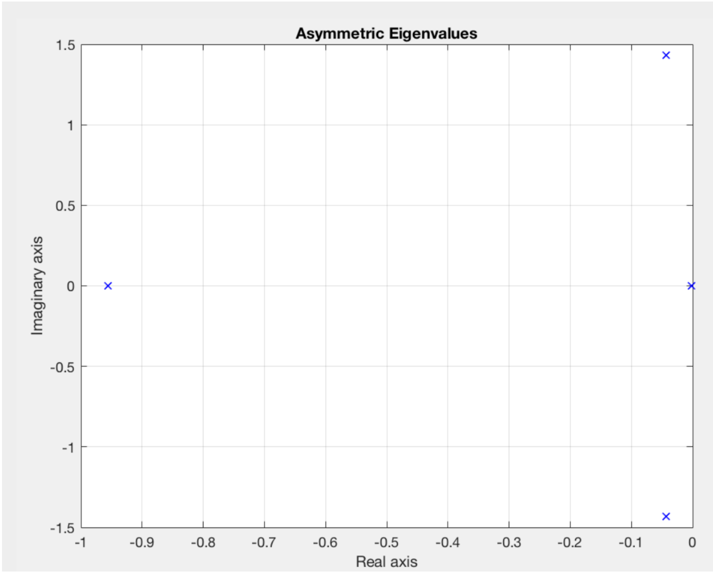

Figure 7.11: Asymmetric eigenvalues

Now, for the period P and the time to half amplitude $T_{\frac{1}{2}}$:

Mode	Eigenvalue	Period P (s)	$T_{\frac{1}{2}}$
First aperiodic	0.0170	N/A	−5.03
Second aperiodic	−0.498	N/A	0.172
Periodic	-0.0416 ± 0.396	1.966	2.063

Table 7.12: Non-dimensional asymmetric eigenvalues and parameters

Again, it can be seen that the real parts of all eigenvalues are negative, and that the aircraft is thus asymmetrically stable.

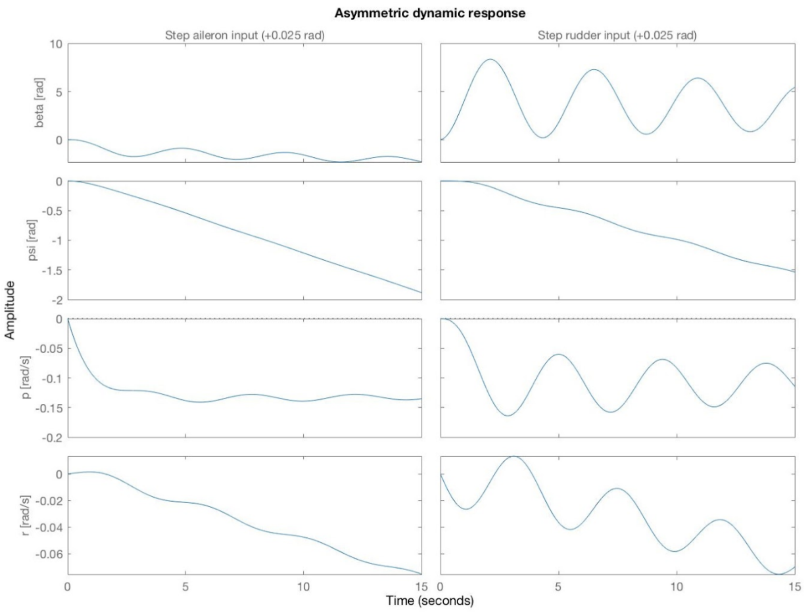

Figure 7.12: Short-period response

7.4. Verification and Validation

The methods and inputs used in previous sections need to be verified in order to continue designing in the next phases. After verification, the results obtained need to be validated with existing data. Hence, for the verification of the model the inputs and the model itself are verified.Table 7.13 contains the expected signs and the actual signs of the stability derivatives[40]. However, the order of magnitude is difficult to verify for the stability derivatives as it cannot be compared to the magnitudes of similar BWB..

Table 7.13: Lateral stability derivatives sign verification.

Derivative	Actual sign	Expected sign
C_{Y_b}	-	-
C_{Y_p}	-	-
C_{Y_r}	+	+
C_{l_b}	-	-
C_{l_p}	-	-
C_{l_r}	+	+
C_{n_b}	+	+
$C_{n_{\dot{b}}}$	0.0	/
C_{n_p}	-	-
C_{n_r}	-	-

The model used to assess dynamic stability is verified by using existing data about current aircraft, filling in the respective stability derivatives and the general aircraft characteristics. Then, the model outputs and response curves are compared to those of existing aircraft to see if they match. Additionally, stability results are compared between the model used for HYDRA and the verification data.

Validation requires results from real flight of the aircraft. However, the validation through flight test data is not possible at this stage. Validation is only possible after building a prototype as there is no current BWB flying around with accessible flight test data.

8

Aircraft Performance

In this chapter the performance of the aircraft in different situations are discussed. The flight envelope and turning performances determine the loads that the aircraft has to support during flight. Additionally, the performance of different phases are presented, including take-off, climb, cruise, descent and landing. Lastly, general results for the global flight are presented. A simulation model is used in order to obtain the performances at a certain instant in time.

8.1. Flight Envelope

The flight envelope, in addition with the turning performance, is used to determine the maximum loads that the aircraft must be able to sustain during flight. Hence, for the flight envelope a maneuver load diagram is given in Figure 8.1. In this diagram the load factor n is given as a function of the speed V. In Figure 8.1 line O-A is determined by,

$$n = \frac{qC_{L_{max}}}{W/S} \tag{8.1}$$

where n is the load factor, q is the dynamic pressure, $C_{L_{max}}$ is the maximum lift coefficient in the clean configuration and W/S the wing loading of the aircraft. The $C_{L_{max}}$ and W/S are given in Chapter 3. The limits for the load factor are dictated by the CS 25 regulations, where line A-D represents the maximum positive load factor and line H-F the maximum negative load factor [21]. The dive speed V_d is also specified by CS 25[21]. V_c and V_s are the cruise and stall speed respectively.

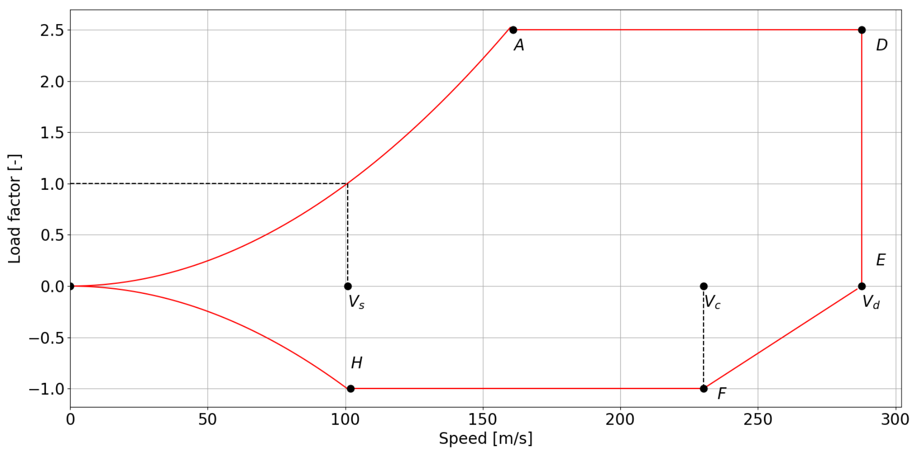

Figure 8.1: The Maneuver load diagram

From Figure 8.1 it is clear that the upper and lower limit for the load factor are illustrated by line A-D and line H-F. However, the load factors during turning are also considered in section 8.2 in order to verify if the upper limit is indeed 2.5.

8.2. Turning Performance

The turning performance of the aircraft contains the load factors on the aircraft during turning, the minimum radius and minimum time to turn. Figure 8.2 illustrates the determination of the maximum loads. Figure 8.2a shows the performance of the aircraft for different load factors, where the thrust is constant as it assumed that the aircraft turns at a constant altitude and the drag as a function of speed is given by,

$$D = nC_D q V^2 S \tag{8.2}$$

where C_D is the drag coefficient, q the dynamic pressure, V the airspeed and S the wing surface. C_D is calculated from the C_L-C_D relation given in Chapter 4. It is important to note that for the starting point of the drag calculation at every load factor, the stall speed is considered. Hence, $C_{L_{max}}$ is accounted for in the determination of C_D; and also the speed V, given by,

$$V = \sqrt{\frac{nW}{S}\frac{2}{\rho}\frac{1}{C_L}} \tag{8.3}$$

where W is the aircraft weight and ρ the air density. For the weight the maximum take-off weight is used and the air density is calculated by means of the ISA standards at a height of 1000 m. From the load factor, the required turn radius follows. The turn radius is calculated with the following relation[54]:

$$R = \frac{V^2}{g\sqrt{n^2-1}} \tag{8.4}$$

where R is the turn radius and g the gravitational constant. This relation in combination with the maximum load factors obtained in Figure 8.2b results in minimum turn radii for different speeds given in Figure 8.3a. Looking at Figure 8.3a, the airspeed for the minimum turn radius is different to the airspeed for the maximum load factor.

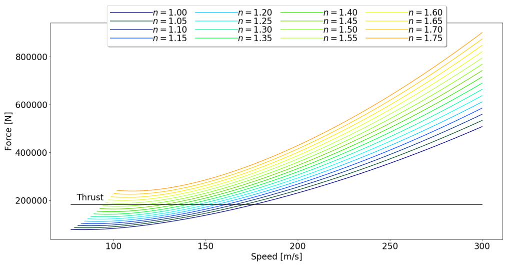

(a) Performance diagram for multiple load factors.

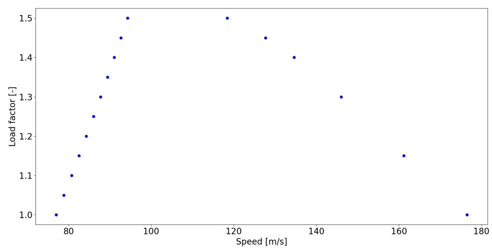

(b) Load factors as a function of speed where thrust equals drag.

Figure 8.2: Determination of the maximum load factors at different speeds.

Last but not least, from the load factor and turn radius the minimum time to turn can be computed. Figure 8.3b illustrates the turning time as a function of speed. The turning time is simply determined by the following relation, using the turn radii found in Figure 8.3a, where the time for a full turn (360°) is considered:

$$T_{2\pi} = \frac{2\pi R}{V} \tag{8.5}$$

Hence, the maximum load factor, minimum turn radius and the minimum turning time are determined. The final results are given in Table 8.1.

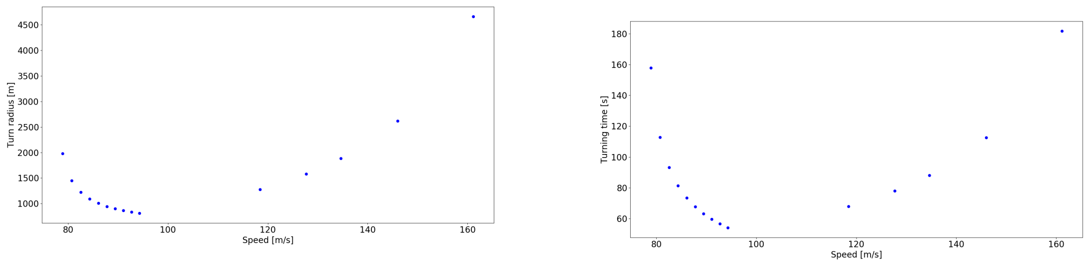

(a) The turn radius as a function of speed, where thrust equals drag.

(b) Turning time as a function of speed.

Figure 8.3: Determination of the maximum load factors at different speeds.

n_{max} [-]	1.5
R_{min} [m]	810.36
T_{min} [s]	54

Table 8.1: Final results for the turning performance.

8.3. Take-off

In this section the take-off phase is discussed. The ground and airborne phases are both included in take-off calculations. The ground phase is considered as the distance until the aircraft reaches its lift-off speed. The lift-off speed is determined with the following equation,

$$V_{LOF} = \sqrt{\frac{W}{S}\frac{2}{rho}\frac{1}{C_{L_{maxTO}}}} \tag{8.6}$$

where V_{LOF} is the lift-off speed and $C_{L_{maxTO}}$ is the maximum lift coefficient at take-off. For the weight the maximum take-off weight is considered and a sea-level take-off is assumed. The speed until lift-off is computed with the equations of motion given below:

$$\frac{W}{g}\frac{dV}{dt} = T - D - \mu(W - L) \tag{8.7}$$

$$\frac{dx}{dt} = V \tag{8.8}$$

where μ is the friction coefficient[20]. The drag is computed with the C_D-C_L relation given in Chapter 4. The specific inputs are given in Table 8.2. The airborne distance for take-off is determined by approximating the initial take-off as a circular movement until the aircraft reaches the screen height that can be seen in Figure 8.4. However, in Figure 8.4 the circular motion is not visible only the screen height.

$C_{L_{maxTO}}$	1.1
μ	0.02
Thrust setting	80 % of T_{TO}

Table 8.2: Specific inputs for take-off.

8.4. Climb

After taking off the aircraft has to climb up to the cruise altitude. The climbing performance is defined by the climb rate of the aircraft. For the climbing phase a constant indicated airspeed is opted as the climbing

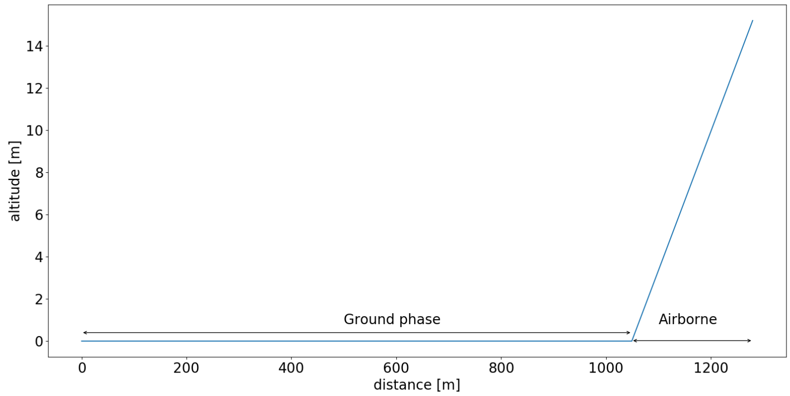

Figure 8.4: The take off distance as a function of height.

strategy. Furthermore, the thrust change with altitude is assumed to be proportional with the density change. Hence, the steady rate of climb (V constant), following from the equation of motion for climb given by

$$T - D = W sin(\gamma) \tag{8.9}$$

where γ is the climb angle. Additionally, a steady symmetric flight is assumed, meaning that the speed and climb angle are kept constant. The steady rate of climb is then determined with the following equation:

$$RC_{st} = \frac{P_a - P_r}{W} \tag{8.10}$$

where P_a is the available power and P_r is the required power. Equation 8.10 is only valid when assuming $\frac{dV}{dt}$ equal to zero and a constant flight path angle. The actual rate of climb can be calculated with the following equation[54]:

$$\frac{RC}{RC_{st}} = \frac{1}{1 + \frac{V}{g}\frac{dV}{dH}} \tag{8.11}$$

where H is the altitude and the change in velocity with altitude is given by

$$\frac{dV}{dH} = V_{EAS}\frac{d(\sqrt{\frac{\rho_0}{\rho}})}{dH} \tag{8.12}$$

where V_{EAS} is the equivalent airspeed and is assumed equal to the indicated airspeed, considering that the flow is incompressible [11]. The change in density with altitude is derived from the ISA standard atmosphere conditions. Hence, the rate of climb over the climb phase is illustrated in Figure 8.5a. The sudden changes in rate of climb in the beginning of the climb are due to considering some flight maneuvers. It is taken into consideration that the aircraft's rate of climb increases after take-off by changing the flight path angle and at a later stage the thrust setting is decreased. Figure 8.5b depicts the time needed to climb to the cruise altitude. As can be seen from both plots, the climb does not completely end at 11000m. The reason is that in flight the pilot or autopilot adjust the aircraft trajectory when approaching the cruise altitude.

8.5. Cruise

The cruise phase constraints the range of the flight. The cruise characteristics are given in Table 8.3. In order to model the cruise, several assumptions had to be made: the cruise speed and the angle of attack are kept constant. Hence, in order to keep these constant the aircraft is slightly increasing its altitude. In theory this

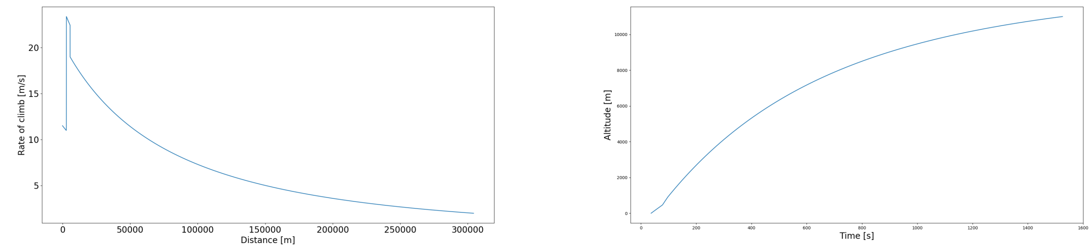

(a) The rate of climb over the climb distance.

(b) The climbing time until reaching the cruise altitude.

Figure 8.5: Determination of the climb characteristics.

can be done by linearly increasing the altitude over the cruise distance, as seen in Figure 8.6, however in reality this is applied in step climbs during cruise.

Parameter	Value	Unit
Altitude	11000	m
Density	0.3636	kg/m^3
Thrust setting	70 %	-
Mach number	0.75	-

Table 8.3: Input parameters for the cruise phase.

The difference between Figure 8.6a and Figure 8.6b lies in the fuel fraction. For Figure 8.6a a fuel fraction based on the design range determined in Chapter 3 is used, Figure 8.6b considers a fuel fraction based on the maximum fuel.

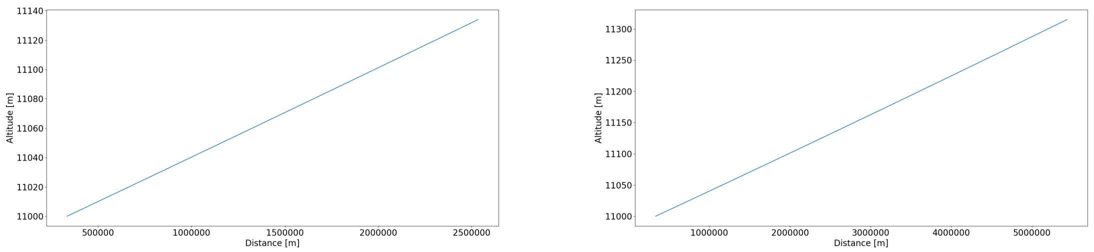

(a) The cruising distance as a function of altitude for the design range.

(b) The cruising distance as a function of altitude for maximum fuel.

Figure 8.6: Determination of the cruise characteristics.

8.6. Descent

The descent performance is based on the same computations as the climb performance in section 8.4. The difference in the climb phase is that the thrust level is decreased, causing the aircraft to descend. Similar to the climb phase, the indicated airspeed is kept constant for the descent phase. Looking at Figure 8.7a the descent rate does not reach zero at the end of the descent phase, instead it stays significantly high. This is because at the end of descent phase the aircraft adjusts for the glide slope trajectory towards the landing field. Figure 8.7b indicates that the descent phase lasts for approximately 30 minutes.

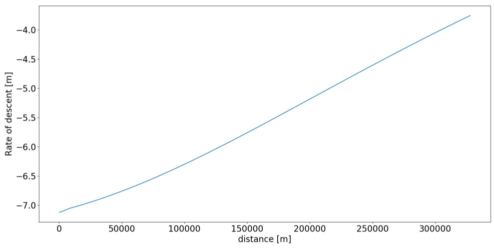

(a) The rate of descent over the climb distance.

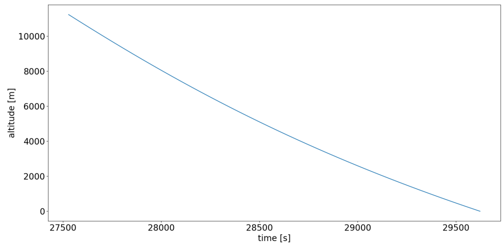

(b) The descent time of the aircraft starting from the cruise altitude.

Figure 8.7: Determination of the descent characteristics.

8.7. Landing

Similar to take-off, the landing consists of the airborne and the ground phase. The airborne phase is determined similarly to section 8.3. However, the ground phase is based on the following equation of motion,

$$\frac{W}{g}\frac{dV}{dt} = -T_{rev} - D - \mu(W - L) \tag{8.13}$$

where T_{rev} is the reverse thrust and assumed zero and μ is the wheel friction. For the drag the C_L-C_D relation Chapter 4 is used where the $C_{L_{max}}$ is considered. The landing distance can be seen in Figure 8.8, the beginning altitude is the screen height of 15 m. As can be seen, the airborne phase indicated is including a part of the zero altitude landing distance. This is because the transition time and distance between airborne and ground phase is included in the landing distance.

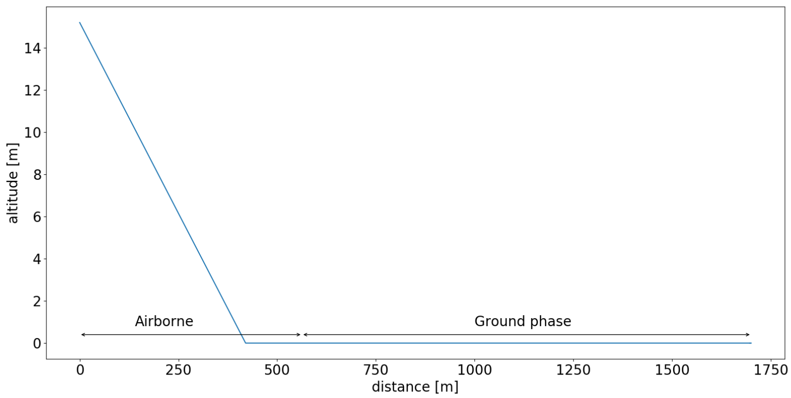

Figure 8.8: The landing distance of the aircraft.

8.8. Overall flight

Combining the flight phases from previous sections, the overall flight characteristics can be obtained. Figure 8.10 illustrates the flight distance for the design parameters from Chapter 3. The design flight characteristics are given in Figure 8.9. The calculation for the fuel burnt in every phase is based on the mass flow determination in Chapter 6.

Parameter	Value
Range [km]	2857
Flight time	3hrs 39min
Fuel burnt [kg]	1920

Figure 8.9: Design flight characteristics.

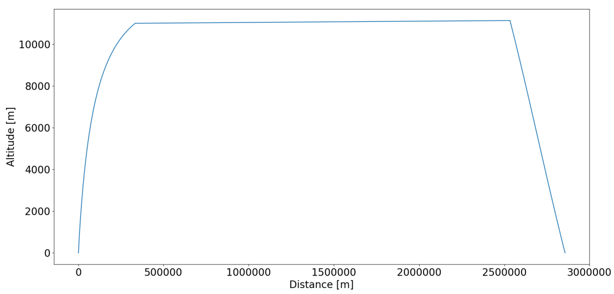

Figure 8.10: Distance of the whole flight as a function of altitude.

9

RAMS Characteristics

This chapter discussed the reliability, availability, maintainability and safety of HYDRA. First the reliability and availability will be discussed in section 9.1. Next, the maintainability will be addressed in section 9.2. Finally the safety aspects will be discussed in section 9.3.

9.1. Reliability and availability

The availability of the aircraft is defined as the amount of days in the year that the aircraft is operational. This means that availability of the aircraft is very much dependent on the amount of maintenance required which will be discussed in section 9.2. Turnaround time is also an important factor for the availability of the aircraft. The turn round time is determined by how quickly the airport can make the aircraft flight ready and is in part dependent on the design of the aircraft. The turn round time of an A320 can be seen in Figure 9.1 below.

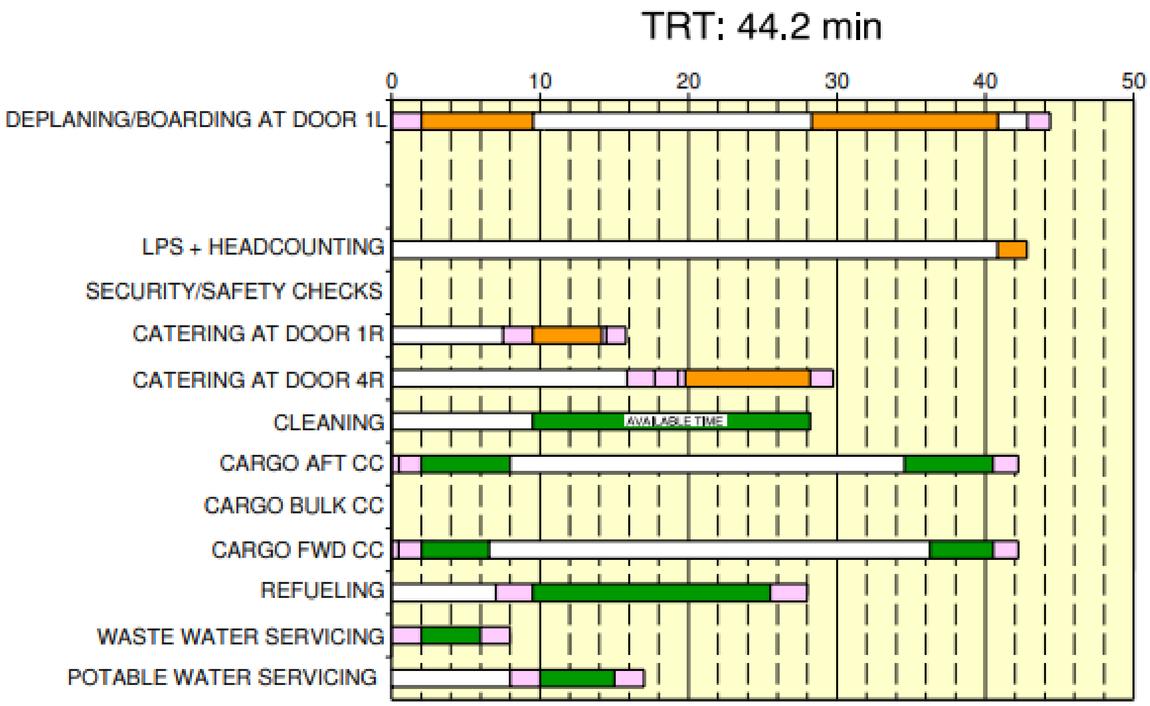

Figure 9.1: Turn round time of A320 [8]

Activities that can potentially change due to the blended fuselage and cryogenic fuel are refuelling, and passenger and cargo loading/unloading. It has been shown in subsection 6.2.1 that the tanks can be fuelled in the same time by setting the massflow to $5\frac{kg}{s}$ or $71\frac{l}{s}$. This is more massflow in volume compared to the A320 which requires $28\frac{l}{s}$ to refuel in 16 minutes therefore requiring bigger pumps. No showstoppers have however been found that indicate that these rates are not achievable.

The reliability of the aircraft is defined as

$$R = \sum_{i=1}^{n} 1 - P_{failure_i} \tag{9.1}$$

The total reliability of the aircraft is dependent on the reliability and therefore the probability of failure of each subsystem. The reliability of each subsystem is hard to approximate because of the early stage of the design. It is therefore assumed that the new systems in HYDRA will have similar probability of failure compared to conventional aircraft.

9.2. Maintainability

Certain characteristics of HYDRA will change the maintenance process. The use of hydrogen tanks requires more inspection compared to conventional fuel tanks. This is because of more complex fuel systems and pressurization cycles. The top mounted engines also make inspection more challenging as they are much higher from the ground compared to conventional below the low wing mounted engines. This will require the airport personnel to use lifters to reach these heights. The scheduled maintenance guidelines are shown in Table 9.1[6].

Check	When	Tasks	Hours needed
Daily checks	Daily	Visual inspection	0.5
A	≈ 250 flight hours	Filter replacement, emergency equipment inspection and lubrication	20 - 50
B	6 months	Systems operational and functional checkouts	120 - 150
C	20 - 24 months	Thorough inspection of aircraft systems	6000
D	6 years	All aircraft systems are taken apart, inspected and reassembled	50000

Table 9.1: Scheduled maintenance

Where HYDRA differs from conventional aircraft is the B and C checks. When performing B checks and testing the operational and functional performance of the aircraft systems, the fuel tanks also have to be tested. This includes pressurization and temperature tests.

9.3. Safety

Characteristics that have influence on safety are the location of the engines and the hydrogen fuel tanks. The engines are placed at the very back of the aircraft behind the pressure bulk head of the cabin. This means that an engine blade failure will not pose a threat to depressurization of the cabin. The cryogenic tank is also placed behind the cabin compared to in the wingbox in conventional configurations. This has the advantage that a fire in the cabin or cargo department has less risk of spreading to the fuel tank. HYDRA will have a $3-6-3$ layout as seen in Figure 3.3b which is wider than compared to the A320 which has a $3-3$ layout. HYDRA has four doors on each side of the aircraft. Half of those doors are type I and the other half type III. This allows for the aircraft to still be evacuated in the required 90 seconds meaning that it is compliant with the regulation.

10
Production Plan

The production plan is discussed in this chapter. The plan is split up in the manufacturing and production locations. The manufacturing breakdown is discussed in section 10.1 and the production location is discussed in section 10.2.

10.1. Manufacturing

The production plan is in Figure 10.1. The production plan is broken down in three stages. Part manufacturing, subsystem Assembly and final assembly. In the part manufacturing, raw materials will be processed into parts. This stage of manufacturing can be done in parallel and even on different locations. In subsystem assembly the various parts parts from the previous stage are put together. For example the valves, pumps, insulation layers, baffles pipes and structural layers are put together to make the hydrogen fuel tank. As with the previous step this step can also be done parallel and at different locations. At the final step all the different subsystems are put together to form the final aircraft. This step has to be done at one location. In Figure 10.1 it can be seen how the different steps connect for each subsystem. For the subsystems, the engines will be produced at a different company, like Rolls Royce, GE or Pratt & Whitney. These companies already have a lot of experience in engine design and production. Even in conventional design this cannot be equalled by aircraft manufacturers.

In the manufacturing timing is of paramount importance. If one subsystem assembly as a delay the whole final assembly of one aircraft will be delayed and also the following aircraft will be affected by this delay.

During manufacturing the crew working on the aircraft will gain experience and therefore work more efficient, which no only reduces cost, but also increases production numbers. The cost part will be explained in subsection 13.3.5. Initially it is assumed that 16 aircraft per month will be produced but this will gradually increase due to the effect of learning. This is shown in Figure 10.2. The effect of the increased production, can be found in the program time. For a constant rate of 16 aircraft per month it would take 250 months to produce 4000 aircraft, which corresponds to 20 years and 10 months. With the learning effect the total production take 184 months which is 15 years and 4 months. Which means that 5.5 years can be won by the learning effect.

10.2. Production locations

A location for the final assembly has not been determined yet. India could be a viable option since this is one of the target markets [3]. Europe and north America could also be options, since a lot of aircraft knowledge and experience is already available from companies like Airbus, Boeing and companies affiliated with those.In addition, especially in the US and Germany a lot of investment is already done to increase the knowledge and experience in the use of hydrogen [67].

The manufacturing of the various parts and different subsystems can be done at different locations in different countries or even continents. This can be done to omit trade barriers or gain regional support and funding.

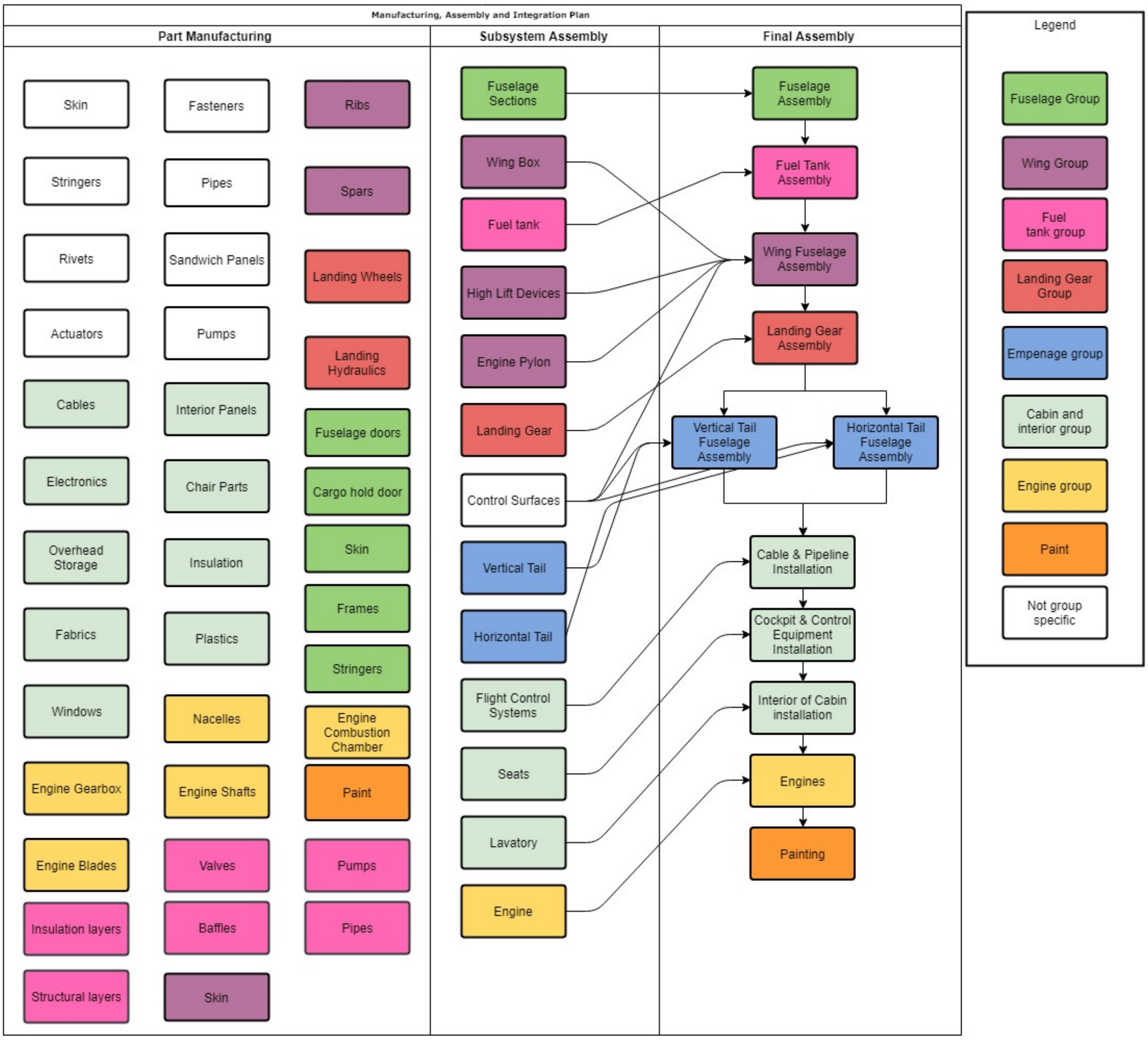

Figure 10.1: Production plan for blended wing aircraft body with open rotor and hydrogen fuel tank

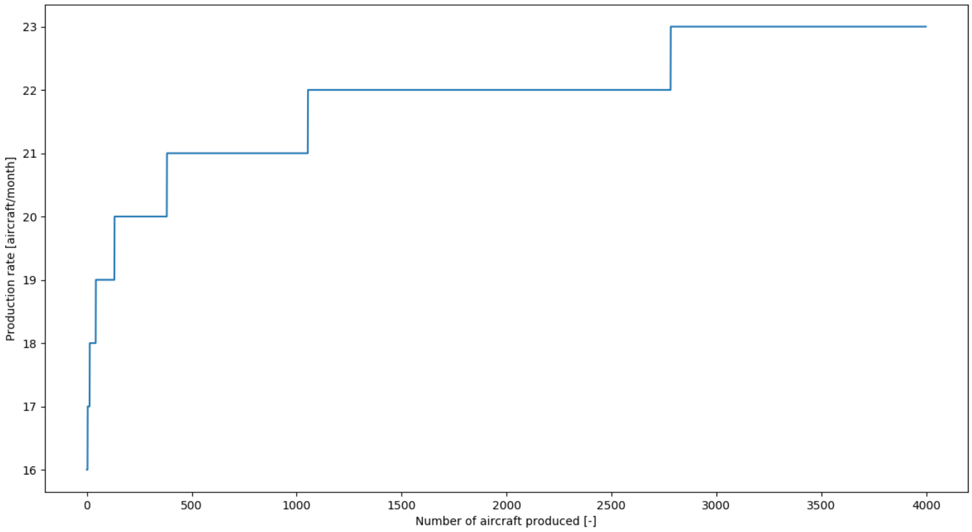

Figure 10.2: The production rate showing the effect of learning.

11

Operations & Logistics

In this chapter the operations and logistics for the HYDRA will be discussed. Operations consists of the tasks needed to operate the aircraft, which is discussed in section 11.1. Logistics consists of the measures to get everything to the aircraft to make it operable. This is from refueling to getting passengers and their luggage into the aircraft. Logistics including the transport of fuel is discussed in section 11.2.

11.1. Operations

Characteristics that make the HYDRA different in terms of operation compared to conventional aircraft is the different seating configuration, hydrogen tank and wider cargo department.

Although the seating configuration is 3-6-3 compared to the 3-3 in an A320, this is not expected to significantly increase the time needed to load and unload the passengers.

A single HYDRA requires about 70000 liters of hydrogen compared to 27000 liters for an A320. Additionally, it has been shown in Chapter 9 that the fuelling rate in liters is 3 times higher than an A320. This requires more fuelling trucks pumping at a higher rate. Current larger airports use pipelines to fuel their aircraft. These pipelines are usually made out of steel just like the pipes used to get the fuel to the airport and are not suitable for transporting hydrogen. This means that these existing pipelines have to be renewed to similar pipelines used for transporting natural gas.

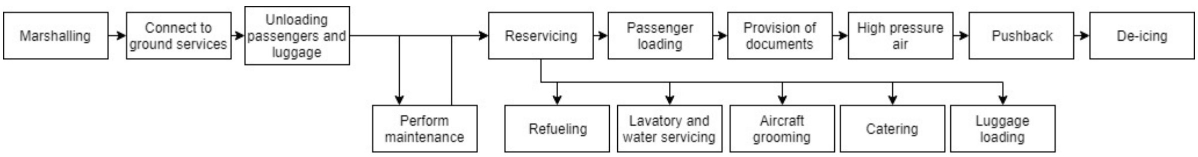

Figure 11.1: Aircraft ground operations.

Although the HYDRA has a wider cargo compartment, the containers are still the same as conventional aircraft. The cargo compartment also has similar placement, below the passengers accessible by a door. It therefore expected that the cargo loading and unloading will take the same time as an A320 or equivalent.

11.2. Logistics

Currently airports get their fuel either directly by pipeline or by the use of trucks, marine vessels and trains. Airport also have local storage tanks for the fuel that act as a buffer. Existing pipelines for jet fuel cannot be used to transport hydrogen as they are made of steel, a metal that is not resistant to hydrogen. In some countries such as France, Belgium, Germany and The Netherlands a 1300km hydrogen pipeline network is already available [16]. Hydrogen can however also be produced locally at the airport by using electrolysis which can be done with existing electrical and water infrastructure. Although fresh water methods are more efficient and less difficult, electrolysis and photocatalytic methods for extracting hydrogen from saltwater are also possible for places where fresh water may be scarce [25]. In the market analysis [1], it is stated that south and southeast Asia are targets for the aircraft. India already researched in hydrogen infrastructure for transportation purposes. They planned to have test facilities for refueling available by 2020 [37]. Also, Japan, South-Korea and China are investing in hydrogen as a fossil fuel replacement [45].

12

Sustainable Development Strategy

This chapter discusses the sustainable development strategy followed by the design team throughout the entire process. Sustainability is considered throughout various parts of the development and operation of the HYDRA.

12.1. Emissions during flight

One of the key factors to consider when examining the sustainability during operations is the emissions of the aircraft. As hydrogen has been chosen as the fuel type three different gaseous emissions are relevant namely, H_2O, CO_2 and NO_x. In addition to these emissions, noise emission is also considered as this has become increasingly important for regulators.

$\mathbf{H_2O}$

A by-product of hydrogen combustion is H_2O, although not commonly seen as a pollutant, emitting water vapour at high altitude does contribute to the greenhouse effect. The water vapour traps heat in the atmosphere increasing the heat and in effect contributing to global warming. Although this can be seen as a predominantly adverse effect the residence time of H_2O is about 6-12 days, which is much shorter than the 100 year residence time of CO_2 which is the predominant emission in kerosene fueled engines[64]. In this regard, the emission of water vapour due to hydrogen combustion is still seen as a significant step forward due to the greatly reduced residence time.

$\mathbf{CO_2}$

In traditional kerosene combustion CO_2 is one of the primary by-products that have enhanced the greenhouse effect and thus contributed to global warming. As the combustion of hydrogen produces no CO_2 this is another major advantage compared to current aircraft which utilize kerosene and thus emit CO_2

$\mathbf{NO_x}$

During flight the primary drawback of using hydrogen is the increased emission of nitrous oxides, NO_x. NO_x has been known to cause depletion of the ozone layer [44] as well as contributes to global warming. The primary reason for the NO_x emission is the greater burn temperature compared to kerosene. Increasing the burn temperature has been directly correlated to an increase in NO_x emissions [64]. The NO_x emissions can be reduced by decreasing the burn temperature, due to the cryogenic storage of the hydrogen fuel entering the combustion chamber is much colder than kerosene which aids in reducing the NO_x emission. In addition, a leaner fuel mixture also reduces the amount of NO_x emitted. Compared to kerosene, hydrogen can consistently burn in a leaner condition however this can affect engine performance. Something that has not been investigated at this stage of the design is the a concept called micro-mix combustion, which is a combustion process that produces less NO_x emission compared to kerosene combustion[48]. This works by increasing the number of local small mixing zones involving "thousands" of flames that increase the mixing intensity. As promising as this technology sounds further research in the detailed design phase will be required to assess its feasibility to this design. Ultimately, a middle ground between minimizing the NO_x emissions and achieving the required engine performance must be found.

Noise

One of the primary concerns with open rotor engines, that have been selected for HYDRA, is the noise emitted by these engines. At this stage in the design the noise generated by the engines has not been examined in detail. However, research has shown that with the use of CFD tools open rotor engines have shown significant reduction in noise. The reason for the improvements in noise level is due to the fact that CFD allows for better modelling of complex flows such as the tip vortices around the fan blades. This also allows for better optimization with regards to noise when designing the open rotor fan blades. The tools have allowed the engine to meet current noise regulation and are expected future regulations whilst maintaining the efficiency improvement compared to the CFM56 turbofan engines [12].

12.2. Hydrogen production

The type of hydrogen production will be a crucial aspect in the sustainability of the HYDRA, currently 97% of hydrogen is produced from natural gas, the remaining 3% is hydrogen produced using electrolysis. From an economic perspective it is currently much more profitable to produce hydrogen from fossil fuels, such as natural gas [33]. However, as the world moves towards adopting more renewable energy sources such as wind and solar the price of electrolysis may come down. It is hoped that this would shift hydrogen production away from the steam forming method that uses fossil fuels and instead favor electrolysis as the primary means to producing hydrogen.

12.3. End-of-life

Another important aspect that must be considered when assessing the sustainability of an aircraft is the disposal or repurposing of an aircraft at its end-of-life. As materials must be extracted from the earth an effort must be made to recycle and reuse materials in order to become truly sustainable as these finite resources will eventually run out. In recent years, as the number of new aircraft has increased, more old aircraft have been taken out of service. This has also helped drive an increase in the amount of material in an aircraft that can be recycled. Around ten years ago only about 50% of an aircraft could be recycled, however over the past decade much progress has been made up to the point that approximately 90% of the aircraft can be recycled[30].

As explained in Chapter 5 the aircraft frame is predominantly made out of aluminum. From a sustainability perspective this is largely positive as aluminum can be recycled relatively easily. The largest aircraft manufacturers have pushed carbon fiber reinforced polymers or other composite materials as the future with the entry into service of the Boeing 787 and Airbus A350. However, what they fail to address is the fact that these materials are notoriously difficult to recycle or even dispose of easily[30].

Besides the reuse of the airframe other key aspects to consider at the end-of-life are the engines, fuel tanks and interior of the aircraft. The engines need to be developed almost from the ground up as they are a new technology that until now has only been tested but largely unproven in commercial use. Currently, engines are typically removed from the aircraft and installed on another aircraft or taken apart and used for spare parts [14]. This strategy is likely most suitable for HYDRA as well, engines require frequent maintenance and replacement of parts thus there is demand for these parts. The only requirement for reusing engines and its parts is that they must be certified before being installed on another aircraft.

Not all parts of the aircraft can be recycled or reused easily; the fuel tanks for example are made up of several materials, see subsection 6.2.1. Recycling the tanks at the end-of-life will be difficult as first the materials would need to be separated first and then if possible be repurposed. Requiring these fuel tanks for liquid hydrogen storage is a drawback for sustainability in terms of repurposing the tanks however the use of hydrogen has reduced the emissions of the aircraft. Hence, on the whole the net effect is positive as using hydrogen has contributed to significant emission reduction as explained in section 12.1.

13

Market Analysis and Cost

In this chapter the market analysis will be presented. The analysis done in the baseline will be reviewed in section 13.1. In section 13.2 the analysis of the market will be given in which the HYDRA has to operate. In section 13.3 the cost analysis will be shown.

13.1. Review of baseline

In the baseline the first market analysis was done. The goal of that research was to analyze the size of the market, by looking at the expected production volume and the value attached to the numbers for the class HYDRA is supposed to compete in. Furthermore the opportunities of future markets were analyzed, in order to find out how the markets on different continents work and to find where largest growth could occur. At last the fuel price was also analyzed, due to the already existing possibility for a hydrogen powered design the kerosene fuel price was analyzed, to see how operational cost would increase over time due to increasing fuel price.

13.1.1. Future market

The main part of the baseline market analysis was the analysis of the market during the period of 2016-2036. It was set up to find a justification for an extra single aisle aircraft in the market that is dominated by Boeing[10] and Airbus[56]. In Table 13.1 the predictions done by Boeing and Airbus are shown for the period 2016-36. The unit costs was calculated by dividing the expected value by the expected volume. From the data it can be seen that both parties differ in the numbers, but the general trend in both data sets is that more than twenty thousand aircraft will be produced.

Table 13.1: Estimates for the single aisle market by Boeing and Airbus aircraft by 2016-2036

	Airbus	Boeing
Expected value [$\$10^{12}$] (FY 17)	2.38	3.18
Global Estimated Volume [-]	24810	29530
Unit cost [$\$10^{6}$] (FY 17)	133	99

Emerging markets were analyzed to find out where opportunities arise for HYDRA. It was found that the North American market and European market are already developed and will see some growth but most deliveries will be for fleet replacements. The emerging markets were found Asia, especially India, as the Indian market is the fastest growing market in the world currently. Further it was found that the Indonesian market is developing fast as well large orders from low cost airlines operating in both countries have been placed for single aisle aircraft.

An entry into service date was also set. The date was determined to be in 2030, with the reasoning being that the new aircraft can still take part in the growth of the coming 20 years and that it can start to replace some of the earlier production numbers of the current generation aircraft.

13.2. HYDRA on the market

HYDRA will provide a totally new platform on the market by 2030, with hydrogen used as the fuel for the aircraft this would be large innovation in the whole aviation market since kerosene has been used since the 1950's. The platform would provide a solution to finite fossil fuel resources, and will provoke a period of transition. Therefore the use in the early years, destinations could be limited, but will likely increase if the transition to hydrogen will be made. The main idea for HYDRA is to create an aircraft which is energy efficient over the total lifetime. This is achieved by reducing the energy used during operations as cruise was found to be the most energy intensive phase of an aircraft operational life. After analyzing the parameters that affect this efficiency it was found that switching to hydrogen would reduce the energy usage significantly. With fuel reserves running out, an approach should be taken to allow a change of energy source, the HYDRA provides an alternative to flight on kerosene. The aim is to achieve a market share of 15%, which results in 4000 aircraft sold.

HYDRA will enter the market when all of the aircraft that are produced are kerosene powered aircraft. It will use part of the growth of the market, which was shown in subsection 13.1.1. This will be from the entry into service in 2030 until 2035. After which the market will potentially grow further, but most of the sales will be replacement of older models from competitors.

13.3. Cost

In the baseline report a cost estimation was performed, this section will review the results from the baseline and will provide a cost analysis based on the same method only with more detailed input values which would provide a increased accuracy, compared to the cost estimation of the midterm. The cost estimation followed the Roskam method [52]. The total cost of the aircraft is divided into three sub costs: Development cost, manufacturing cost and the operational cost. For every group the results for the A320 are also included, which acts as an baseline.

13.3.1. Development Cost

According to Roskam the development cost includes the research, design, testing and evaluation cost (RDTE). Roskam's method, is based on statistical data of aircraft, labor hours, and statistical data on the cost of labor. The full method is explained further in this chapter. Important note is that the inputs are all in imperial units. The results of the calculations are shown in Table 13.2.

The first step is to find the so-called aeronautical manufacturing planning report weight, which is found using statistical data of previous aircraft:

$$W_{ampr} = 10^{0.1936+0.8645log(MTOW)} \tag{13.1}$$

The maximum airspeed, V_{max} is taken as the cruise speed for commercial aircraft, which for Mach = 0.7 at sea level (obtaining equivalent airspeed in knots) is 219.3 kts. The number of prototype aircraft; N_{rdte} is taken to be 7. The RDTE production rate per month is taken to be 0.33, which is industry standard. The number of engines; N_e is taken to be 2. The unconventionality factor (F_{diff}) is based on the conventionality of the design and ranges from 0.8 to 2.0. In the midterm the cost analysis was done for the configuration at that time; the Hybrid Blended Wing Body (HBWB). The unconventionality factor that was applied for that concept was 2.0 due to the very unconventional factor of the design. The same value of 2.0 will be used for the BWB design. The use of computer aided design (CAD) software a similar factor should be taken. Because both the HBWB and the BWB are very unconventional and CAD is extensively used nowadays in aircraft design the lowest factor of 0.8 is taken. Since the method by Roskam was published in the past a Cost Elevation Factor (CEF) was also determined. This factor is needed because the cost of production has increased since the method was published. According to the trend in Roskam the CEF equals 7. The CEF will mainly be used in the calculation on labor cost. Using the CEF, the engineering cost per hour, manufacturing labor cost per hour, and tooling cost per hour could be calculated by comparing the cost with the cost in 1982. The equation used was:

$$Cost_{current} = \frac{CEF}{3.02} \cdot cost_{1982} \tag{13.2}$$

The cost for engineering, manufacturing, and tooling were \$62, \$34.44, and \$45 respectively in 1982. The 3.02 represents the CEF of 1982. This resulted in an engineering cost per hour of \$143.7, \$79.8, \$99.8 in 2017.

To calculate the total engineering man-hours:

$$MHR_{aed_r} = 0.0396 W_{ampr}^{0.791} V_{max}^{1.526} N_{rdte}^{0.183} F_{diff} F_{cad} \tag{13.3}$$

To calculate the total manufacturing man-hours:

$$MHR_{man_r} = 28.984 W_{ampr}^{0.74} V_{max}^{0.543} N_{rdte}^{0.524} F_{diff} \tag{13.4}$$

To calculate the total tooling man-hours:

$$MHR_{tool_r} = 4.0127 W_{ampr}^{0.764} V_{max}^{0.899} N_{rdte}^{0.178} N_{r_r}^{0.066} F_{diff} \tag{13.5}$$

Multiplying these hours with the labor cost per hour, the total engineering labor, manufacturing labor and tooling labor costs are obtained.

Development and support testing cost is given as:

$$C_{dstr} = 0.008325 W_{ampr}^{0.873} V_{max}^{1.89} N_{rdte}^{0.346} F_{diff} CEF \tag{13.6}$$

The manufacturing material cost for the test airplane is obtained as:

$$C_{mat_r} = 37.632 F_{mat} W_{ampr}^{0.689} V_{max}^{0.624} N_{rdte}^{0.792} CEF \tag{13.7}$$

The quality control cost is taken to be 13% of the manufacturing labor cost.

The flight test airplane cost is:

$$C_{fto_r} = 0.001244 W_{ampr}^{1.16} V_{max}^{1.371} (N_{rdte} - N_{st})^{1.281} CEF F_{diff} \tag{13.8}$$

The cost for the necessary test and simulation facilities were estimated at 15% in the midterm. This will be the same for HYDRA as the new aircraft design will likely require new test and simulation facilities. Finally, both the cost of financing the entire RDTE phase as well as a profit margin on this phase are estimated at 10%.

Table 13.2: Development cost breakdown for each concept in million US Dollars

Cost components [\$ million]	Phase		
	Midterm	Final	A320
Engineering cost	223.0	286.7	128.75
Development and support testing	66.8	89.1	36.5
Engine and avionics	101.9	109.4	34.4
Manufacturing labor	638.5	774.0	287.3
Material cost for test aircraft	154.0	132.4	84.61
Tooling cost	461.1	571.7	257.5
Quality control cost	83.0	100.6	37.3
Flight test airplane cost	52.0	72.1	11.1
Test/simulation facilities cost	410.9	305.2	125.4
Financing cost	273.9	305.2	125.4
RDTE profit	52.0	305.2	125.4
Total cost of RDTE [\$ billion]	**2.739**	**3,502**	**1,254**

Table 13.3: Estimated unit price for the aircraft.

Concept	Aircraft estimated unit price [$ million]
Midterm	36.5
Final	42.0
A320	30.3

13.3.2. Manufacturing Cost

After developing the development cost, the manufacturing cost were determined. To start the estimation for the manufacturing cost, the number of aircraft produced was estimated. It was assumed that a market share of around 15% was attained. From Table 13.1 this would be around 4000 aircraft. Further more the number of aircraft produced was estimated to be 16 per month, this is a very conservative estimate as competitors produce around 60 aircraft per month for the same class [1]. This conservative estimate because the competitors have many years of experience, whereas the teams building the HYDRA has limited experience and will be building a whole new concept. Not only because it is a brand new aircraft, it is also a very unconventional one. The method used to estimate the manufacturing cost was based on statistical relations used to estimate the number of man hours for tooling and manufacturing over the entire production program, the cost per man hour for the various aspects are presented in subsection 13.3.1. Material cost was estimated using Equation 13.7, where N is now equal to the number of aircraft produced. Again a profit margin of 10% was taken to arrive at an estimated unit price per aircraft. The final estimated aircraft unit prices are presented in Table 13.3.

13.3.3. Operating Cost

After determining the development and manufacturing cost, the operational costs were determined. In general the operational costs are different for different airlines. Therefore a general aspect was analyzed which changes the cost on a similar level for all airlines, namely the fuel cost. The fuel cost itself is a large cost factor in an airlines operational cost. Since it is very hard to predict the fuel price, since it is easily affected by political unrest in oil producing countries, two scenarios were considered. The baseline scenario assumes the price of $113 per barrel and a liquid hydrogen price of $7.8 per kg. The optimistic scenario would see a strong increase in price of kerosene, to the level it would cost $186 per barrel. This scenario further sees an decrease in the price of hydrogen to $3.3 per kg[7, 15]. Although it should be noted that the cheapest method for the hydrogen production is used, which is centralized gas reforming. This process still produces CO_2, while electrolysis would produce no CO_2 but is the more expensive option at this time.

The baseline cost scenario is displayed in Table 13.4. It can be seen that in the baseline scenario the A320 is cheaper than the HYDRA, by 300 million dollar. Furthermore it can be seen that total life cycle cost for one aircraft increased drastically in the final phase. Then also the optimistic scenario was analyzed, the results are shown in Table 13.5. It is clear that the HYDRA will be cheaper than the A320 by 350 million dollar, furthermore it can be seen that the increase in the total life cycle price is lower when moving from midterm to final, as compared to the baseline scenario. A summary of the costs is given in Table 13.6. The cost of each sub group is included, and the total sum of all the costs is given.

13.3.4. Verification

Since the same method was used as in the midterm phase, verification procedure of the method remains the same as in the midterm phase. The method to determine cost was that followed by Roskam. Verification of the method was performed by implementing the values for the example aircraft in Roskam into the calculator and comparing with the values obtained by Roskam. Upon comparison, it was determined that all costs were within a 1% margin with Roskam, with the difference due to use of rounding throughout by Roskam.

[1] URL `https://www.bloomberg.com/news/articles/2018-02-06/airbus-mulls-raising-output-of-a320-family-jets-as-demand-soars` [cited 25 June 2018].

Table 13.4: Baseline cost scenario

Cost factor	Midterm	Final	A320	units
Total lifecycle cost	868,135,488	1,202,649,445	936,274,560	$
Direct operating cost	23.3	25.95	20.26	$/nm
Indirect operating cost	11.6	12.98	10.1	$/nm
Total operating cost	34.9	38.93	30.4	$/nm
Operating cost block hour	8,563	11889.94	9,281	$/blhr
Aircraft fuel lifecycle cost	168,341,598	344,979,389	271,473,578	$/AC
Percent fuel cost	19.4%	28.7%	29.0%	-
Estimated unit price	36,530,855	41,969,813	30,268,460	$/AC

Table 13.5: Optimistic cost scenario

Cost factor	Midterm	Final	A320	units
Total lifecycle cost	707,148,741	872,596,239	1,226,230,518	$
Direct operating cost	18.7	18.57	26.7	$/nm
Indirect operating cost	9.4	9.29	13.4	$/nm
Total operating cost	28.1	27.85	40.1	$/nm
Operating cost block hour	6,894	8508.89	12251	$/blhr
Aircraft fuel lifecycle cost	70,928,790	145,353,085	446,850,315	$/AC
Percent fuel cost	10.0%	16.7%	36.4%	-
Estimated unit price	36,530,855	41,969,813	29,498,632	30,268,460$/AC

Table 13.6: Total lifecycle cost

Cost factor	Midterm	Final	A320	units
Total RDTE cost	2,739,102,992	3,051,513,373	1,253,545,542	$
Manufacturing cost	37,415,454	37,460,850	27,374,333	$/AC
Total operating cost (Baseline)	34.9	38.93	30.4	$/nm
Total operating cost (Optimistic)	28.1	27.85	40.1	$/nm
Total lifecycle cost (Baseline)	868,135,488	1,202,649,445	936,274,560	$
Total lifecycle cost (Optimistic)	707,148,741	872,596,239	1,226,230,518	$
Estimated unit price	36,530,855	41,969,813	30,268,460	$/ac

Table 13.7: Return on Investment

Scenario	Midterm	Final	A320
Baseline	-7.3	0.81	13.1
optimistic	9.6	1.16	-5.1

13.3.5. Return on Investment

The return on investment (ROI) was determined using the Roskam method [52]. The return on investment for the airline is the difference between the investment made by acquisition of the aircraft, operational cost incurred during lifetime and the revenue made through transportation of payload. The ROI was calculated using the following assumptions: All the tickets are sold at the same price, the aircraft is flown at design range of 6200 km, which would result in ticket prices of \$575 and economy class. The aircraft can hold 170 passengers in a single class configuration. From the manufacturing cost and operational cost; described in subsection 13.3.2 and subsection 13.3.3, the IOC, DOC, AEP, V_{bl} and $U_{ann_{bl}}$ were obtained. Furthermore taxes should be included. Two types of taxes are applied: the investment tax credit rate, tx_{inv} and the income tax rate, tx_{rev}. The percentages for both taxes are taken to be 10% and 20% respectively. The results for the ROI calculation are shown in Table 13.7.

$$ROI = \frac{(Rev - IOC - DOC)V_{bl}}{(AEP)(1 - tx_{inv})}(1 - tx_{rev})U_{ann_{bl}} \tag{13.9}$$

From the manufacturing cost and RDTE cost the total program cost for the company was analyzed.

$$C_{prog} = C_{RDTE} + C_{man} \tag{13.10}$$

Equation 13.10 shows how the total program cost was determined. Which is based on the total RDTE cost and the total manufacturing cost. This results in the total program cost being \$152,894,915,443. When taking the estimated unit price an multiply this with the units sold the revenue accounts to \$168,000,000,000. Which gives a profit of \$15,105,084,556. This is shown in Figure 13.1, in the revenue lines and the cost line for no learning curve. Usually during the manufacturing of the aircraft the workers become more experienced, which cuts down the production time. This reduces the cost and increases the production rate of the aircraft. The learning curve was implementing using the following equation:

$$E_N = K \cdot N^s \tag{13.11}$$

Where E_N represents the effort needed for the N^{th} aircraft, K is the effort for the first aircraft, N is the number of aircraft produced and s represents the learning factor, which is negative for a learning process. In this case the effort directly translates to cost. For determining s a reduction factor of 90% was taken, with the log_{10}, which results in s being -0.046.

From Figure 13.1 it can be seen that the break even point is met early on in the production phase of HYDRA. The break even point lays at the intersection with the revenue line and the cost line. For the line incorporating the effect of learning, this is met earlier than for the scenario when there is no learning. For the learning curve line the break even point lays at 264 aircraft produced. The linear line on the other hand needs 676 aircraft produced to break even.

13.4. SWOT analysis

In the baseline a SWOT analysis was presented and was updated for HYDRA. The SWOT analysis is given in Table 13.8. At the time of making the SWOT analysis for the baseline, certain design features were not clear yet, such as the fuel used. Therefore the table is colored, with green being parts that are still applicable, red being not applicable to HYDRA and cyan being HYDRA specific factors.

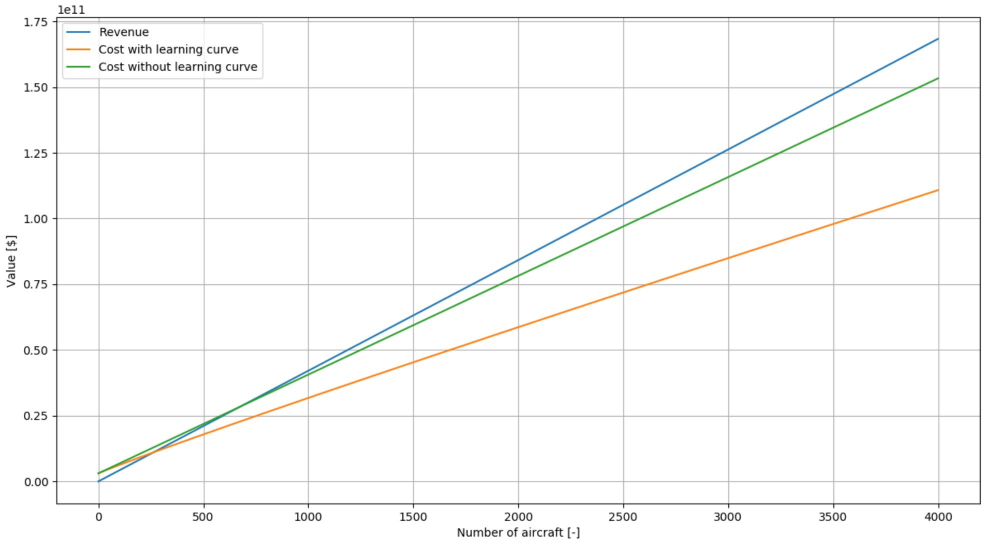

Figure 13.1: Revenue and cost

Table 13.8: SWOT analysis for the market

Strengths	**Weaknesses**
Long lifetime of product	Slow response time to market demand
Efficient aircraft	Higher unit price
No CO_2 emissions	Requires logistic change
Lighter than competitor	More challenging maintenance
Opportunities	**Threats**
Strength of emerging markets, particularly in Asia Pacific region	Financial crisis
The fact that the design is a brand new design vs. updated designs	Major incidents & terrorist attack with aircraft causing bad image and increase in regulation
Consistent growth in market	High speed rail network
Start of transition to hydrogen	Dependency on oil price
Show the feasibilty of the BWB design	Dependency on hydrogen price

13.5. Budgets

In this section a cost and mass budget is provided, for the current aircraft design, and what could be expected in the future. In Table 13.9 mass fractions for each sub group are given, both as a fraction of the MTOW and OEW.

In Table 13.10 the mass budget is given for the current phase. The contingency in the current phase is 8%, because the design is becoming more certain in this phase, as compared to the baseline report where a contingency of 20% was used, mainly because of the large uncertainties.

For the cost a budget can also be put together. The same story goes for the contingency factor that is used. From the cost determined in section 13.3 it was determined that the unit price should be 42 million US dollars. In Table 13.11 this is broken down.

Table 13.9: Ratio of each OEW sub group to MTOW (%) [22]

Subgroup	Subgroup mass percentage MTOW	Subgroup mass percentage of OEW
Wing	1.5	2.2
Fuselage	22.1	32.6
Tail	6.3	9.3
Landing gear	4.9	5.8
Total fuel system	8.0	11.8
Total Airframe structure	42.8	61.8
Engines	9.8	14.5
Systems and equipment	16.1	23.7

Table 13.10: Allocated mass budget with contingency factor

Subgroup	Wing	Fuselage	Tail	Landing gear	Propulsion	Systems and equipment	engines
Specification mass [kg]	1169	16762	4784	2982	6060	12168	7424
Target mass[kg]	1076	15421	4401	2743	5575	11195	6830
Contingency factor	0.08	0.08	0.08	0.08	0.08	0.08	0.08

Table 13.11: Allocated cost budget in million of dollars with contingency factor

Subgroup	Wing	Fuselage	Tail	Landing gear	Propulsion	Systems and equipment	final assembly	payload and cabin layout
Specification cost [$\$10^6$]	11,4	11,7	4,2	1,3	3,8	2,5	2,5	4,62
Target cost [$\$10^6$]	0,5	10,8	3,9	1,2	3,5	2,3	2,3	4,3
Contingency factor	0.08	0.08	0.08	0.08	0.08	0.08	0.08	0.08

14

Technical Risk Assessment

In this chapter, the risks associated with the design are discussed. They are evaluated using a number scale and are plotted onto a risk map for visualization. Following that, mitigation techniques are proposed and the now mitigated risks are plotted onto an updated risk map. The risk assessment appears limited due to the fact that a lot of the risks with the design were already assessed in the Midterm report [2]. A few more subsystem specific ones are observed here.

14.1. Risks

Establishing and evaluating the risks requires quantifying the probability of occurrence and the consequence should that risk occur. For the purposes of this report, the evaluation is done using educated guesses and a scale of 1 to 5. Where 1 is low probability and low consequence, while 5 is high probability and high consequence. The list of risks to be analyzed is given in Table 14.1. For the remainder of this chapter, "risk consequence" is going to be referred as "consequence" and "probability of occurrence" is going to be referred to as "probability".

Table 14.1: List of risks associated with the final design

ID	Component	Associated risk	Consequence	Probability
1	Open rotor engines	Blade failure	4	2
2	Open rotor engines	Bird strike	3	4
3	Fuel tanks	Flammability	4	2
4	Fuel tanks	Pressure loss	3	3
5	Fuel tanks	Difficult damage repair	3	2

14.2. Risk map

The risks and their probabilities and consequences from Table 14.1 are plotted onto a risk map Table 14.2. As before, the top right corner (high probability and high consequence) in red should be avoided, while the bottom left corner (low probability and low consequence) in green is favourable. Later when the risks are mitigated, they will move closer to the favourable corner.

14.3. Mitigation

In this section, mitigation techniques are presented for the risks discussed. The risks with their mitigation can be seen in Table 14.3. Additionally, the change of level in Consequence or probability is given.

Table 14.2: Risk map prior to any mitigation

5					
4			2		
3			4		
2			5	1,3	
1					
Probability / Consequence	1 (negligible)	2 (marginal)	3 (significant)	4 (critical)	5 (catastrophic)

14.4. Updated risk map

Now that the risks are mitigated in consequence and/or probability, they are plotted once again onto an updated risk map. Although the risks discussed here appear to be limited, the ones mitigated are key for the safety of the aircraft. And with time more and more risks will be added to the analysis.

Table 14.3: Technical risks and associated mitigation procedures

ID	Mitigation	Change in consequence	Change in probability
1	The failing blade cannot be contained due to the lack of nacelle and it is located close to the tail control surfaced. In order for the aircraft to be able to withstand the impact, the control surfaces will be designed with redundancy. They will be made out of several pieces with several hydraulic and electric lines so that in case of a blade strike, only a part of the component is damaged. Additionally the hydraulic and electrical lines will be rerouted away from the impact zones.	-2	0
2	The propellers will be designed to not brake off whenever bird strikes occur. The inspection intervals for the propellers will be reduced, so that any structural inadequacies can be spotted. This is done easier than a turbofan, as inspection will not require any dismantling whatsoever.	0	-2
3	The fuel tanks can be coated with a fire retardant substance on the outside to minimize the chance of a flame occurring. Additionally the fuel is extremely cold so that self combustion in case of a leak is highly unlikely.	0	-1
4	Pressure loss due to a leak can cause the hydrogen to freeze at the leak point. The consequence of that is not that high, because the freezing hydrogen may seal the leaking hole. Redundant pressure and temperature measuring devices will be put in the tank and at blow-off valves to more reliably measure the parameters such that occurrence is found as early as possible and preventative measures can be taken before critical damage occurs. (i.e. emergency landing).	0	-2
5	Repairing the damages on the hydrogen fuel tank may require fuselage disassembly. For a repair technique a hole on the fuselage skin can be cut out as a temporary access point to the damaged part of the tank. The hole can then be patched.	-1	0

Table 14.4: Risk map after mitigation

5					
4					
3					
2		1,5	2		
1			4	3	
Probability / Consequence	(negligible)	2 (marginal)	3 (significant)	4 (critical)	5 (catastrophic)

15 Functional Analysis

In this chapter a discussion regarding the functions that the aircraft shall achieve is presented. A visualization of the sequence of aircraft functions is provided in the form of a functional flow diagram (FFD), while the functions are depicted in the functional breakdown structure (FBS).

15.1. Functional Flow Diagram

The FFD is given in Figure 15.1. The FFD shows the logical order of the functions which the aircraft must perform. The functions of the aircraft are analyzed sequentially. This helps in visualizing the required actions that need to be taken by the aircraft whilst on the ground and during flight. The maintenance of the aircraft must also be considered as a functional requirement of the system. As can be seen on Figure 15.1, multiple levels of functional flows are identified. The top level starts from the operations needed before flight and flows through to the performances needed during flight and ends with operations performed after flight. Additionally, on the top level the maintenance of the aircraft and the disposal of it are depicted. All top levels (L1) are expanded (L2, L3 and L4). In the bottom right corner a legend is given for the diagram. section 15.2 restructures the functional analysis by breaking the functions down thereby ignoring the time wise distribution of the tasks.

15.2. Functional Breakdown Structure

The FBS is shown in Figure 15.2 and shows the breakdown of the various functions that the aircraft will perform. This starts at the top level and is then broken down into smaller functions. Firstly, a distinction is made between the transport of passengers and the maintenance that the aircraft must undergo. The transport of passengers is the primary function and is thus detailed most in the FBS. This was then split into pre/post-flight operations and the flight phase. The pre/post-flight operations have been broken down and result in the several functions for which requirements need to be established. For example, there might be a requirement on the time to refuel to meet a specified turn around time. The flight phase is broken down into the different flight profile phases, for each of these phases relevant aspects have been identified for which requirements will be established. Finally, the maintenance function, which has been separated from the flight phases, is detailed and 3 low level functions have been established.

15.2.1. System Flow Diagram

The system flow diagram has been given in Figure 15.3 and shows the interaction between various aircraft systems.

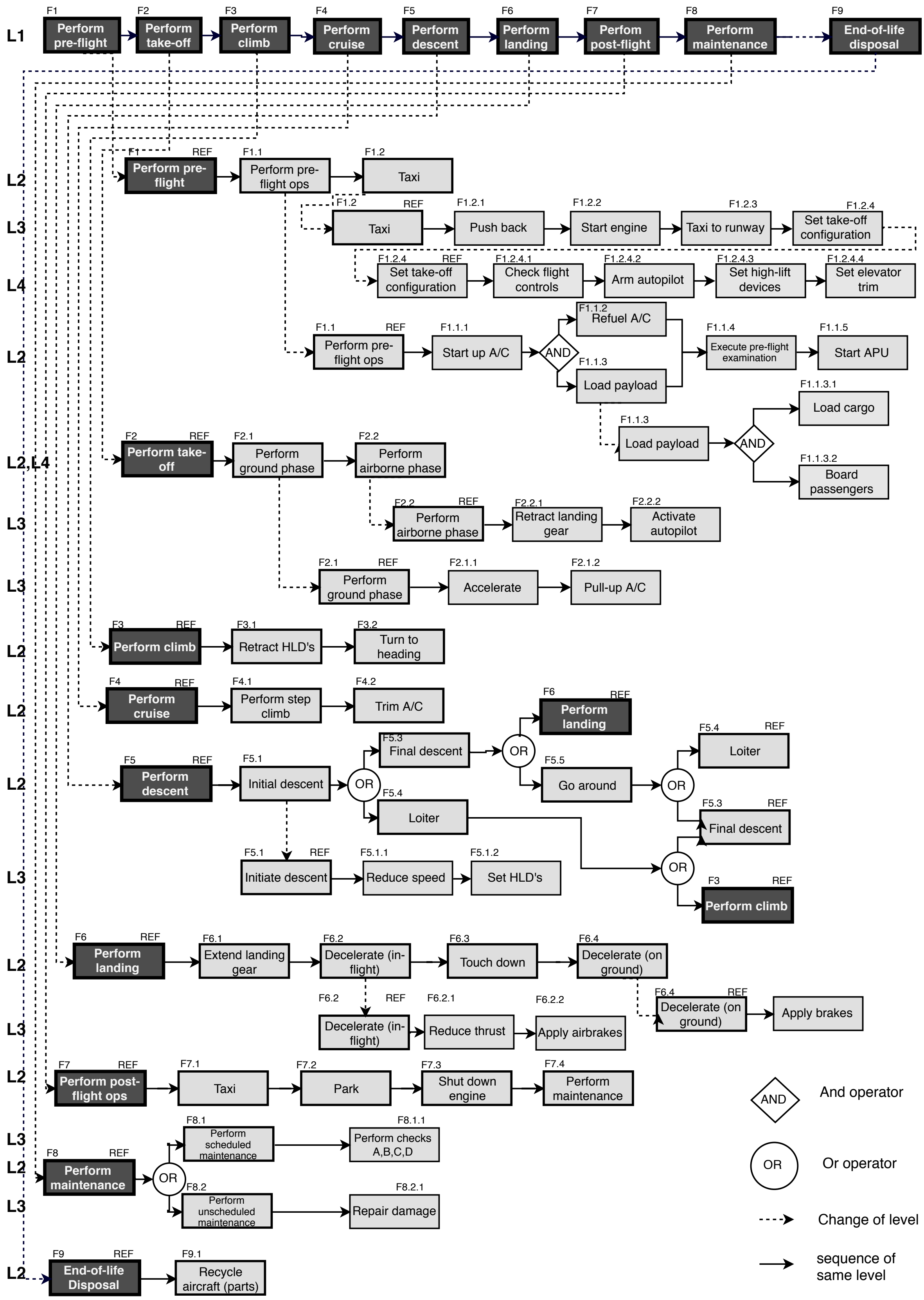

Figure 15.1: Functional Flow Diagram

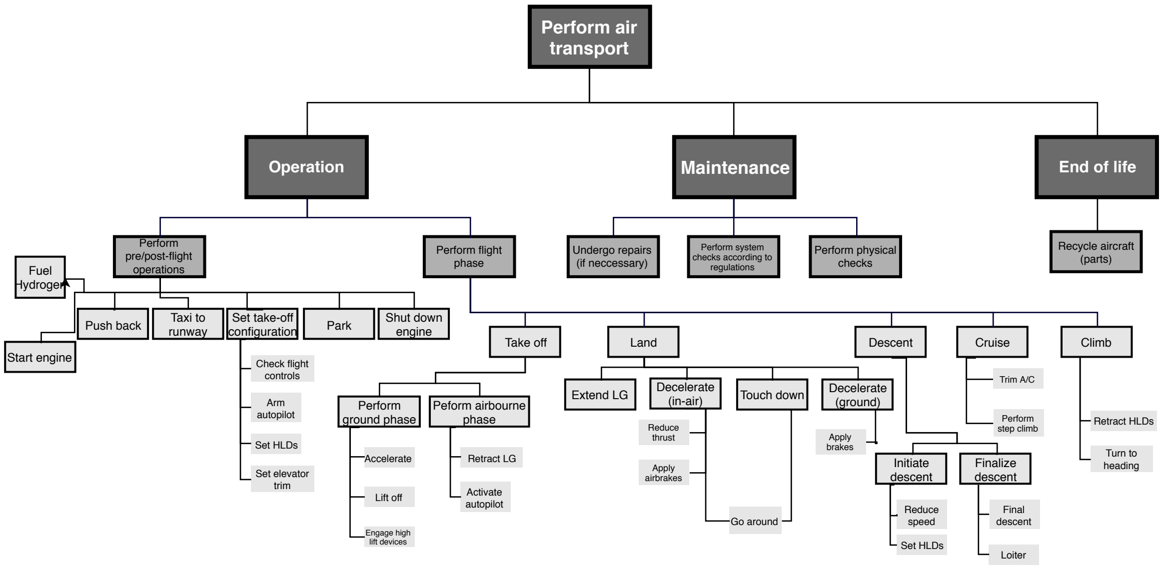

Figure 15.2: Functional Breakdown Structure

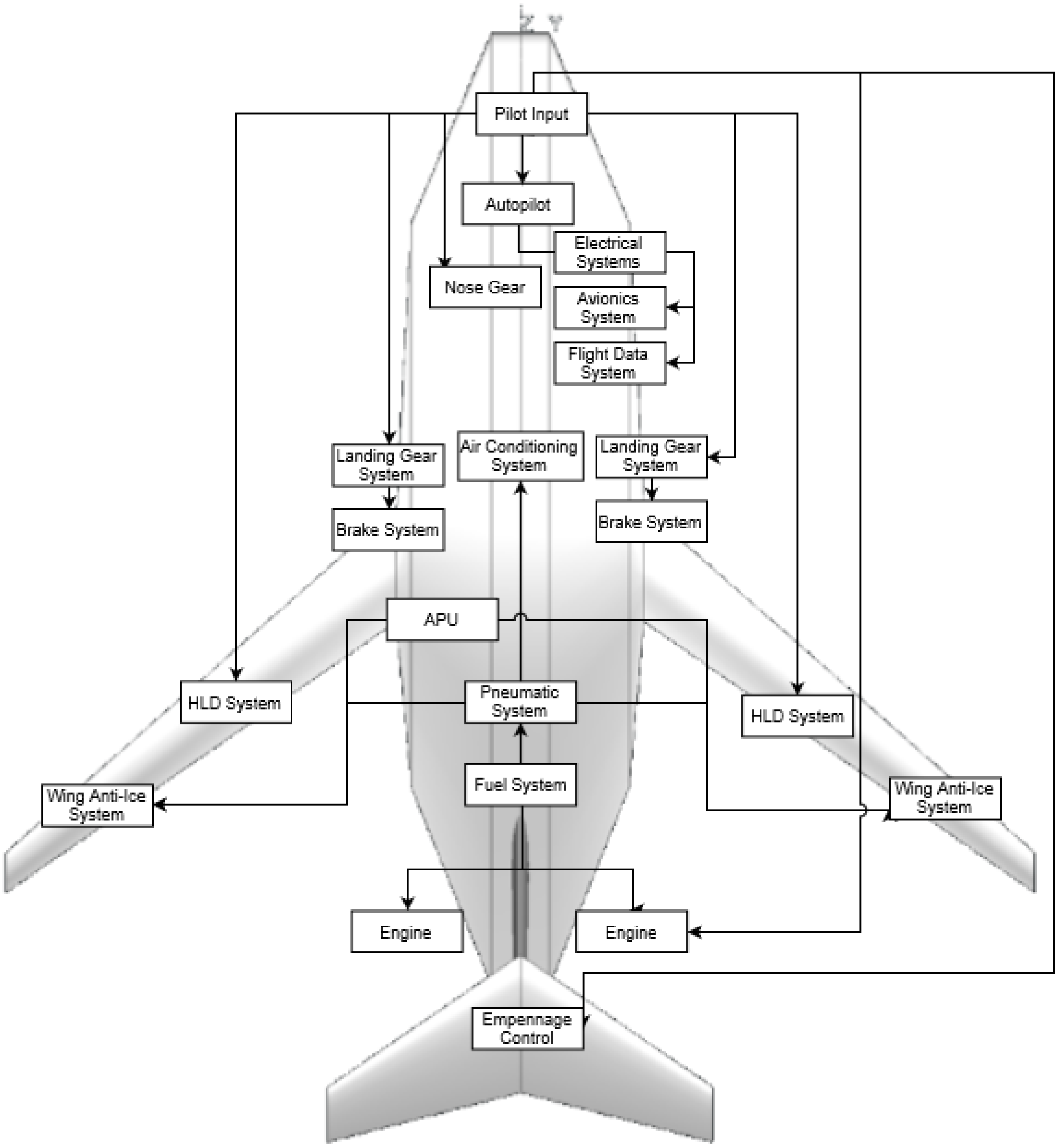

Figure 15.3: System Flow Diagram

16

Design overview

16.1. Efficiency

Improving efficiency is the leading goal of the entire project. As previously explained in [2], the efficiency is defined as the energy usage during the cruise phase E_{cruise} normalized for the number of passengers $n_{passengers}$, the number flights $n_{flights}$ and the range R. The mathematical form is

$$\frac{E_{cruise}}{n_{passengers} n_{flights} R^p} = E_{sp} a \left(\left[\frac{g}{E_{sp}} \frac{1}{\eta_{total}} \frac{C_D}{C_L} \right]_{min} c \right)^d \left(\frac{m_{fuel}}{m_{passengers}} + \frac{m_{OEW}}{m_{passengers}} + 1 \right) m_{passenger} \quad (16.1)$$

containing the specific energy for the fuel production $E_{sp_{fp}}$, the fuel mass m_{fuel}, the passenger mass $m_{passengers}$ and the structural mass m_{OEW}.

The fitting constants that allow for the normalization with respect to the range are given in Table 16.1b. Furthermore, the scaling factor c with respect to the the specific energy E_{sp}, the total propulsive efficiency η_{total} and the lift-to-drag ratio L/D is given in Table 16.1a.

Table 16.1: Efficiency equation parameters

(a) Ranging parameters

Parameter	Min	Max	Approximated range
$E_{sp}[J/kg]^1$	2e7	14e7	4e7
η_{total} [-]	0.2	0.6	0.2-0.6
$\frac{C_L}{C_D}$ [-]	15	25	15-25
c [-]	1	35	1-10

(b) Fitting constants

Constant	Value
a [-]	1.0265
d [-]	0.9475
p [-]	0.9225

The top level results together with the efficiency comparison in presented in Table 16.2. It is seen that the design is 25% more efficient than the Airbus A320.

Table 16.2: Efficiency comparison: A320 NEO vs. HYDRA

Aircraft	Range [km]	EIS	η_0 [-]	$\frac{CL}{CD}$ [-]	OEW [kg]	FW [kg]	m_{pax} [kg]	E_{sp} [J/kg]	Efficiency [J/m]
A320 NEO	5 639	2016	0.37	19.07	47000	17750	14250	4.28e7	1846
HYDRA	6 200	2030	0.40	21.50	56993	2364	16150	1.20e8	1372

Additionally, the cost conclusion as in section 13.3 suggests that a total lifecycle cost reduction of 29% is feasible.

16.2. Payload-Range diagram

In Figure 16.1, the payload-range diagram shows the possible combinations of payload and range for the aircraft. Indeed, the range requirement of 6200km is met, as that is where the economically interesting first part of the diagram ends [71].

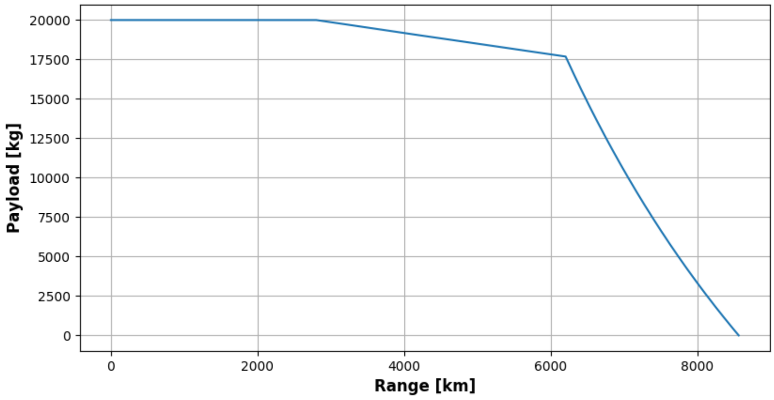

Figure 16.1: Payload-range diagram

16.3. Requirement compliance

The requirement compliance matrix is presented in Table 16.3-16.4. Requirement identifier number, text description, responsible department and status is indicated, 1 meaning a met requirement and 0 being a not verified requirement.

Table 16.3: Compliance matrix

ID	Requirement	Responsible	Status
TL1	The aircraft shall have a range of 6000 km.	FD	1
TL2	The aircraft shall be able to accommodate at least 170 passengers.	CE	1
TL3	The aircraft shall comply with the latest safety and environmental regulations.	POLS	1
TL4	The aircraft shall have a efficiency increase of 20% compared to current commercial aircraft	CE	1
TL5	The aircraft's total life cycle cost shall be 10% less than that of the current A320 and 737	CE	1
2	The aircraft shall be ETOPS-180 regulations certified.	FD, POLS	0
4	The landing gear shall be retractable.	SM	1
5	The propulsion system shall provide 202 kN of thrust at sea level.	PP	1
6	The aircraft shall have a minimum climb gradient of 3.2 percent in landing configuration.	FD	1
7	The aircraft shall have a minimum turn rate of TBD rad/s	FD	1
8	The aircraft shall have a minimum cruise speed of 0.7 Mach.	AE	1
11	The aircraft shall be able to safely withstand lightning strikes.	SM	0
12	The cabin shall be pressurized to a pressure altitude of 6000ft.	SM	1
13	The aircraft shall be able to take off, sustain flight and land with 1 engine inoperational.	FD	0
14	Maximum thrust shall be available at most 8 seconds after initial thrust application from idle.	PP	0
16	The aircraft shall be longitudinally stable during all flight phases.	FD	1

Table 16.4: Compliance matrix-continued

ID	Requirement	Responsible	Status
17	The aircraft shall be laterally stable during all flight phases.	FD	1
18	The Auxiliary Power Unit (APU) shall provide 450 W.	PP	1
20	The passenger boarding and cargo loading process shall not cause the center of gravity to exceed the tip-over limit.	FD, POLS	1
21	The aircraft shall have a minimum ground turn radius of 22.60m.	FD	0
22	The aircraft shall have emergency doors that do not need the use of the flight deck to be operable.	POLS	1
23	The emergency exits shall comply with the CS 25.807 regulations.	POLS	1
24	The aircraft shall have a maximum wing span of 36m.	AE	1
25	The aircraft doors shall fit to airport jet bridges.	POLS	1
26	The total cargo volume shall be at least 40 m^3.	POLS, SM	1
27	The aircraft shall be able to take-off on a runway length of 2500 m at standard conditions at MTOW.	FD	1
28	The noise at take-off shall not exceed 97 EPNdB according to the ICAO noise.	POLS	0
29	The aircraft shall be able to land on a runway of length 1750 m at sea level and ISA conditions and MLW	FD	1
32	At end of life 50% of the aircraft structural mass shall be recyclable/reusable.	POLS, SM	0
33	The aircraft shall be able to operate in temperatures ranging from -50 to 80 degrees Celsius.	POLS, SM	0
34	The aircraft shall be able to be evacuated in under 90 seconds with half of the emergency exits accessible.	POLS	0
35	The aircraft shall have a lifetime of 20 years.	POLS, SM	0
36	The aircraft shall meet the minimum reserve fuel requirement of carrying fuel to sustain flight for 30 minutes at 1500ft	FD	1
37	The aircraft shall have an autopilot system capable of autonomous climb, cruise, descent, landing and go-around.	POLS	0
38	In the event of a water landing, the aircraft shall stay afloat for a minimum of 10 minutes.	SM	0
39	The aircraft shall enter service in 2030.	CE	1
40	The cargo hold(s) shall be able to accommodate seven LD3-45W containers.	POLS	1
41	Take-off in airports at elevated altitudes, conditions different from sea-level.	FD	0
42	The aircraft shall have a maximum stall speed of 90 m/s.	AE	1
43	The aircraft shall have a cruise L/D of 20	AE	1
45	The aircraft shall have a CLmax of 1.3 in landing configuration	AE	1
46	The aircraft shall have a CLmax of 1.1 in take off configuration	AE	1
47	The aircraft shall have a CLmax of 0.6 in clean configuration	AE	1
48	The propulsion system shall provide .8 * MTOW [kN] of thrust at cruise	PP	1
49	The cryogenic tanks will be able to store 4670 [kg] of Liquid Hydrogen	PP	1
50	The temperature in the cryogenic tank shall remain below 20 [K]	PP	1
51	The aircraft engines shall have a SFC below 4.5 [mg/N*s]	PP	1
52	The aircraft shall be able to refuel in 16 [minutes]	PP	1
53	The engines shall be able to provide 101 [kN] reverse thrust.	PP	1
56	The wing box shall be able to withstand a maximum von Mises stress of 269.5 MPa.	SM	1
58	LH2 tanks must be able to withstand 0.4 MPa of pressure.	SM	1
59	The fuselage shall be able to be pressurized and unpressurized TBD amount of times	SM	
60	The structure shall be able to provide space for the the LH2 tank	SM	1
61	The aircraft structure shall be able to be serviced in regular maintenance or when mild impact, like bird strike, occurs.	SM	0
62	The aircraft shall be inspectable.	SM	0
68	The aircraft shall be able to land with a roll angle of 5 degrees	FD	1
69	The aircraft shall be able to land with a pitch angle of 15 degrees	FD	1

17
Future Planning

This chapter talks about the future plans of the project. Firstly, the technical design plans for the future are discussed, following from that the overall project plan on how the HYDRA shall enter into service.

17.1. Technical design

The section discusses design methods that could not be implemented during this phase of the design, but are to be implemented in the future. The reasons they were not implemented at this stage are mostly scheduling and/or lack of resources. This section is also meant as suggestions for improvement for reproducing the results obtained.

17.1.1. Aerodynamics

For future aerodynamic analysis it is suggested to examine the following:

- Verify XLFR5 results using a CFD analysis, this would allow for the initial results to be compared to further analysis and understand any discrepancies in the analysis.
- A CFD analysis would likely also allow analysis for greater angles of attack. This would aid in the understanding of when exactly the wing stalls as well as a better indication of the $C_{L_{max}}$ of the aircraft as this is currently estimated
- Model the aircraft engines such that they can be modeled for use in a CFD analysis. This will allow for a better prediction of the drag by the engine.
- Investigate and design wingtip devices to reduce the induced drag of the outer wing. This could further improve the aerodynamic efficiency of the aircraft.
- Investigation into active flow control to potentially further increase the amount of laminar flow over the aircraft. Again, the aim of adding active flow control would be to improve aerodynamic efficiency through the reduction in drag.
- Once the design has been finalized it would also be desirable to perform wind tunnel tests on the both the selected airfoils as well as the 3D wing. This is done to validate the obtained results and ensure that the expected performance is met during actual operations.

17.1.2. Structures

For future structural analysis, several aspects within scope of this project to be improved:

- Add in-flight load cases to the fuselage stringer design. For example loads from the empenage and engines
- In depth landing gear design and analysis.

- Analysis and design of windows and doors in the aircraft.
- Engine pylon design.
- Empenage structural design. Including moving parts
- HLD's and control surfaces structural design.
- Design floors in greater detail.
- Fuselage wing box integration.
- Introduce torsional loads on the wing. This will introduce shear flows in addition to the transverse loads, which will most likely increase the required number of stringers or require a mid spar to be introduced. This will require to move the lift and drag forces to act at a location given by the Aerodynamics department.
- Have the wing box non-symmetric. By doing so, the neutral axes will not be located at the symmetry planes of the wing box. This way the shear centre can be moved for better torsional stiffness w.r.t. the loads on the structure.
- Analyze types of stringers. This way different stringers can be used for the top and bottom skins. Some stringers are good at carrying tension while others are good in compression. Such design options will help optimize the structural weight of the wing box since the most optimized stringer for the load case at a certain location, which can therefore be done with less material. The method will require to go into crippling failure analysis.
- Introduce flanges on the outside of the spars. Flanges help with shear load carrying and the ones at the front spar form the leading edge shape. By introducing flanges, less ribs will be required, helping with better weight optimization as flanges weigh less.
- Analyze materials in more depth. By going fully or partially into composites may yield a better weight optimized design. However, it is important to acknowledge that such options would pose difficulties and expenses in manufacturing and maintenance.
- Analyze the weaknesses of different fastening methods (bolts, rivets, welding, etc.) imposed on the structure and choose the most optimal one. Furthermore if holes are to be drilled, analyze the hole spacing with respect to the loads of a given component.

17.1.3. Power and Propulsion

The detail of the analysis of the power and propulsion systems can be improved by taking the following considerations.

- The thermodynamic model can be made in more detail using CFD tools. This will allow for many of the assumptions to disappear as they will be modeled in the CFD tool.
- The heatflow calculations can also be calculated using CFD tools with the complete tank geometry including the pipes going in and out of the tank.
- The engine weight estimation could be improved by adding more detail by analysing the weight on a component basis.
- The sloshing barriers can be designed in more detail by moddeling the fluid and analysing the effectiveness of the barriers.
- A more detailed analysis into the power required could be made, this will improve the size and weight estimates of the APU.

17.1.4. Stability and control

- Detailed derivatives determination based on the more accurate aerodynamics analysis
- Control system analysis + control actuation

- stability change with fuel emptying during flight
- Detailed research in the empenage- body connection
- Comparison with data from wind tunnel

17.1.5. The project

This section talks about the plans for the future of the entire project. From the end of DSE to the entry into service in 2030. The entry into service is defined as the first aircraft to be delivered to a customer for which the date of 02-01-2030 is selected. The reason for this date is to leave a safety margin of a year for any delays that may occur during this phase of the project such that the entry into service date requirement can still be met. The start of this project is selected as the first Monday after DSE Symposium - 09-07-2018.

Project plan

The plan firstly incorporates the more detailed design methods described in section 17.1. The Gantt chart visualization of this plan can be seen in Figure 17.1.
Each technical department will be verifying their designs using more sophisticated methods (CFD, FEM, etc.). Additionally, validation will occur in the form of a physical model being built and tested accordingly.
Moreover, when the detailed design phase is close to completion, the subsystems interaction will be observed. This way the compatibility between the different subsystems will be established to see how the total system behaves (i.e if the aerodynamic body provides clean airflow for the engines to generate the thrust required). After the system is established, the manufacturing procedures will be developed. According to the materials to be used, different methods of manufacturing may be required (press-forming stringers vs drawing). After the manufacturing methods and procedures are established, factories need to be built or existing ones to be adjusted for the manufacturing of the HYDRA in particular. Then prototypes will be built in order to test them in flight. This way stability and control can be validated and certification can be obtained. After certifying the HYDRA, mass producing can occur to start delivering on the airliners that have ordered. Along the whole duration of the post-DSE project, the HYDRA is marketed to ensure sufficient sales and back-orders, so that delivery can start as early as possible with as many aircraft as possible on the entry into service date of 2030.

ID	Task Mode	Taaknaam	Duration	Start	Finish	Predecessors	Resource Names
1		**Market aircraft**	149 mons	Mon 09-07-18	Fri 07-12-29		
2		**Detailed subsystem design**	**2120 days**	**Mon 09-07-18**	**Fri 21-08-26**	**1SS**	
3		**Aerodynamic analysis**	**880 days**	**Mon 09-07-18**	**Fri 19-11-21**		
4		Analyze more airfoils or design an airfoil	9 mons	Mon 09-07-18	Fri 15-03-19		
5		Analyze winglets and vortex generators	6 mons	Mon 18-03-19	Fri 30-08-19	4	
6		Analyze aerodynamics of aircraft tail	9 mons	Mon 18-03-19	Fri 22-11-19	4	
7		Verify methods using CFD	8 mons	Mon 25-11-19	Fri 03-07-20	4,5,6	
8		Validate model by windtunnel testing	18 mons	Mon 06-07-20	Fri 19-11-21	7	
9		**Structural analysis**	**931 days**	**Mon 09-07-18**	**Mon 31-01-22**		
10		Analyze types of stringers	3 mons	Mon 09-07-18	Fri 28-09-18		
11		Research and analyse the full or partial use of different materials	12 mons	Mon 09-07-18	Fri 07-06-19		
12		Introduce flanges in the wing box analysis	8 mons	Mon 10-06-19	Fri 17-01-20	10,11	
13		Analyse torsion on wing box	6 mons	Mon 10-06-19	Fri 22-11-19	12SS	
14		Design floorbed	2 mons	Mon 20-01-20	Fri 13-03-20	13,12	
15		Design empennage structure	6 mons	Mon 25-11-19	Fri 08-05-20	13	
16		Design HLD mechanism structure	6 mons	Mon 25-11-19	Fri 08-05-20	15FF	
17		Analyze aeroelastic characteristics of the aircraft	8 mons	Mon 11-05-20	Fri 18-12-20	16,5,6	
18		Analyze currently neglected loads on fuselage	18 mons	Mon 09-07-18	Fri 22-11-19		
19		Size fuselage frames	3 mons	Mon 25-11-19	Fri 14-02-20	18	
20		Design engine pylons	6 mons	Mon 09-07-18	Fri 21-12-18		
21		Size landing gear	6 mons	Mon 24-12-18	Fri 07-06-19	20	
22		Perfrom iteration cycles	1 mon	Mon 11-05-20	Fri 05-06-20	16,19,21	
23		Verify methods by using FEM	6 mons	Mon 08-06-20	Fri 20-11-20	22	
24		Validate model by destructive testing	15.55 mons	Mon 23-11-20	Mon 31-01-22	23	
25		**Propulsion and power analysis**	**980 days**	**Mon 09-07-18**	**Fri 08-04-22**		
26		Generate a geometrical thermodynamic model of the fuel tanks	9 mons	Mon 09-07-18	Fri 15-03-19		
27		Perform a complete CFD analysis	12 mons	Mon 18-03-19	Fri 14-02-20	26	
28		Design fuel tank sloshing barriers	2 mons	Mon 17-02-20	Fri 10-04-20	27	
29		Design pumps and fuel lines	4 mons	Mon 17-02-20	Fri 05-06-20	28SS	
30		Analyse thermodynamics of fuel spraying into combustion chamber	6 mons	Mon 08-06-20	Fri 20-11-20	29	
31		Design engine components	24 mons	Mon 09-07-18	Fri 08-05-20		
32		Design APU	2 mons	Mon 11-05-20	Fri 03-07-20	31	
33		Build and test engines	18 mons	Mon 23-11-20	Fri 08-04-22	30,32	
34		**Stability, control and performance analysis**	**2120 days**	**Mon 09-07-18**	**Fri 21-08-26**		
35		Determine detailed derivatives	6 mons	Mon 09-07-18	Fri 21-12-18		
36		Design with control actuation details	12 mons	Mon 24-12-18	Fri 22-11-19	35	
37		Analyze fuel emptying during flight	4 mons	Mon 25-11-19	Fri 13-03-20	36	
38		Verify methods by inputting data from existing aircraft	3 mons	Mon 16-03-20	Fri 05-06-20	37	
39		Validate model with flight tests.	12 mons	Mon 22-09-25	Fri 21-08-26	50SS,38	
40		**Systems interaction**	**280 days**	**Mon 11-04-22**	**Fri 05-05-23**	**3,9,25,38**	
41		Analyze complete model in wind tunnel	8 mons	Mon 11-04-22	Fri 18-11-22		
42		Design hydraulic lines	6 mons	Mon 21-11-22	Fri 05-05-23	41	
43		Design electrical lines	4 mons	Mon 21-11-22	Fri 10-03-23	42SS	
44		**Develop manufacturing procedures**	**300 days**	**Mon 11-04-22**	**Fri 02-06-23**	**40SS**	
45		Analyze stringer manufacturing methods	6 mons	Mon 11-04-22	Fri 23-09-22		
46		Analyze thin plate, spar, rib manufacturing methods	6 mons	Mon 11-04-22	Fri 23-09-22		
47		Analyze required fasteners types and sizing (bolts,rivets, etc.)	9 mons	Mon 26-09-22	Fri 02-06-23	45,46	
48		Create or adjust factories for manufacturing	12 mons	Mon 05-06-23	Fri 03-05-24	44,40	
49		Build prototypes	18 mons	Mon 06-05-24	Fri 19-09-25	48	
50		Perform test flights	24 mons	Mon 22-09-25	Fri 23-07-27	49	
51		Certify aircraft	36 mons	Mon 22-09-25	Fri 23-06-28	50SS,39FF	
52		**Produce aircraft**	**397 days**	**Mon 26-06-28**	**Tue 01-01-30**	**51**	
53		Build fuselage	8 mons	Mon 26-06-28	Fri 02-02-29		
54		Build engines	13.75 mons	Mon 26-06-28	Fri 13-07-29		
55		Build wings	12 mons	Mon 26-06-28	Fri 25-05-29		
56		Build empennage	6 mons	Mon 26-06-28	Fri 08-12-28		
57		Part delivery and assembly	6 mons	Wed 18-07-29	Tue 01-01-30	53,54,55,56	
58		Enter into service	0 days	Wed 02-01-30	Wed 02-01-30	52,1	

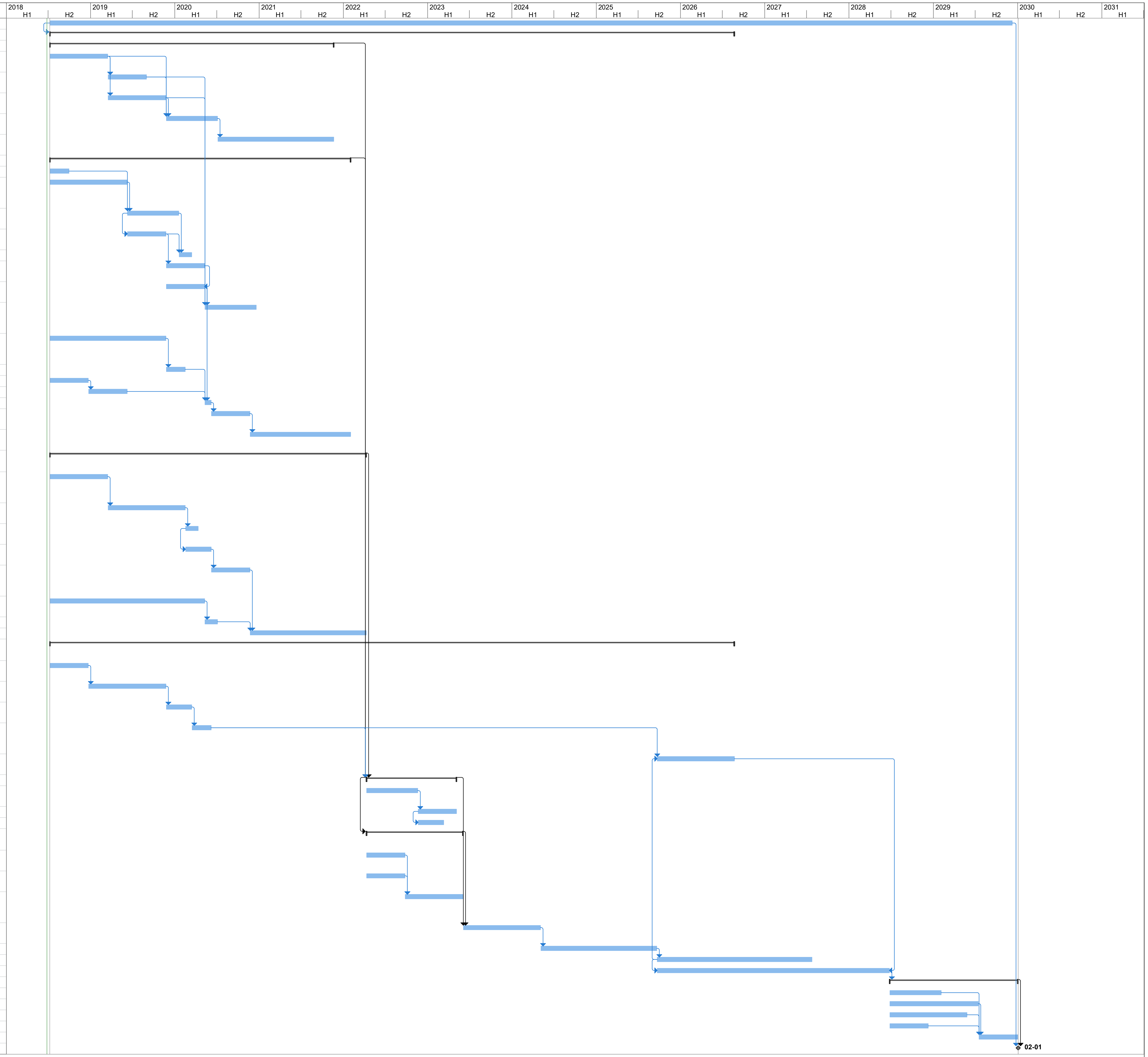

Project: msproj11
Datum: Tue 26-06-18

Taak | Splitsing | Mijlpaal | Samenvatting | Projectsamenvatting | Externe taken | Externe mijlpaal | Inactieve taken | Inactieve mijlpaal | Inactieve samenvatting | Handmatig taak | Alleen duur | Handmatige samenvatting | Handmatige samenvatting | Alleen begindatum | Alleen einddatum | Deadline | Voortgang | Manual Progress

Pagina 1

Figure 17.1: Gantt chart, describing the project plan from the end of DSE until entry into service date.

Bibliography

[1] Group 1. True high-efficiency commercial aircraft : The baseline report. Technical report, TU Delft, 2018.

[2] Group 1. True high-efficiency commercial aircraft : The midterm. Technical report, TU Delft, 2018.

[3] Group 1. True high-efficiency commercial aircraft : The project plan. Technical report, TU Delft, 2018.

[4] Elham A. Aerospace design and system engineering elements. Technical report, Delft University of Technology, 2016.

[5] I.H. Abbott and A.E. Von Doenhoff. *Theory of wing sections*. Dover Publications Inc., 1959.

[6] Federal Aviation Administration. Aviation maintenance technician handbook, 2008.

[7] J. Adolf, C.H. Balzer, A. Louis, J., U. Schabla, M. Fischedick, K. Arnold, A. Pastowski, and D. Schüwer. *Shell Hydrogen Study: Energy of the Future?*, 2017.

[8] *Aircraft Characteristics - Airport and Maintenance Planning*. Airbus, February 2018.

[9] R.C. Alderliesten. Introduction to Aerospace Engineering - Structures and Materials. Lecture reader, Delft University of Technology, 2011.

[10] Boeing Commercial Airplanes Market Analysis. *Boeing Current Market Outlook 2017-2036*. P.O. Box 3707, MC 21-28, Seattle, WA 98124-2207, 2017.

[11] John Anderson. *Fundamentals of Aerodynamics*. McGraw-Hill, 2016.

[12] S. Arif Khalid, A. Breeze-Stringfellow, T. Wood, K. Ramakrishnan, U. Paliath, J. Wojno, B. Janardan, T. Goerig, A. Opalski, and J. Barret. Open rotor aeroacoustic technology non-proprietary report. Technical report, General Electric Company, May 2013.

[13] M.T.H. Brown. Conceptual design of blended wing body airliners within a semi-automated design framework. master thesis, Delft University of Technology, May 2017.

[14] W. Carberry. Airplane recycling efforts benefit boeing operators. *Aero*, 2008.

[15] R. Conrady and M. Buck. *Trends and Issues in Global Tourism 2009*. Springer, 2009.

[16] H. Dagdougui, R. Sacile, C. Bersani, and A. Ouammi. *Hydrogen Economy, Supply Chain, Life Cycle Analysis and Energy Transition for Sustainability*. Elsevier, 125 London Wall, London EC2Y 5AS, United Kingdom, 2017.

[17] D. Daggett, O. Hadaller, R. Hendricks, and R. Walther. Alternative fuels and their potential impact on aviation. *ICAS*, 2006.

[18] A. Deperrois. About xflr5 calculations and experimental measurements, October 2009.

[19] A Deperrois. Point is out of flight envelope. XFLR5 Documentation, 2010.

[20] Tulapurkara E. Flight dynamics. Technical report, Indian Institute of Technology, 2013.

[21] *Certification Specifications for Large Aeroplanes CS-25*. EASA, September 2007.

[22] A. Elham. *Weight Indexing for Multidisciplinary Design Optimization of Lifting Surfaces*. Dissertation, Delft University of Technology, 2013.

[23] E. Gill. AE3211-I 2017/2018 SEAD Lecture 4. Lecture slides, Delft University of Technology, 2018.

[24] E. Gill. AE3211-I 2017/2018 SEAD Lecture 5. Lecture slides, Delft University of Technology, 2018.

[25] L. Guo, Z. Yang, K. Marcus, Z. Li, B. Luo, L. Zhou, X. Wang, Y. Du, and Y. Yang. *MoS2/TiO2 heterostructures as nonmetal plasmonic photocatalysts for highly efficient hydrogen evolution*, August 2017.

[26] A. Haj Ayeda, K. Kusterer, H.H.-W. Funke, J. Keinz, C. Striegan, and D. Bohn. Experimental and numerical investigations of the dry-low-nox hydrogen micromix combustion chamber of an industrial gas turbine. *Propulsion and Power Research*, 2015.

[27] E.S. Hendricks and M.T. Tong. Performance and weight estimates for an advanced open rotor engine. Technical report, NASA, 2012.

[28] Honeywell. *131-9[A] Auxiliary Power Unit*, 2008.

[29] D. Howe. Blended wing body airframe mass prediction. *Proceedings of the Institution of Mechanical Engineers, Part G: Journal of Aerospace Engineering*, 2001.

[30] International Air Transport Association (IATA). *Aircraft Recycling - The Life and Times of an Aircraft*, August 2011.

[31] F.P. Incropera, D.P. Dewitt, T.L. Bergman, and A.S. Lavine. *Fundamentals of heat and mass transfer*. JOHN WILEY & SONS, 6 edition, 2007.

[32] D. Jeong, D. Roach, J. Canha, J. Brewer, and T. Flournoy. Strain fields in boeing 737 fuselage lap splices: Field and laboratory measurements with analytical correlations. *Federal Aviation Administration*, 1995.

[33] B. Khandelwal, A. Karakurt, P.R. Sekaran, V. Sethi, and R. Singh. Hydrogen powered aircraft : The future of air transport. *Progress in Aerospace Sciences*, 60, 2013.

[34] R. Liebeck. Design of the blended wing body subsonic transport. *Journal of Aircraft*, 41, 2004.

[35] Van Dresar N.T. Lin C.S. and M.M. Hasan. Pressure control analysis of cryogenic storage systems. *Journal of Propulsion and Power*, 20(3), 2004.

[36] Z. Lyu and J.R.R.A. Martins. Aerodynamic design optimization studies of a blended-wing-body aircraft. *Journal of Aircraft*, 51, 2014.

[37] R.K. Malhotra. Report on transportation through hydrogen fuelled vehicles in india. Technical report, Ministry of New and Renewable Energy, Government of India, 2016.

[38] W.H. Mason. Analytic models for technology integration in aircraft design. Master's thesis, Virginia Polytechnic Institute and State University, 1990.

[39] A.F. Mills and Coimbra C.F.M. *Basic Heat and mass transfer*. Temporal, 3 edition, 2015.

[40] J. Mulder, W. van Staveren, J. van der Vaart, E. de Weerdt, C. de Visser, A.C. in't Veld, and E. Mooij. *Flight Dynamics*. Delft University of Technology, March 2013.

[41] J.A. Mulder, W.H.J.J. van Staveren, J.C. van der Vaart, E. de Weerdt, C.C. de Visser, A.C. in 't Veld, and E. Mooij. Flight Dynamics Lecture Notes, 24 Mar. 2013. [Online]. Available: `brightspace.tudelft.nl`. [Accessed: 21 Mar. 2018].

[42] Y.S.H. NAJJAR. Hydrogen fueled and cooled gas turbine engine. *Int. J. Hydrogen Energy*, 15(11):827–832, 1990.

[43] M.C.Y. Niu. *Airframe stress analysis and sizing*. Hong Kong Conmilit Press Ltd., Flat A, 10th Floor, Shing Loong Court, 13 Dragon Terrace, North Point HONG KONG, 1997.

[44] R.W. Portmann, J.S. Daniel, and A.R. Ravishankara. Stratospheric ozone depletion due to nitrous oxide: Influences of other gases. *Philosophical Transactions of the Royal Society B: Biological Sciences*, 2012.

[45] M. Pudukudy, Z. Yaakob, M. Mohammad, B. Narayanan, and K. Sopian. *Renewable hydrogen economy in Asia – Opportunities and challenges: An overview*, December 2013.

[46] N. Qin, A. Vavalle, and A. Le Moigne. Spanwise lift distribution for blended wing body aircraft. *American Institute of Aeronautics and Astronautics*, 2005.

[47] D. Raymer. *Aircraft Design: A Conceptual Approach.* AIAA, Washington D.C, USA, 1992.

[48] S. Rondinelli, R. Sabatini, and A. Gardi. Challenges and benefits offered by liquid hydrogen fuels in commercial aviation. Technical report, RMIT University, November 2014.

[49] J. Roskam. *Airplane design part 1: preliminary sizing of airplanes.* Roskam Aviation and Engineering Corporation, Ottowa, KS, USA, 1985.

[50] J. Roskam. *Airplane Design Part IV: Layout of Landing Gear and Systems.* Roskam Aviation and Engineering Corporation, Ottowa, KS, USA, 1985.

[51] J. Roskam. *Airplane Design Part V: Component weight estimation.* Roskam Aviation and Engineering Corporation, Ottowa, KS, USA, 1985.

[52] J. Roskam. *Airplane Design Part VIII: Airplane Cost Estimation: Design, Development, Manufacturing and Operating.* Roskam Aviation and Engineering Corporation, Ottowa, KS, USA, 1985.

[53] J. Roskam and C. Lan. *Airplane Aerodynamics and performance.* Roskam Aviation and Engineering Corporation, Ottowa, KS, USA, 1998.

[54] G. Ruijgrok. *Elements of Airplane Performance.* Delft University Press, 2004.

[55] Mohammad S. *Aircraft Design: A Systems Engineering Approach.* Wiley Publications, September 2012.

[56] Airbus S.A.S. *Global Market Forecast Growing horizons 2016/2036.* 31707 Blagnac Cedex, France, 2017.

[57] S.P. Schoensleben. Integrated trailing edge flap track mechanism for commercial aircraft. Master's thesis, Eidgenössische Technische Hochschule Zürich, 2016.

[58] D. Scholz. An optional apu for passenger aircraft. *Challenges in European aerospace*, 2015.

[59] W.G. Sewall, R.J. Mcghee, D.E. Hahne, and F.L. Jordan. Wind tunnel results of the high-speed nlf(1)-0213 airfoil, 1987.

[60] A.J. Slingerland. Development of a preliminary sizing module for conventional and unconventional aircraft. master thesis, Delft University of Technology, June 2014.

[61] D. Steenhuizen and A. Elham. Wing Design Part 3. Lecture slides, Delft University of Technology, 2015.

[62] D. Steenhuizen and A. Elham. Wing Design Part 2. Lecture slides, Delft University of Technology, 2015.

[63] M. F. Stephenson. Wing trailing edge flap mechanism, February 1991.

[64] F. Svensson, A. Hasselrot, and J. Moldanova. Reduced environmental impact by lowered cruise altitude for liquid hydrogen-fuelled aircraft. *Aerospace Science and Technology*, 8, 2004.

[65] E. Torenbeek. *Synthesis Of Subsonic Airplane Design.* Delft University Press, Delft University of Technology, The Netherlands, 1972.

[66] E. Torenbeek. *Advanced aircraft design : conceptual design, analysis, and optimization of subsonic civil airplanes.* John Wiley and Sons, Ltd., Delft University of Technology, The Netherlands, 2013.

[67] M. de Valladares. Global trends and outlook for hydrogen. *iea Hydrogen*, 2017.

[68] J. Vargas. Development of a wave drag prediction tool for the conceptual design phase. master thesis, Delft University of Technology, Jul 2015.

[69] J.K. Viken, W. Pfenninger, H.L. Morgan, and R.L. Campbell. Design of the low-speed nlf(1)-0414f and the high-speed hsnlf(1)-0213 airfoils with high-lift systems. Technical report, NASA, 1987.

[70] R. Vos, J.A. Melkert, and B.T.C. Zandbergen. Aerospace Design and Systems Engineering Elements: The design of the fuselage. Lecture slides, Delft University of Technology, 2018.

[71] R. Vos, J.A. Melkert, and B.T.C. Zandbergen. Aerospace Design and Systems Engineering Elements: Class-I weight estimation + Payload-range diagrams. Lecture slides, Delft University of Technology, 2018.

[72] R. Vos, J.A. Melkert, and B.T.C. Zandbergen. Aerospace Design and Systems Engineering Elements: A/C Preliminary Sizing (T/W-W/S diagram). Lecture slides, Delft University of Technology, 2018.

[73] L. Werfelman. Thin skinned. *Aerosafety world*, 2011.

[74] C. Winnefeld, T. Kadyk, B. Bensmann, U Krewer, and R. Hanke-Rauschenbach. Modelling and designing cryogenic hydrogen tanks for future aircraft applications. *Energies*, 2018.

[75] Matt Zagoren. *Airbus A320-232 Limitations*, 2016.

A

Drawings

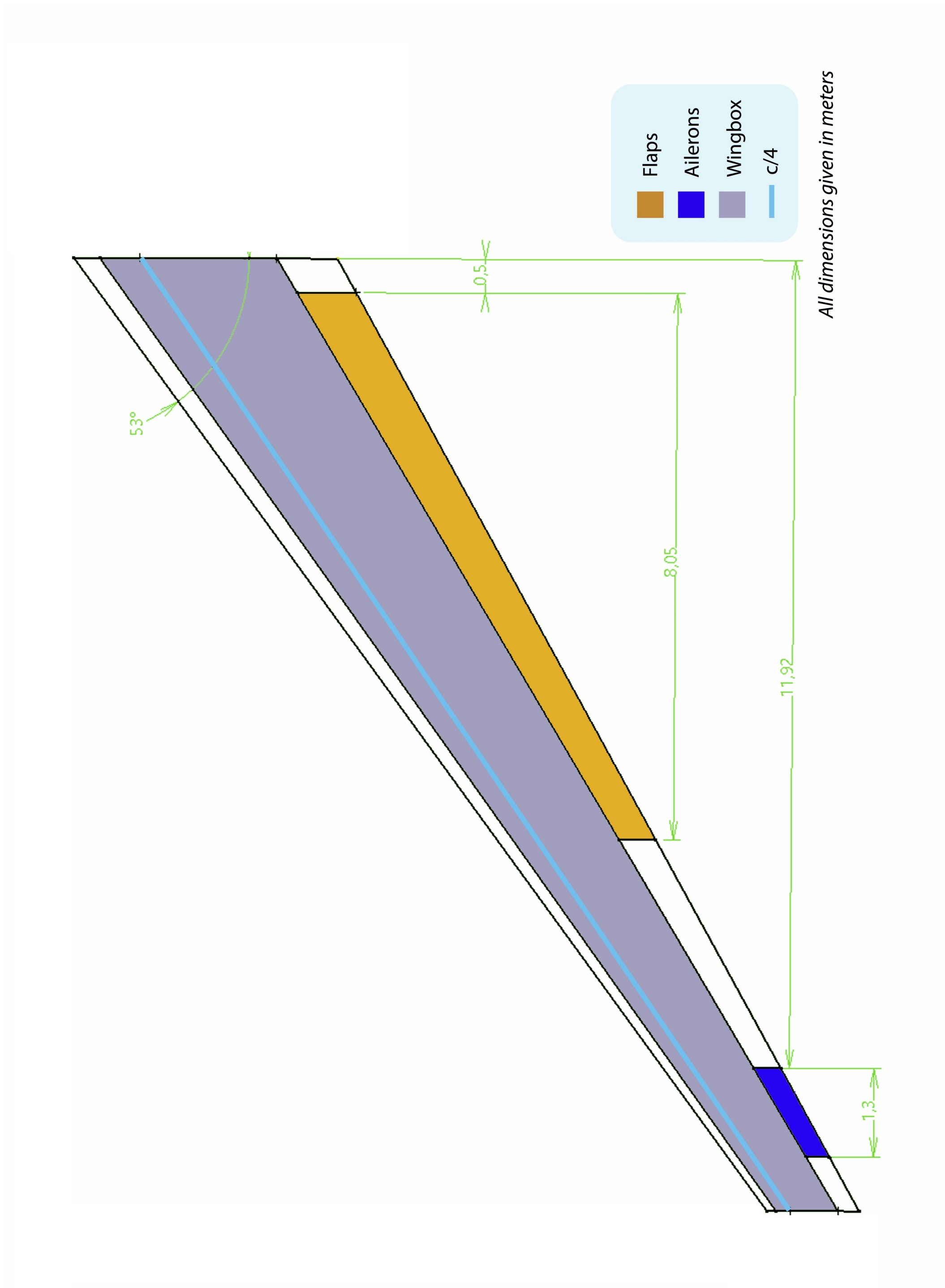

Figure A.1: Wing planform

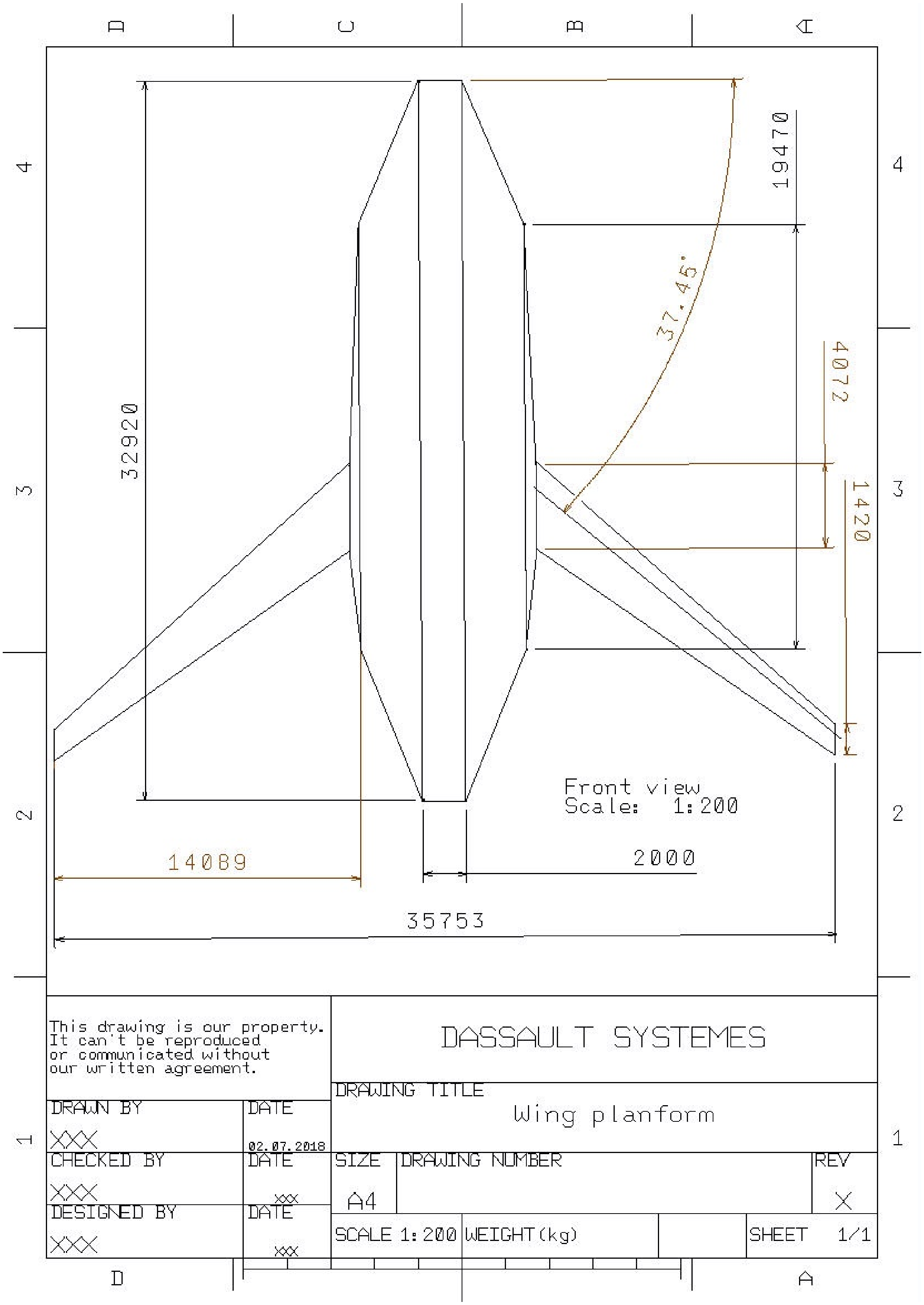

Figure A.2: Aircraft planform

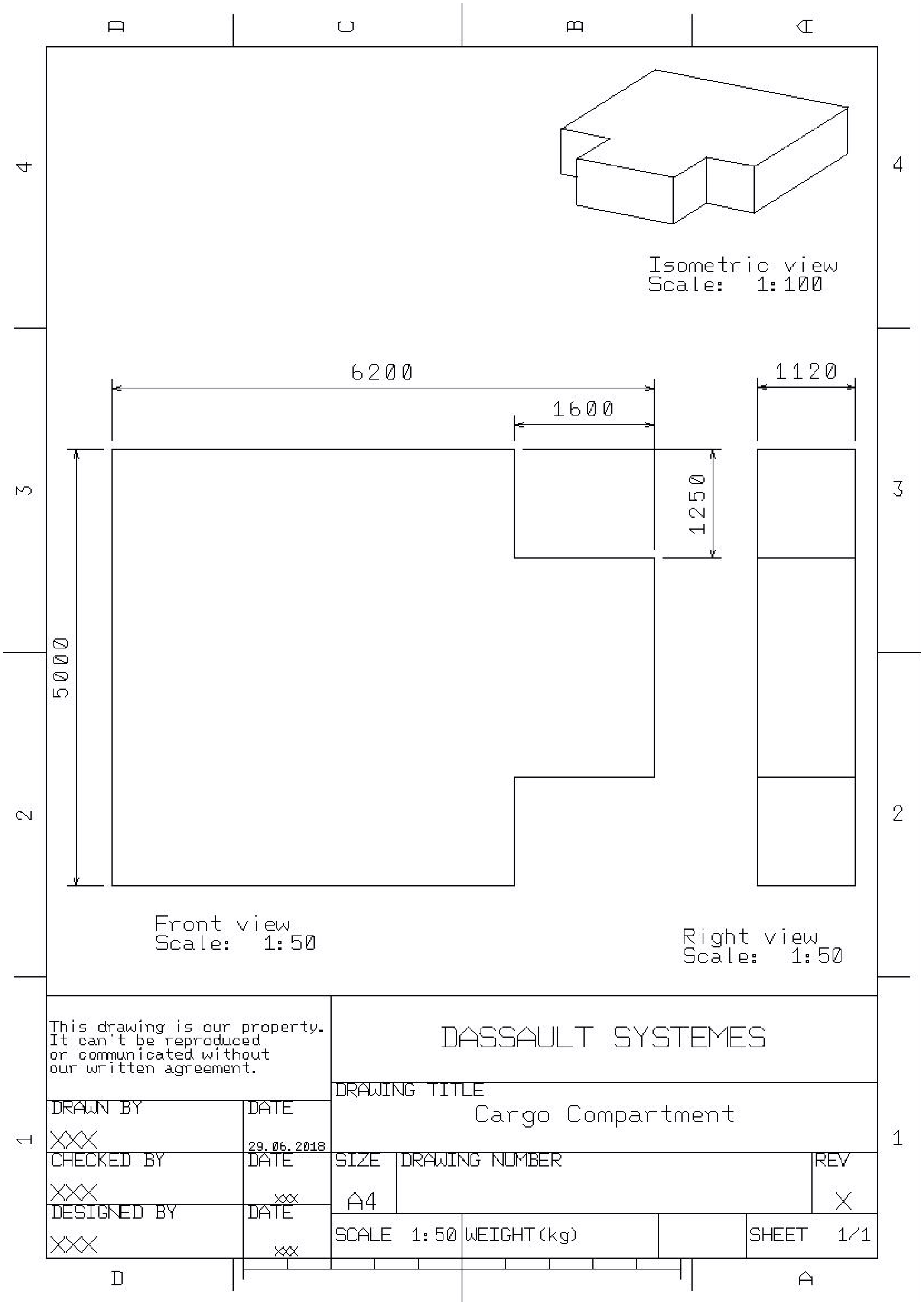

Figure A.3: Cargo compartment

B

Group Organization

Task Division The task division in Table B.1 shows which team member worked on what section(s).

Table B.1: Task Division

Chapter	**Names**
Introduction	Bas Grootnibbelink
Executive Overview	Everyone
Top Level Concept	Antonin Panzo
Stability and Control	Toto Marchand, Benyamin De Leeuw
Aerodynamics	Jeffrey Chen, Bas Grootnibbelink
Structures	Kevin Siemonsma, Jacob Fransen, Adnan Feim
Power and Propulsion	Pjotr Lengkeek, Camille van Weert
Aircraft Performance	Benyamin De Leeuw, Toto Marchand
RAMS	Pjotr Lengkeek
Production Plan	Kevin Siemonsma
Operations & Logistics	Pjotr Lengkeek
Sustainable Development	Bas Grootnibbelink
Market Analysis, budget allocation & cost analysis	Camille van Weert, Antonin Panzo
Technical Risk Assessment	Adnan Feim
Functional Analysis	Jeffrey Chen
Design Overview	Antonin Panzo
Plans for future	Everyone

Distribution List

This report will be distributed to:

- René Alderliesten
- Victor Villalba
- Haohua Zong
- Wim Verhagen
- Erwin Mooij
- PM/SE teaching assistants